Alma Mater Studiorum - Università di Bologna

DIPARTIMENTO DI ASTRONOMIA
Corso di Dottorato di Ricerca in Astronomia
Ciclo XXI
Esame finale anno 2009

A Panchromatic Study of Stellar Populations In Galactic Globular Clusters

Dottorando:
Dott. Emanuele Dalessandro

Relatori:
Ch.mo Prof. Francesco R. Ferraro

Dott.ssa Barbara Lanzoni

Coordinatore:
Ch.mo Prof. Lauro Moscardini

Scuola di Dottorato in Scienze Matematiche, Fisiche e Astronomiche
Settore Scientifico Disciplinare: Area 02 - Scienze Fisiche
FIS/05 Astronomia e Astrofisica

Alla mia famiglia

” L’ ignorante afferma, il saggio dubita, il sapiente riflette ”
(Aristotele)

” Sole fermati su Gabaon e tu, luna, sulla valle di Aialon!
E il sole si fermò e la luna rimase al suo posto... ”
(Giosué X:12-13)

Contents

Chapter 1

Introduction

1.1 Globular Clusters

Globular Clusters (GCs) are systems made of hundreds of thousands of gravitationally bounded stars, distributed in an approximately spherical geometry. They are believed to be the best example of Simple Stellar Populations (SSPs) in Nature, i.e. systems harboring coeval stars, typically with age t=12-13Gyr, and sharing identical chemical composition. Even if recent studies unveiled the presence of multiple stellar populations in a fraction of GCs (mainly the most massive ones; see for example Piotto et al. 2007 for the case of NGC2808), at a first approximation and in most cases they can still be considered as SSPs.

GCs are true touchstones for astrophysics and the study of their stellar populations addresses fundamental questions ranging from stellar evolution, to the dynamics of stellar systems and the Galaxy formation process at early epochs of the Universe. In particular GCs turn out to be astrophysical laboratories for the study of both stellar evolution and stellar dynamics. In recent years it became clear that these two astrophysical aspects cannot be studied independently: physical interactions between single stars as well as the formation, evolution, survival and interactions of binary systems have a significant role in the evolution of GCs and of their stellar populations (SPs; Chernoff & Weinberg 1990). In particular, such interactions change the energy budget of the cluster and therefore influence the time scales on which mass segregation, core collapse and other dynamical processes occur. On the evolutionary side, they can generate peculiar objects (like blue stragglers, X-ray binaries, millisecond pulsars, etc.) that cannot be explained by standard stellar evolution of single stars. Moreover strong stellar segregation during the early phases of GCs formation may provide the material to form the (still undetected) Intermediate Mass Black Holes (IMBHs), which may represent the missing link between the stellar mass BHs and the super-massive BHs (found in the center of nearly all massive galaxies and commonly recognized

as crucial ingredients to understand the processes of galaxy formation).

1.2 Blue Straggler Stars

The most abundant product of such a dynamical activity are the so-called Blue Straggler Stars (BSS). They are core-hydrogen burning stars which appear brighter and bluer than the Turn-Off (TO) point along an extension of the Main Sequence (MS) in the cluster color-magnitude diagrams (CMDs). BSS were first discovered by Sandange (1953) in the outer regions of M3 and for about four decades they were believed to form only in loose clusters or in low-density environments. Thanks to the advent of the high-resolution space telescope HST and ground-based instrumentation with unprecedent wide-field capabilities, the observational and interpretative scenario of BSS has significantly changed. The new generation of astronomical instrumentation in fact shaded new light on the BSS study, correcting some observational biases and making stronger and stronger the idea (now commonly accepted) that BSS stars are a typical population of all the GCs and they populate not only the outer, low-density cluster peripheries, but also (mainly) the highly crowded central regions. Based on these observations, the first complete catalogs of BSS have been published (Fusi Pecci et al. 1992; Sarajedini 1992; Ferraro, Bellazzini & Fusi Pecci 1995) until the most recent collection of BSS counting nearly 3000 candidates (Piotto et al. 2004). However, a major problem in the systematic study of BSS still persists, especially in the highly crowded central regions, because of the high probability of photometric blends which mimic the BSS in the optical CMDs even with HST. In fact, since the CMD of an old stellar population (as a GC) in the classical (V, B - V) plane is dominated by the cool stellar component, the observation and the construction of complete samples of hot stars (as BSS, extreme blue HB, various by-products of binary evolution etc.) is intrinsically difficult in this plane.

In the UV plane, where the sub-giant (SGB) and red giant (RGB) stars responsible for BSS-like blends are faint and the hot stellar populations are relatively bright, those problems are much less severe, thus allowing to obtain complete BSS samples even in the densest cluster core regions. In Fig.1.1 the traditional (V, B-V) CMD (panel (a)) and the UV one (panel (b)) are compared. It's quite evident that in the UV plane the main evolutionary branches display very different morphologies with respect to those in the optical CMD. The RGB is very faint in the UV, while the HB is much brighter. The BSS define a narrow, nearly vertical sequence spanning ~ 3 mag in this plane (see also the case of M3 in Fig. 1.2). Thus, a complete BSS sample can be obtained

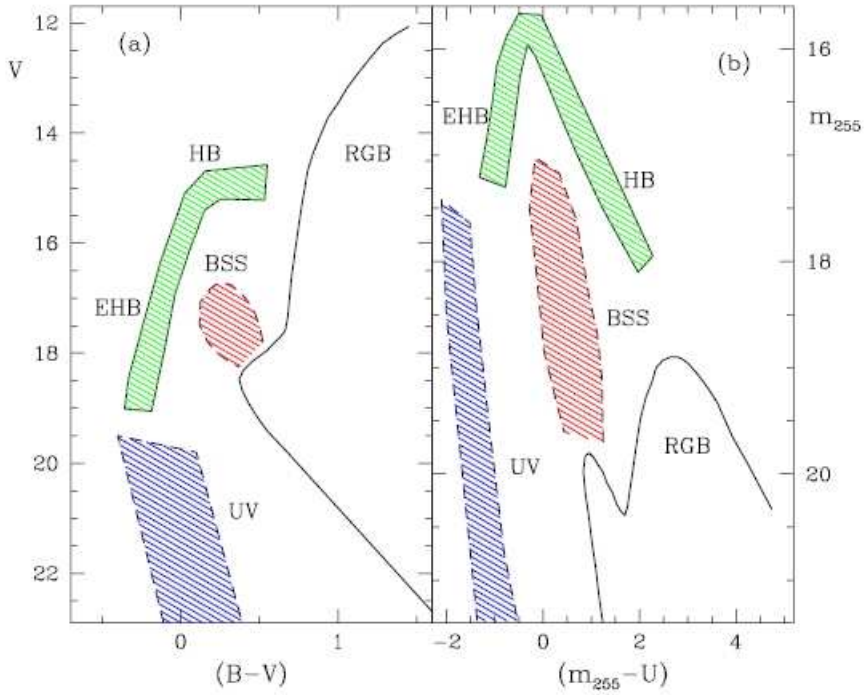

Figure 1.1: The main evolutionary sequences of a GC CMD in the (V,B-V) and (m_{255},m_{255} - U) planes, respectively.

even in the densest cores: indeed, the (m_{255} , m_{255} - m_{336}) plane is an ideal plane for selecting BSS.

1.2.1 Formation Scenarios

Since they populate the upper MS above the cluster TO point, BSS mimic a young stellar population, with masses larger than the normal cluster stars (this is also confirmed by direct mass measurements; e.g. Shara, Saffer & Livio 1997). Hence BSS are thought to be objects that have increased their initial mass during their evolution, and two main scenarios have been proposed for their formation (e.g., Bailyn 1995): the *collisional scenario* suggests that BSS are the end-products of stellar mergers induced by collisions (COL-BSS), while in the *mass-transfer scenario* BSS form by the mass-transfer activity between two companions in a binary system, possibly up to the complete coalescence of the two stars (MT-BSS; Mateo et al. 1990; Pritchet & Glaspey 1991; Bailyn & Pinsonneault 1995; Tian et al. 2006; Leigh, Sills & Knigge 2007). Hence, understanding the origin of BSS in stellar clusters provides valuable insight both on the binary

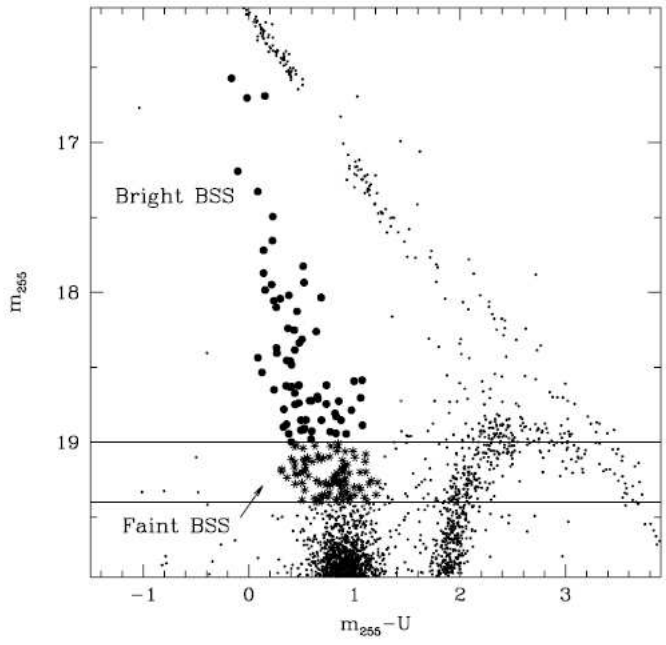

Figure 1.2: UV CMD of the central region of M3. BSS are highlighted as solid dots and aterisks.

fraction and evolution processes and on the effects of dynamical interactions on the (otherwise normal) stellar evolution.

The two formation channels seem to coexist within the same cluster with different efficiencies depending on the environment (Fusi Pecci et al. 1993, Ferraro et al. 1999, Bellazzini et al. 2002). COL-BSS are expected to be formed preferentially in high-density environments (i.e., the GC central regions), where stellar collisions are most probable, while MT-BSS should mainly populate lower density environments (the cluster peripheries), where binary systems can more easily evolve in isolation without suffering exchanges or ionization due to gravitational encounters. The overall scenario is complicated by the fact that primordial binaries can also sink into the core due to mass segregation processes, and "new" binaries can be formed in the cluster centers by gravitational encounters. The two formation mechanisms are likely to be at work simultaneously in every GC (see the case of M3 as an example; Ferraro et al. 1993, 1997), but the identification of the cluster properties that mainly affect their relative efficiency is still an open issue. The detection of unexpected properties of stars along standard evolutionary sequences (e.g., variability, anomalous population fractions, or peculiar radial distributions) can help estimating the fraction of binaries within a cluster (see, e.g., Bailyn 1994, Albrow et al.2001, Bellazzini et al. 2002, Beccari et al.

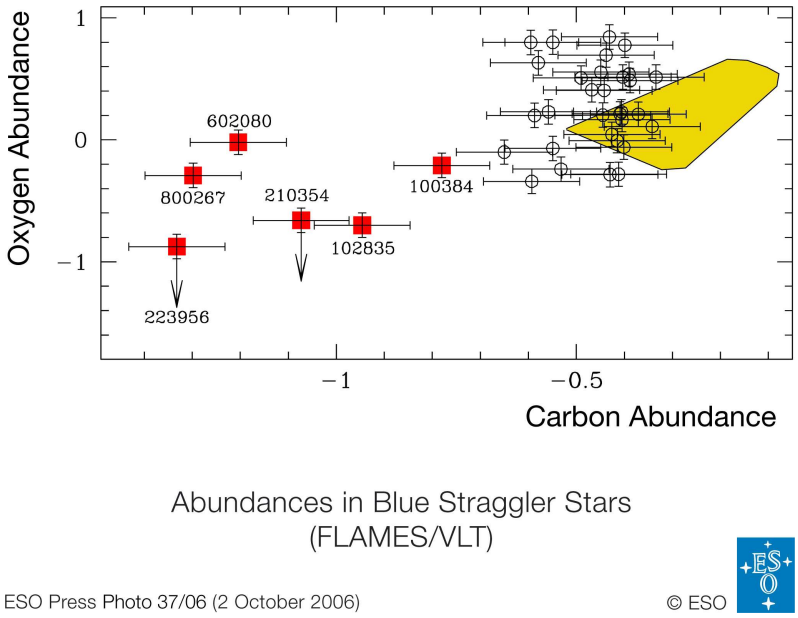

Figure 1.3: [O/Fe] ratio as a function of [C/Fe] for the BSS observed in 47 Tuc. Normal BSS are marked with empty circles, while CO-depleted BSS are marked with filled squares and their names are also reported. The yellow regions correspond to the location of the 12 TO stars in 47 Tuc analyzed by Carretta et al. (2005)

2006), but such evidence does not directly allow the determination of the relative efficiency of the two BSS formation processes. One possibility for distinguishing between the two types of BSS is offered by high-resolution spectroscopic studies. In fact anomalous chemical abundances are expected at the surface of MT-BSS (Sarna & de Greve 1996), while they are not predicted in case of the collisional formation (Lombardi, Rasio & Shapiro 1995). Such spectroscopic studies have just become feasible, and the results found in the case of 47 Tucanae (47 Tuc; Ferraro et al. 2006a) are quite encouraging (see Fig. 1.3).

The most widely applicable tool to probe the origin of BSS is the study of their radial distribution within the clusters (see for a review Ferraro et al. 2006).

1.2.2 The radial distribution

BSS represent the largest population of massive bright objects in GCs. For this reason they should be the most affected by the dynamical evolution of the system and in fact the radial distribution of BSS seems to be a powerful tool to understand the dynamical history of the system and to get insights on how the dynamics can influence the stellar evolution.

The first characterization of the BSS radial distribution was performed in M3 by Ferraro et al.

(1997). A complete coverage of the cluster extent allowed to properly sample both BSS and RGB stars, thus revealing that BSS are more centrally concentrated than RGBs (assumed as reference population), while they are less concentrated in the outskirts. In particular, the radial distribution of the ratio between the BSS and the sampled light is bimodal (Fig. 1.4): highly peaked in the cluster center, decreasing at intermediate radii and rising again in the outskirts. Such a bimodality has then been discovered in other 3 Galactic Globular Clusters (GGCs): 47 Tuc (Ferraro et al. 2004), NGC 6752 (Sabbi et al. 2004), and M5 (hereafter W06, Warren et al. 2006). Preliminary evidence of bimodality has also been found in M55 (Zaggia et al. 1997). As shown by dedicated dynamical simulations (Mapelli et al. 2004, Mapelli et al. 2006), the bimodal radial distributions observed in a few clusters can be reproduced only by including a significative fraction ($\sim 40\%$) of MT-BSS. In this context, the case of ω Cen is atypical: the BSS radial distribution in this cluster is flat (Ferraro et al. 2006b), and mass segregation processes have not yet played a major role, thus implying that the system is populated by a vast majority of MT-BSS (Mapelli et al. 2006). These results demonstrate that detailed studies of the BSS radial distribution within GCs are very powerful tools for better understanding the complex interplay between dynamics and stellar evolution in dense stellar systems.

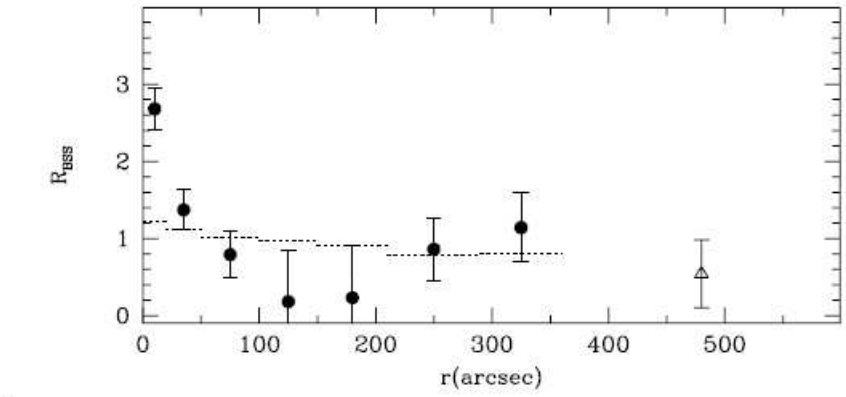

Figure 1.4: Radial distribution of the BSS population of M3 (Ferraro et al. 1997).

1.3 Thesis Structure

The aim of this Thesis is to investigate *(i)* how common the bimodal BSS radial distribution is in stellar clusters and *(ii)* which are the physical processes that can produce this bimodality.

We discuss possible relations between the properties of the BSS radial distribution and the

dynamical state of the hosting clusters by making use of dynamical models and simulations. When relevant, we also discuss the possible links with some cluster "anomalies" and the effects of a massive object (like IMBH) in the cluster center. To this purpose we present the observational studies of the BSS populations and their radial distributions in 5 GGCs. The Thesis is articulated in 6 Chapters, plus a final Section devoted to shortly present future developments of this project.

Chapter 2

In Chapter 2 we present the results obtained for the GGC M5 where we determined the BSS frequency over the nearly entire cluster extent. We used HST data for the central regions and wide field ground-based CCD images for the external ones. We found that the observed BSS radial distribution is bimodal, as in M3 and 47tuc. We performed dynamical simulations (Sigurdsson & Phinney 1995) in order to get more information about the formation scenarios and the role of the dynamics in determining such a distribution. The dynamical simulations showed that the observed radial distribution cannot be explained within a purely collisional scenario in which BSS are generated exclusively in the core through stellar interactions. In fact, an accurate reproduction of the observed BSS radial distribution can be obtained only requiring that a sizable fraction of BSS is generated in the peripheral regions of the cluster, in primordial binary systems that evolve in isolation experiencing mass-transfer.

Chapter 3

A proper photometric analysis of M55, from the near UV to the optical bands, allowed us to reveal the largest external upturn in the BSS radial distribution found to date. This evidence is in contrast with previous findings (Zaggia et al. 1997). Moreover this evident external upturn seems to suggest that the fraction of binaries in the external regions of M55 should be substantially larger than what observed in the core ($\sim 10\%$).

Chapter 4

In this Chapter we present a multiwavelength photometric analysis of the GGC M2. In this case the UV high resolution images obtained with the WFPC2 have been combined with wide-field UV observations performed with GALEX. Additional optical data (from ACS, MEGACAM, EMMI) have been also analyzed and combined to the UV data-set. The entire photometric set has been used to redetermine the cluster structural parameters (center of gravity, r_c, c, etc.) by using the star counts density profile. The BSS radial distribution has been derived and it turns out to

be bimodal. We also searched for radial color gradients (as detected by Sohn et al. 1996) and anomalies in the RGB and AGB populations, finding an overabundance of AGB stars within the core radius of the cluster.

Chapter 5

The photometric analysis presented in this Chapter demonstrates that NGC2419 shows a BSS radial distribution which is flat all over the cluster extension, i.e. the BSS population shares the same radial distribution of the reference populations (HB or RGB stars). This is the second case (after ω Cen) where such a behaviour is found. This observational evidence would suggest that NGC2419 is not relaxed yet. This is in agreement with the estimated half-mass relaxation time which is of the order of the cluster age. In such a case we would be in presence of a huge BSS population formed in a purely non-collisional scenario, where dynamical interactions played a minor role (if any) in determining the observed BSS population and in characterizing its radial distribution.

Chapter 6

Using the same approach previously described, we analyzed the BSS radial distribution of the anomalous GGC NGC 6388. It turns out to be bimodal as in most clusters, but accurate analysis revealed an anomalous radial position of the minimum of the observed distribution. The minimun in the bimodal BSS radial distributions is the observational indication of the efficiency of mass segregation in the clusters. The observed radial position of the dip is interpreted as the radius (*radius of avoidance*, r_{avoid}) at which all the massive stars have already sunk into the core due to dynamical friction and mass segregation processes. In all the cases analyzed so far, the predicted values of r_{avoid} are in good agreement with the observed positions of the minimum of the BSS distribution, with only one exception represented by NGC 6388. Hence the mass segregation in NGC 6388 seems to be less efficient than expected and we discuss some possible explanations for this uncommon behaviour. One possible factor could be the presence of an IMBH in the center of the cluster (see below).

Chapter 7

By using both the surface brightness profile and star-counts density profile we revealed a

significant deviation from a flat core King model in the innermost ($r < 1''$) region of NGC 6388. This could be interpreted as an indication for the presence of a central IMBH. With analytical models we inferred the mass of the IMBH to be about $6 \times 10^3 M_\odot$.

1.4 List of Publications

Referred

1. **The Blue Straggler Population of the Globular Cluster M5.**
   Lanzoni, B.; Dalessandro, E.; Ferraro, F. R.; Mancini, C.; Beccari, G.; Rood, R. T.; Mapelli, M.; Sigurdsson, S.; 2007ApJ, 663, 267L

2. **The Surprising External Upturn of the Blue Straggler Radial Distribution in M55.**
   Lanzoni, B.; Dalessandro, E.; Perina, S.; Ferraro, F. R.; Rood, R. T.; Sollima, A.; 2007ApJ, 670.1065L

3. **The Surface Density Profile of NGC 6388: A Good Candidate for Harboring an Intermediate-Mass Black Hole.**
   Lanzoni, B.; Dalessandro, E.; Ferraro, F. R.; Miocchi, P.; Valenti, E.; Rood, R. T.; 2007ApJ, 668L.139L

4. **Blue straggler stars in the unusual globular cluster NGC 6388.**
   Dalessandro, E.; Lanzoni, B.; Ferraro, F. R.; Rood, R. T.; Milone, A.; Piotto, G.; Valenti, E.; 2008ApJ, 677.1069D

5. **Another Non-segregated Blue Straggler Population in a Globular Cluster: the Case of NGC 2419.**
   Dalessandro, E.; Lanzoni, B.; Ferraro, F. R.; Vespe, F.; Bellazzini, M.; Rood, R. T.; 2008ApJ, 681, 311D

6. **The Nucleus of the Sagittarius Dsph Galaxy and M54: a Window on the Process of Galaxy Nucleation.**
   Bellazzini, M.; Ibata, R. A.; Chapman, S. C.; Mackey, A. D.; Monaco, L.; Irwin, M. J.; Martin, N. F.; Lewis, G. F.; Dalessandro, E.; 2008AJ, 136.1147B

7. **A Panchromatic Study of the Globular Cluster M2.**
   Dalessandro, E.; Beccari, G.; Lanzoni, B.; Ferraro, F. R.; Rood, R. T.; Schiavon, R. P.; submitted to ApJ

8. **The BSS population in M10: from the binary fraction to the dynamical models.**
   Dalessandro, E.; Lanzoni, B.; Ferraro, F. R.; Sollima, A.; Beccari, G.; Rood, R. T.; Schiavon, R. P.; in preparation

Conference proceedings

1. **Ruminations on horizontal branch blue tails.**
   Rood, R. T.; Beccari, G.; Lanzoni, B.; Ferraro, F. R.; Dalessandro, E.; Schiavon, R. P.; 2008MmSAI..79..383R

2. **Blue straggler stars in the unusual globular cluster NGC 6388.**
   Dalessandro, E.; Lanzoni, B.; Ferraro, F. R.; Rood, R. T.; Milone, A.; Piotto, G.; Valenti, E; 2008MmSAI..79..698D

Chapter 2

The Blue Straggler Population of the Globular Cluster M5

Based on the results published in:

Lanzoni, B.; Dalessandro, E.; Ferraro, F. R.; Mancini, C.; Beccari, G.; Rood, R. T.; Mapelli, M.; Sigurdsson, S.; 2007ApJ, 663, 267L

Abstract

By combining high-resolution HST and wide-field ground based observations, in ultraviolet and optical bands, we study the Blue Stragglers Star (BSS) population of the galactic globular cluster M5 (NGC 5904) from its very central regions up to its periphery. The BSS distribution is highly peaked in the cluster center, decreases at intermediate radii and rises again outward. Such a bimodal distribution is similar to those previously observed in other globular clusters (M3, 47 Tucanae, NGC 6752). As for these clusters, dynamical simulations suggest that, while the majority of BSS in M5 could be originated by stellar collisions, a significant fraction (20-40%) of BSS generated by mass transfer processes in primordial binaries is required to reproduce the observed radial distribution. A candidate BSS has been detected beyond the cluster tidal radius. If confirmed, this could represent an interesting case of an "evaporating" BSS.

2.1 Observations and data analysis

2.1.1 The data sets

The present study is based on a combination of two different photometric data sets:

1. The high-resolution set – It consists of a series of ultraviolet (UV) and optical images of the cluster center obtained with HST-WFPC2 (Prop. 6607, P.I. Ferraro). To efficiently resolve

the stars in the highly crowded central regions, the Planetary Camera (PC, being the highest resolution instrument: $0\farcs046$/pixel) has been pointed approximately on the cluster center, while the three Wide Field Cameras (WF, having a lower resolution: $0\farcs1$/pixel) have been used to sample the surrounding regions. Observations have been performed through filter F255W (medium UV) in order to efficiently select the BSS and horizontal branch (HB) populations, and through filters F336W (approximately corresponding to an U filter) and F555W (V) for the red giant branch (RGB) population and to guarantee a proper combination with the ground-based data set (see below). The photometric reduction of the high-resolution images was carried out using ROMAFOT (Buonanno et al. 1983), a package developed to perform accurate photometry in crowded fields and specifically optimized to handle under-sampled Point Spread Functions (PSFs; Buonanno & Iannicola 1989), as in the case of the HST-WF chips.

To obtain a better coverage of the innermost regions of the cluster, we have also used a set of public HST-WFPC2 and HST-ACS observations. The HST-WFPC2 data set has been obtained through filters F439W (B) and F555W (V) by Piotto et al. 2002, and because of the different orientation of the camera, it is complementary to ours. Additional HST-ACS data in filters F435W (B), F606W (V), and F814W (I) have been retrieved from the ESO-STECF Science Archive, and have been used to sample the central area not covered by the WFPC2 observations. All the ACS images were properly corrected for geometric distortions and effective flux (over the pixel area) following the prescriptions of Sirianni et al. 2005. The photometric analysis was performed independently in the three drizzled images by using the aperture photometry code SExtractor (*Source-Extractor*; Bertin & Arnouts 1996), and adopting a fixed aperture radius of 2.5 pixels ($0.125''$). The magnitude lists were finally cross-correlated in order to obtain a combined catalog. The adopted combination of the three HST data sets is sketched in Figure 2.1 and provided a good coverage of the cluster up to $r = 115''$.

2. The wide-field set - A complementary set of wide-field B and V images was secured by using the Wide Field Imager (WFI) at the 2.2m ESO-MPI telescope during an observing run in April 2000. Thanks to the exceptional imaging capabilities of WFI (each image consists of a mosaic of 8 CCDs, for a global field of view of $34' \times 34'$), these data cover the entire cluster extension (see Figure 2.2, where the cluster is roughly centered on CCD $\#7$). The raw WFI images were corrected for bias and flat field, and the overscan regions were trimmed using IRAF[1] tools. The PSF fitting procedure was performed independently on each image using DoPhot (Schechter,

[1]IRAF is distributed by the National Optical Astronomy Observatory, which is operated by the Association of Universities for Research in Astronomy, Inc., under cooperative agreement with the National Science Foundation.

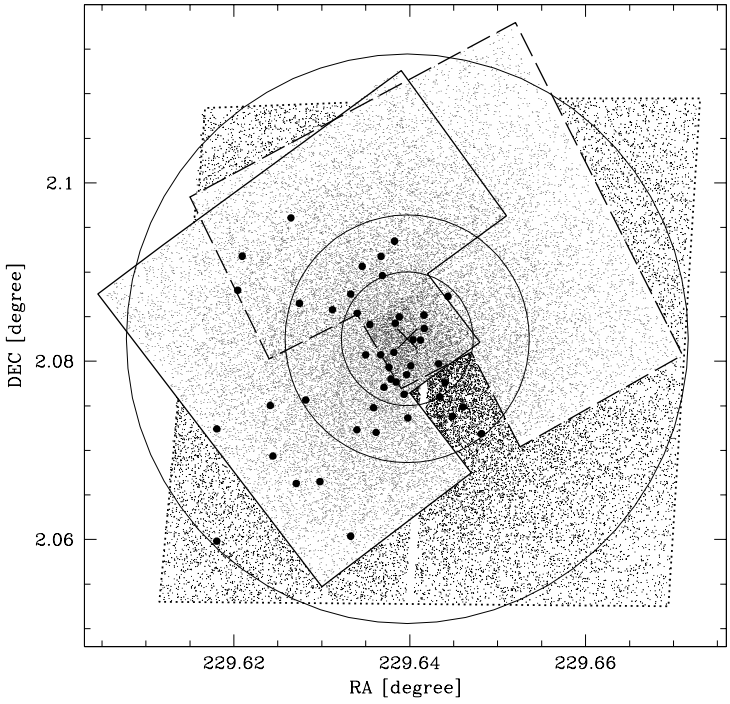

Figure 2.1: Map of the HST sample. The heavy solid line delimits the HST-WFPC2 FoV of our UV observations (Prop. 6607), the dashed line bounds the FoV of the optical HST-WFPC2 observations by Piotto et al. (2002), and the dotted line marks the edge of the complementary ACS data set. The derived center of gravity $C_{\rm grav}$ is marked with a cross. BSS (heavy dots) and the concentric annuli used to study their radial distribution (cfr. Table 2.2) are also shown. The inner and outer annuli correspond to $r = r_c = 27''$ and $r = 115''$, respectively.

Mateo & Saha 1993). All the uncertain detections, usually caused by photometric blends, stars near the CCD gaps or saturated stars, have been checked one by one using ROMAFOT (Buonanno et al. 1983).

2.1.2 Astrometry and center of gravity

The HST+WFI catalog has been placed on the absolute astrometric system by adopting the procedure already described in Ferraro et al. (2001, 2003). The new astrometric Guide Star Catalog (GSC-II[2]) was used to search for astrometric standard stars in the WFI field of view (FoV), and a cross-correlation tool specifically developed at the Bologna Observatory (Montegriffo et al. 2003, private communication) has been employed to obtain an astrometric solution for each of the 8 CCDs. Several hundred GSC-II reference stars were found in each chip, thus allowing an

[2]Available at `http://www-gsss.stsci.edu/Catalogs/GSC/GSC2/GSC2.htm`.

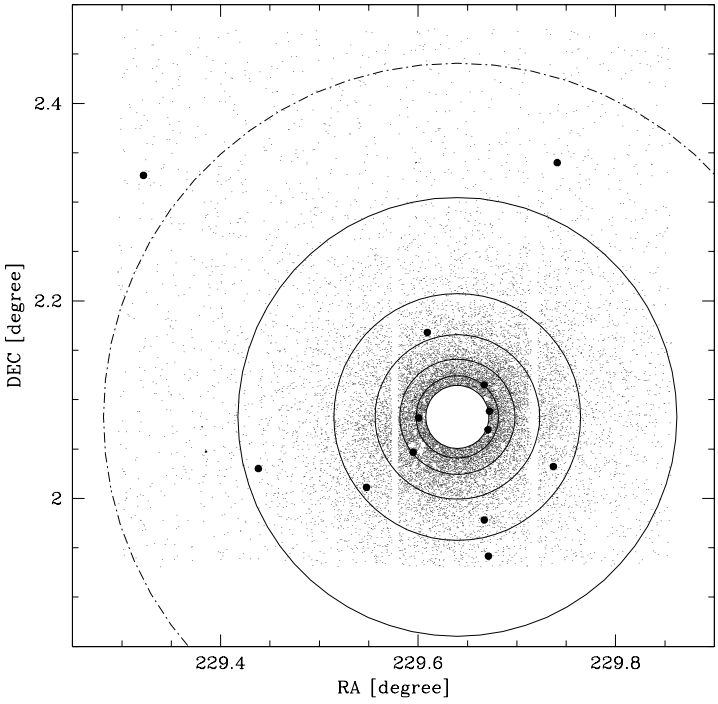

Figure 2.2: Map of the WFI sample. All BSS detected in the WFI sample are marked as heavy dots, and the concentric annuli used to study their radial distribution are shown as solid lines, with the inner and outer annuli corresponding to $r = 115''$ and $r = 800''$, respectively (cfr. Table 2.2). The circle corresponding to the tidal radius ($r_t \simeq 21\farcm5$) is also shown as dashed-dotted line. The BSS lying beyond r_t might represent a BSS previously belonging to M5 and now evaporating from the cluster.

accurate absolute positioning of the stars. Then, a few hundred stars in common between the WFI and the HST FoVs have been used as secondary standards to place the HST catalog on the same absolute astrometric system. At the end of the procedure the global uncertainties in the astrometric solution are of the order of $\sim 0\farcs2$, both in right ascension (α) and declination (δ).

Given the absolute positions of individual stars in the innermost regions of the cluster, the center of gravity $C_{\rm grav}$ has been determined by averaging coordinates α and δ of all stars lying in the PC FoV following the iterative procedure described in Montegriffo et al. (1995; see also Ferraro et al. 2003, 2004). In order to correct for spurious effects due to incompleteness in the very inner regions of the cluster, we considered two samples with different limiting magnitudes ($m_{555} < 19.5$ and $m_{555} < 20$), and we computed the barycenter of stars for each sample. The two estimates agree within $\sim 1''$, giving $C_{\rm grav}$ at $\alpha({\rm J2000}) = 15^{\rm h}\,18^{\rm m}\,33\fs53$, $\delta({\rm J2000}) = +2^{\rm o}\,4'\,57\farcs06$, with a 1σ uncertainty of $0\farcs5$ in both α and δ, corresponding to about

10 pixels in the PC image. This value of $C_{\rm grav}$ is located at $\sim 4''$ south-west ($\Delta\alpha = -4''$, $\Delta\delta = -0''.9$) from that previously derived by Harris 1996 on the basis of the surface brightness distribution.

2.1.3 Photometric calibration and definition of the catalogs

The optical HST magnitudes (i.e., those obtained through the WFPC2 filters F439W and F555W, and through ACS filters F435W, F606W, F814W), as well as the WFI B and V magnitudes have been all calibrated on the catalog of Sandquist et al. (1996). The UV magnitudes m_{160} and m_{255} have been calibrated to the Holtzman et al. (1995) zero-points following Ferraro et al. 1997, 2001), while the U magnitude m_{336} has been calibrated to Dolphin 2000.

In order to reduce spurious effects due to the low resolution of the ground-based observations in the most crowded regions of the cluster, we use only the HST data for the inner $115''$, this value being imposed by the FoV of the WFPC2 and ACS cameras (see Figure 2.1). In particular, we define as *HST sample* the ensemble of all the stars in the WFPC2 and ACS combined catalog having $r \leq 115''$ from the center, and as *WFI sample* all stars detected with WFI at $r > 115''$ (see Figure 2.2). The CMDs of the HST and WFI samples in the $(V,\ U-V)$ and $(V,\ B-V)$ planes are shown in Figure 2.3.

2.1.4 Density profile

We have determined the projected density profile over the entire cluster extension, from $C_{\rm grav}$ out to $\sim 1400'' \sim 23'.3$, by direct star counts, considering only stars brighter than $V = 20$ (see Figure 2.3) in order to avoid incompleteness biases. The brightest RGB stars that are strongly saturated in the ACS data set have been excluded from the analysis, but since they are few in number, the effect on the resulting density profile is completely negligible. Following the procedure already described in Ferraro et al. (1999a, 2004), we have divided the entire HST+WFI sample in 27 concentric annuli, each centered on $C_{\rm grav}$ and split in an adequate number of sub-sectors. The number of stars lying within each sub-sector was counted, and the star density was obtained by dividing these values by the corresponding sub-sector areas. The stellar density in each annulus was then obtained as the average of the sub-sector densities, and its standard deviation was estimated from the variance among the sub-sectors.

The radial density profile thus derived is plotted in Figure 2.4, where we also show the best-fit mono-mass King model and the corresponding values of the core radius and concentration: $r_c = 27''$ (with a typical error of $\sim \pm 2''$) and $c = 1.68$, respectively. These values confirm that

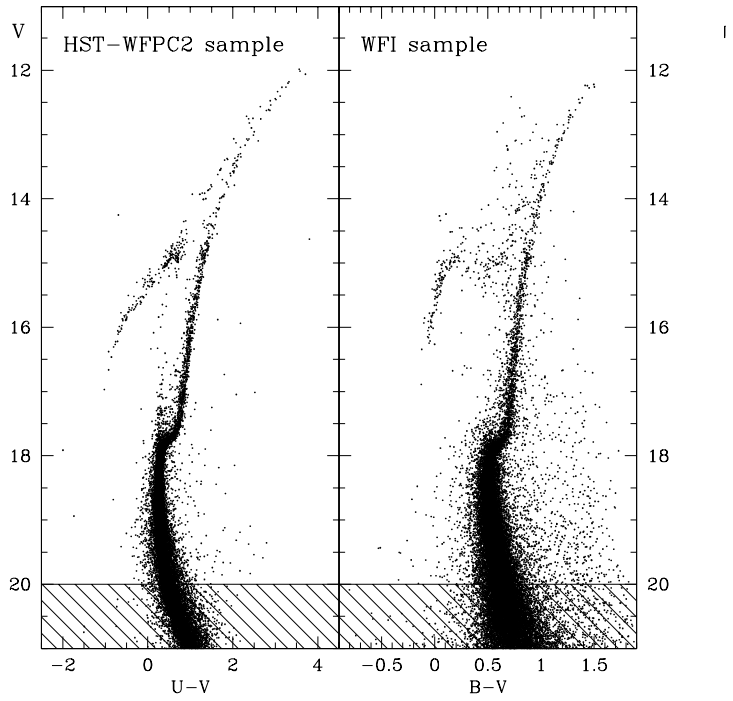

Figure 2.3: Optical CMDs of the WFPC2-HST and the WFI samples. The hatched regions indicate the magnitude limit ($V \leq 20$) adopted for selecting the stars used to construct the cluster surface density profile.

M5 has not yet experienced core collapse, and they are in good agreement with those quoted by McLaughlin & van der Marel (2005) ($r_c = 26\farcs3$ and $c = 1.71$), and marginally consistent with those listed by Harris 1996 ($r_c = 25\farcs2$ and $c = 1.83$), both derived from the surface brightness profile. Our value of r_c corresponds to ~ 1 pc assuming the distance modulus $(m - M)_0 = 14.37$ (Ferraro et al. 1999b; $d \sim 7.5$ Kpc).

2.2 Definition of the samples

In order to study the BSS radial distribution and detect possible peculiarities, both the BSS and a reference population must be properly defined. Since the HST and the WFI data sets have been observed in different photometric bands, different selection boxes are needed to separate the samples in the CMDs. The adopted strategy is described in the following sections (see also Ferraro et al. 2004 for a detailed discussion of this issue).

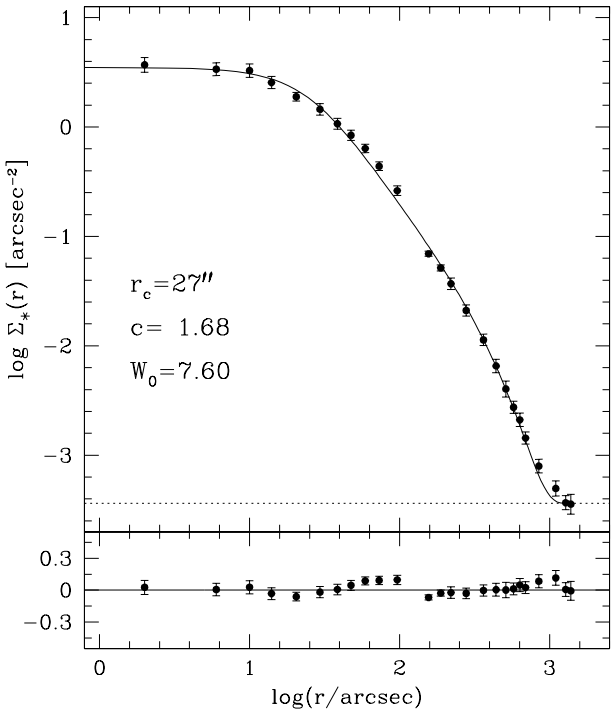

Figure 2.4: Observed surface density profile (dots and error bars) and best-fit King model (solid line). The radial profile is in units of number of stars per square arcseconds. The dotted line indicates the adopted level of the background, and the model characteristic parameters (core radius r_c, concentration c, dimensionless central potential W_0) are marked in the figure. The lower panel shows the residuals between the observations and the fitted profile at each radial coordinate.

2.2.1 The BSS selection

At UV wavelengths BSS are among the brightest objects in a GC, and RGB stars are particularly faint. By combining these advantages with the high-resolution capability of HST, the usual problems associated with photometric blends and crowding in the high density central regions of GCs are minimized, and BSS can be most reliably recognized and separated from the other populations in the UV CMDs. For these reasons our primary criterion for the definition of the BSS sample is based on the position of stars in the ($m_{255},\ m_{255} - U$) plane. In order to avoid incompleteness bias and the possible contamination from TO and sub-giant branch stars, we have adopted a limiting magnitude $m_{255} = 18.35$, roughly corresponding to 1 magnitude brighter than the cluster TO. This is also the limiting magnitude used by W06, facilitating the comparison with their study. The resulting BSS selection box in the UV CMD is shown in Figure 2.5.

Once selected in the UV CMD, the bulk of the BSS lying in the field in common with the

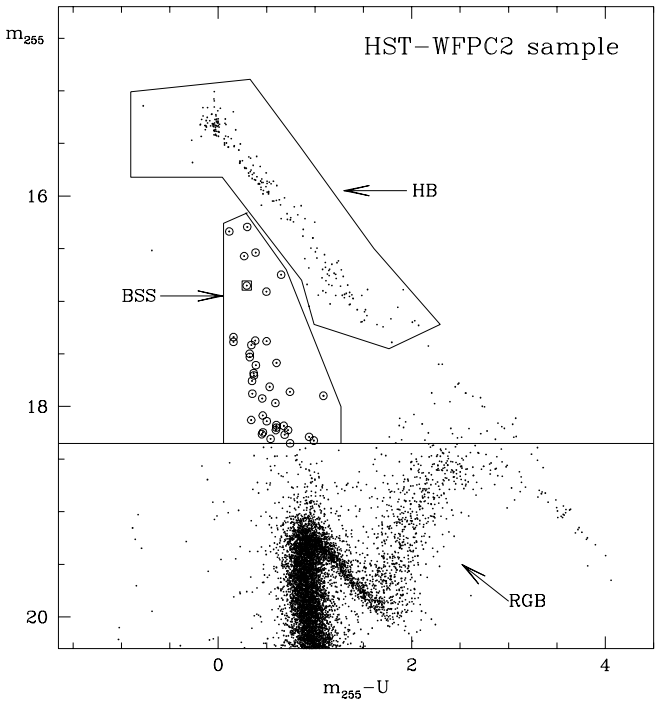

Figure 2.5: CMD of the ultraviolet HST sample. The adopted magnitude limit and selection box used for the definition of the BSS population are shown. The resulting fiducial BSS are marked with empty circles. The open square corresponds to the variable BSS identified by Drissen & Shara (1998) .The box adopted for the selection of HB stars is also shown.

optical-HST sample has been used to define the selection box and the limiting magnitude in the $(B,\ B-V)$ plane. The latter turns out to be $B \simeq 17.85$, and the adopted BSS selection box in the optical CMD is shown in Figure 2.6.

The two stars lying outside the selection box (namely BSS-19 and BSS-20 in Table 2.1) have been identified as BSS from the $(m_{255},\ m_{255}-U)$ CMD. Indeed, they are typical examples of how the optical magnitudes are prone to blend/crowding problems, while the BSS selection in UV bands is much more secure and reliable. An additional BSS (BSS-47 in Table 2.1) lies near the edge of the ACS FoV and has only V and I observations; thus it was selected in the $(V,\ V-I)$ plane (see Figure 2.7, where this BSS is shown together with the other 5 identified in the ACS complementary sample).

With these criteria we have identified 60 BSS: 47 BSS in the HST sample ($r \leq 115''$) and 13 in the WFI one. Their coordinates and magnitudes are listed in Table 2.1. Out of the 47 BSS identified in the HST sample, 41 are from the WFPC2 data set, and 6 from the ACS catalog. As

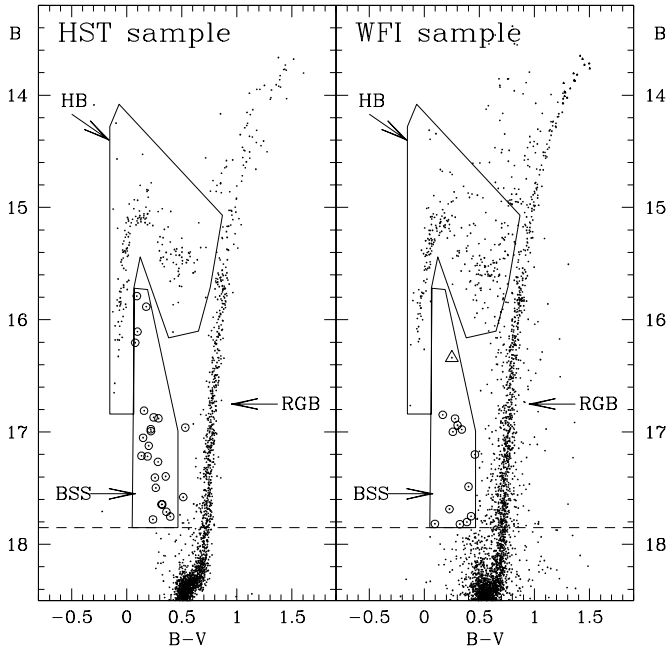

Figure 2.6: CMD of the optical HST-WFPC2 and WFI samples. The adopted BSS and HB selection boxes are shown, and all the BSS identified in these samples are marked with the empty circles. The two BSS not included in the box in the left-hand panel lie well within the selection box in the UV plane and are therefore considered as fiducial BSS. The empty triangle in the right-hand panel corresponds to the BSS identified beyond the cluster tidal radius, at $r \simeq 24'$.

shown in Figure 2.1 their projected distribution is quite asymmetric with the N-E sector seemingly underpopulated. The statistical significance of such an asymmetry appears even higher if only the BSS outside the core are considered. However a quantitative discussion of this topic is not warranted unless additional evidences supporting this anomalous spatial distribution are collected. One of the inner BSS (BSS-29 in Table 2.1) lying at $21\farcs76$ from the center, corresponds to the low-amplitude variable HST-V28 identified by Drissen & Shara (1998)[3]. In the WFI sample ($r > 115''$) we find 13 BSS, with a more symmetric spatial distribution (see Figure 2.2). The most distant BSS (BSS-60 in Table 2.1, marked with an empty triangle in Fig.2.6) lies at $\sim 24'$ from the center, i.e., beyond the cluster tidal radius. Hence, it might be an evaporating BSS previously belonging to the cluster. However, further investigations are needed before firmly assessing this issue.

[3]The observations presented here do not have the time coverage needed to properly search for BSS variability.

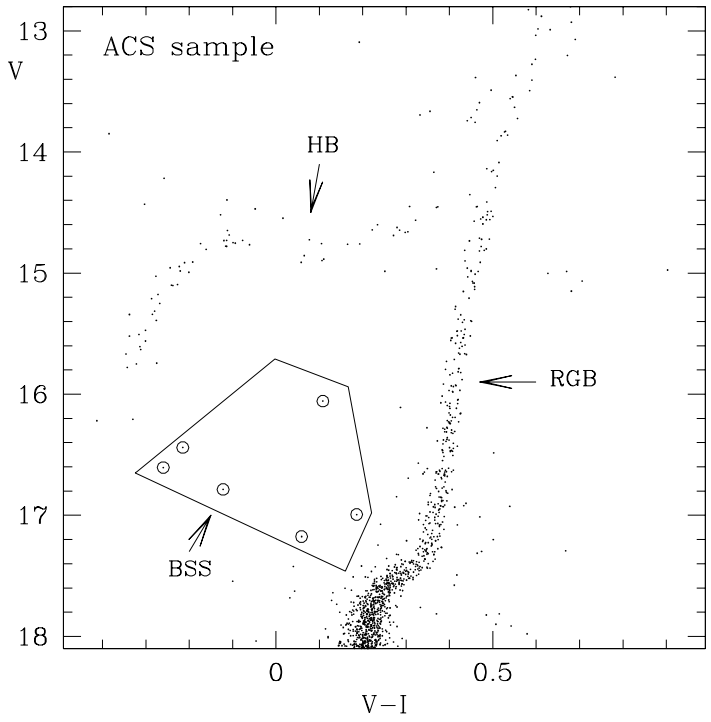

Figure 2.7: CMD of the ACS complementary sample. The BSS selection box is shown, and the resulting fiducial BSS are marked with empty circles.

In order to perform a proper comparison with W06 study, we have transformed their BSS catalog in our astrometric system, and we have found that 50 BSS of their bright sample lie at $r \leq 115''$: 35 are from the HST sample, 13 from the Canada France Hawaii Telescope (CFHT) data set, and 2 from the Cerro Tololo Inter-American Observatory (CTIO) sample; in the outer regions ($115'' < r \lesssim 425''$) 9 BSS are identified, all from the CTIO data set.

By cross correlating W06 bright sample with our catalog we have found 43 BSS in common (see Table 2.1), 37 at $r \leq 115''$ and 6 outward. In particular, 33 BSS out of the 41 (i.e., 80% of the total) that we have identified in the WFPC2-HST sample[4] are found in both catalogs, while 3 of our 5 BSS belong to their faint BSS sample (namely, BSS-27, 34, and 40, corresponding to their Core BSS 70, 79, and 76, respectively), 5 of our BSS have been missed in W06 paper, and 2 objects in their sample are classified as HB stars in our study. This is probably due to different selection criteria, and/or small differences in the measured magnitudes, caused by the different data reduction procedures and photometric analysis. For example, W06 identify the BSS on the

[4]Note that the WFPC2-HST observations used in W06 and in the present study are the same.

basis of both the UV and the optical observations, while we select the BSS only in the UV plane whenever possible. Out of the other 15 BSS found at $r \leq 115''$ in the ground-based CFHT/CTIO sample of W06, 8 BSS (Core BSS 38–45 in their Table 2) clearly are false identifications. They are arranged in a very unlikely ring around a strongly saturated star, as can be seen in Figure 2.8, where the position in the sky of the 8 spurious BSS are overplotted on the CFHT image. Though they clearly are spurious identifications, they still define a clean sequence in the $(B,\ B-I)$ CMD, nicely mimicking the BSS magnitudes and colors.

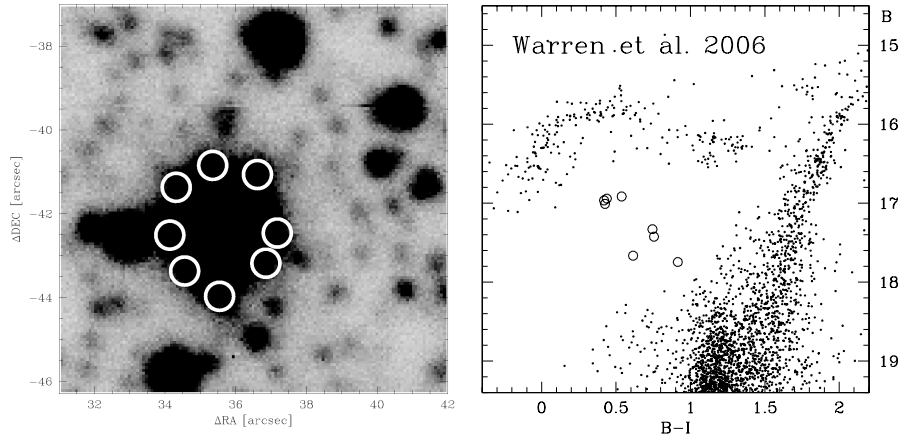

Figure 2.8: *Left-hand panel*: position of the 8 false BSS (marked with white circles) as derived from Table 2 of W06, overplotted to the CFHT image (units are the same as in their Figure 1). As can be seen, a heavily saturated star is responsible for the false identification. *Right-hand panel*: location of the 8 false BSS (empty circles) in the $(B,\ B-I)$ plane, as derived from Table 2 of W06 (cfr. to their Fig. 2).

As already discussed in previous papers, this once again demonstrates how automatic procedures for the search of peculiar objects are prone to errors, especially when using ground-based observations to probe very crowded stellar regions. We emphasize that all the candidate BSS listed in our Table 2.1 have been visually inspected evaluating the quality and the precision of the PSF fitting. This procedure significantly reduces the possibility of introducing spurious objects in the sample. Out of the remaining 7 BSS, 4 objects (namely their Core BSS 32, 30, 37 and 28) are also confirmed by our ACS observations (BSS-42, 43, 44, and 45 respectively), while 2 others (their Core BSS 27 and Ground BSS 6) are not found in the ACS data set, and the remaining one (their Ground BSS 7) is not included in our observation FoV. In turn, two BSS identified in our ACS data set (BSS 46 and 47) are missed in their sample. Concerning the BSS lying at $115'' < r < 450''$, 6 objects (out of 9 found in both samples) are in common between the two catalogs (see Table 2.1), one (BSS-55) belongs to W06 faint sample (their Ground BSS

23), while the remaining 2 do not coincide. Moreover, 4 additional BSS have been identified at $r > 450''$ in our study.

2.2.2 The reference population

Since the HB sequence is bright and well separable in the UV and optical CMDs, we chose these stars as the primary representative population of normal cluster stars to be used for the comparison with the BSS data set. As with the BSS, the HB sample was first defined in the ($m_{255},\ m_{255}-U$) plane, and the corresponding selection box in ($B,\ B-V$) has then been determined by using the stars in common between the UV and the optical samples. The resulting selection boxes in both diagrams are shown in Figures 2.5 and 2.6, and are designed to include the bulk of HB stars[5]. Slightly different selection boxes would include or exclude a few stars only without affecting the results.

We have used WFI observations to roughly estimate the impact of possible foreground field stars contamination on the cluster population selection. As shown in the right-hand panel of Figure 2.6, field stars appear to define an almost vertical sequence at $0.4 < B-V < 1$ in the ($B,\ B-V$) CMD. Hence, they do not affect the BSS selection box, but marginally contaminate the reddest end of the HB. In particular, 5 objects have been found to lie within the adopted HB box in the region at $r > r_t$ sample by our observations (~ 194 arcmin^2); this corresponds to 0.026 spurious HB stars per arcmin^2. On the basis of this, 11 field stars are expected to "contaminate" the HB population over the sampled cluster region ($r < r_t$).

2.3 The BSS radial distribution

The radial distribution of BSS in M5 has been studied following the same procedure previously adopted for other clusters (see references in Ferraro 2006; Beccari et al. 2006).

First, we have compared the BSS cumulative radial distribution to that of HB stars. A Kolmogorov-Smirnov test gives a $\sim\ 10^{-4}$ probability that they are extracted from the same population (see Figure 2.9). BSS are more centrally concentrated than HB stars at $\sim 4\sigma$ level.

For a more quantitative analysis, the surveyed area has been divided into 8 concentric annuli, with radii listed in Table 2.2. The number of BSS ($N_{\rm BSS}$) and HB stars ($N_{\rm HB}$), as well as the fraction of sampled luminosity ($L^{\rm samp}$) have been measured in the 8 annuli and the obtained values are listed in Table 2.2. Note that HB star counts listed in the table are already decontaminated from

[5]The large dispersion in the redder HB stars arises because RR Lyrae variables are included.

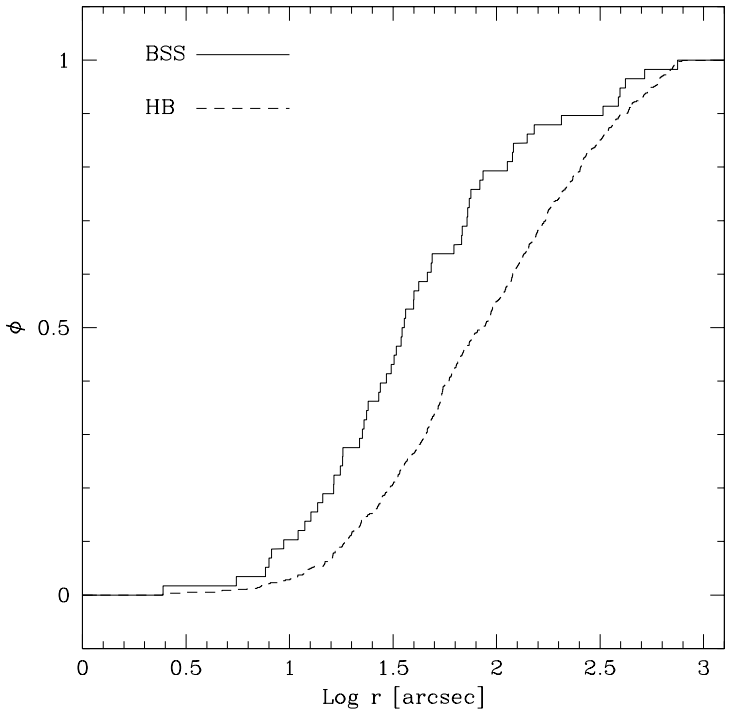

Figure 2.9: Cumulative radial distribution of BSS (solid line) and HB stars (dashed line) as a function of the projected distance from the cluster center for the combined HST+WFI sample. The two distributions differ at $\sim 4\sigma$ level.

field stars, according to the procedure described in Section 2.2.2 (1, 2, and 8 HB stars in the three outer annuli have been estimated to be field stars). The listed values have been used to compute the specific frequency $F_{\rm BSS}^{\rm HB} \equiv N_{\rm BSS}/N_{\rm HB}$, and the double normalized ratio (see Ferraro et al. 1993):

$$R_{\rm pop} = \frac{(N_{\rm pop}/N_{\rm pop}^{\rm tot})}{(L^{\rm samp}/L_{\rm tot}^{\rm samp})}, \tag{2.1}$$

with $\rm pop =$ BSS, HB.

In the present study luminosities have been calculated from the surface density profile shown in Figure 2.4. The surface density has been transformed into luminosity by means of a normalization factor obtained by assuming that the value obtained in the core ($r \leq 27''$) is equal to the sum of the luminosities of all the stars with $V \leq 20$ lying in this region. The distance modulus quoted in Section 2.1.4 and a reddening $E(B-V) = 0.03$ have been adopted (Ferraro et al. 1999b). The fraction of area sampled by the observations in each annulus has been carefully computed, and the sampled luminosity in each annulus has been corrected for incomplete spatial coverage (in the

case of annuli 3 and 8; see Figures 2.1 and 2.2).

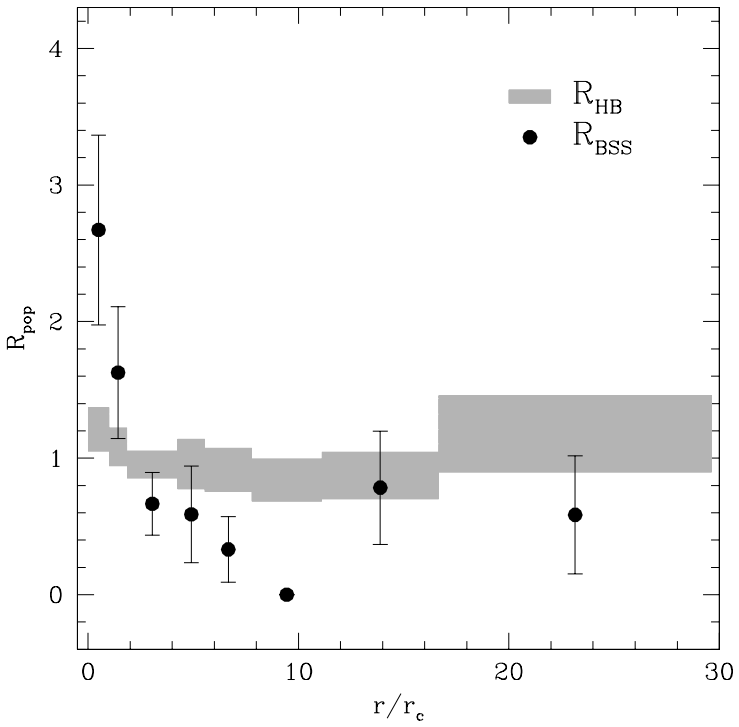

Figure 2.10: Radial distribution of the BSS and HB double normalized ratios, as defined in equation (2.1), plotted as a function of the radial coordinate expressed in units of the core radius. $R_{\rm HB}$ (with the size of the rectangles corresponding to the error bars computed as described in Sabbi et al. 2004) is almost constant around unity over the entire cluster extension, as expected for any normal, non-segregated cluster population. Instead, the radial trend of $R_{\rm BSS}$ (dots with error bars) is completely different: highly peaked in the center (a factor of ~ 3 higher than $R_{\rm HB}$), decreasing at intermediate radii, and rising again outward.

The resulting radial trend of $R_{\rm HB}$ is essentially constant with a value close to unity over the surveyed area (see Figure 2.10). This is just what expected on the basis of the stellar evolution theory, which predicts that the fraction of stars in any post-main sequence evolutionary stage is strictly proportional to the fraction of the sampled luminosity (Renzini & Fusi Pecci 1988). Conversely, BSS follow a completely different radial distribution. As shown in Figure 2.10 the specific frequency $R_{\rm BSS}$ is highly peaked at the cluster center (a factor of ~ 3 higher than $R_{\rm HB}$ in the innermost bin), decreases to a minimum (note that no BSS have been found between $3.'5$ and $5'$.) at $r \simeq 10\, r_c$, and rises again outward. The same behavior is clearly visible also in Figure 2.11, where the population ratio $N_{\rm BSS}/N_{\rm HB}$ is plotted as a function of r/r_c.

Note that the region between $800''$ and $r_t \simeq 1290''$ (and thus also BSS-59, that lies at

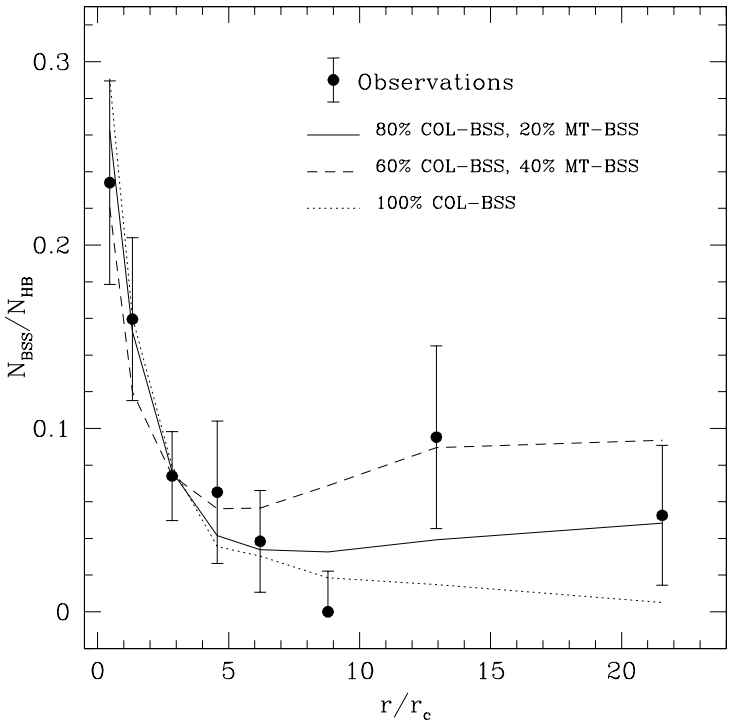

Figure 2.11: Observed radial distribution of the specific frequency $N_{\rm BSS}/N_{\rm HB}$ (filled circles with error bars), as a function of r/r_c. The simulated distribution that best reproduces the observed one is shown as a solid line and is obtained by assuming 80% of COL-BSS and 20% of MT-BSS. The simulated distributions obtained by assuming 40% of MT-BSS (dashed line) and 100% COL-BSS (dotted line) are also shown.

$r \simeq 995''.5$) has not been considered in the analysis, since our observations provide a poor sampling of this annulus: only 35% of its area, corresponding to $\sim 0.4\%$ of the total sampled light, is covered by the WFI pointing. However, for sake of completeness, we have plotted in Figure 2.12 the corresponding value of $F_{\rm BSS}^{\rm HB}$ even for this annulus (empty circle in the upper panel): as can be seen, there is a hint for a flattening of the BSS radial distribution in the cluster outskirts.

2.3.1 Dynamical simulations

Following the same approach as Mapelli et al. (2004, 2006), we now exploit dynamical simulations to derive some clues about the BSS formation mechanisms from their observed radial distribution. We use the Monte-Carlo simulation code originally developed by Sigurdsson & Phinney (1995) and upgraded in Mapelli et al. (2004, 2006). In any simulation run we follow the dynamical evolution of N BSS within a background cluster, taking into account the effects of both

dynamical friction and distant encounters. We identify as COL-BSS those objects having initial positions $r_i \lesssim r_c$, and as MT-BSS stars initially lying at $r_i \gg r_c$ (this because stellar collisions are most probable in the central high-density regions of the cluster, while primordial binaries most likely evolve in isolation in the periphery). Within these two radial ranges, all initial positions are randomly generated following the probability distribution appropriate for a King model. The BSS initial velocities are randomly extracted from the cluster velocity distribution illustrated in Sigurdsson & Phinney (1995), and an additional natal kick is assigned to the COL-BSS in order to account for the recoil induced by the encounters. Each BSS has characteristic mass M and lifetime $t_{\rm last}$. We follow their dynamical evolution in the cluster (fixed) gravitational potential for a time t_i ($i = 1, N$), where each t_i is a randomly chosen fraction of $t_{\rm last}$. At the end of the simulation we register the final positions of BSS, and we compare their radial distribution with the observed one. We repeat the procedure until a reasonable agreement between the simulated and the observed distributions is reached; then, we infer the percentage of collisional and mass-transfer BSS from the distribution of the adopted initial positions in the simulation.

For a detailed discussion of the ranges of values appropriate for these quantities and their effects on the final results we refer to Mapelli et al. (2006). Here we only list the assumptions made in the present study:

- the background cluster is approximated with a multi-mass King model, determined as the best fit to the observed profile[6]. The cluster central velocity dispersion is set to $\sigma = 6.5\,{\rm km\,s^{-1}}$ (Dubath et al. 1997), and, assuming $0.5 M_\odot$ as the average mass of the cluster stars, the central stellar density is $n_c = 2 \times 10^4$ pc^{-3} (Pryor & Meylan 1993);

- the COL-BSS are distributed with initial positions $r_i \leq r_c$ and are given a natal kick velocity of $1 \times \sigma$;

- initial positions ranging between $5\,r_c$ and r_t (with the tidal radius $r_t \simeq 48\,r_c$) have been considered for MT-BSS in different runs;

- BSS masses have been fixed to $M = 1.2\,M_\odot$ (Ferraro et al. 2006a), and their characteristic lifetime to $t_{last} = 2$ Gyr;

- in each simulation run we have followed the evolution of $N = 10,000$ BSS.

[6]By adopting the same mass groups as those of Mapelli et al. (2006), the resulting value of the King dimensionless central potential is $W_0 = 9.7$

The simulated radial distribution that best reproduces the observed one (with a reduced $\chi^2 \simeq 0.6$) is shown in Figure 2.11 (solid line) and is obtained by assuming that $\sim 80\%$ of the BSS population was formed in the core through stellar collisions, while only $\sim 20\%$ is made of MT-BSS. A higher fraction ($\gtrsim 40\%$) of MT-BSS does not correctly reproduce the steep decrease of the distribution and seriously overpredict the number of BSS at $r \sim 10\,r_c$, where no BSS at all are found, but it nicely matches the observed upturning point at $r \simeq 13\,r_c$ (see the dashed line in Figure 2.11). On the other hand, a population of only COL-BSS is unable to properly reproduce the external upturn of the distribution (see the dotted line in Figure 2.11), and 100% of MT-BSS is also totally excluded. Assuming heavier BSS (up to $M = 1.5\,M_{\odot}$) or different lifetimes t_{last} (between 1 and 4 Gyr) does not significantly change these conclusions, since both these parameters mainly affect the external part of the simulated BSS distribution. Thus, an appreciable effect can be seen only in the case of a relevant upturn, and negligible variations are found in the best-fit case and when assuming 100% COL-BSS. The effect starts to be relevant in the simulations with 40% or more MT-BSS, which are however inconsistent with the observations at intermediate radii (see above).

By using the simulations and the dynamical friction timescale (e.g. from Mapelli et al. 2006), we have also computed the radius of avoidance of M5. This is defined as the characteristic radial distance within which all MT-BSS are expected to have already sunk to the cluster core, because of mass segregation processes. Assuming 12 Gyr for the age of M5 (Sandquist et al. 1996) and $1.2\,M_{\odot}$ for the BSS mass, we find that $r_{\rm avoid} \simeq 10\,r_c$. This nicely corresponds to the position of the minimum in the observed BSS radial distribution, in agreement with the findings of Mapelli et al. (2004, 2006).

2.4 Summary and discussion

In this paper we have used a combination of HST UV and optical images of the cluster center and wide-field ground-based observations covering the entire cluster extension to derive the main structural parameters and to study the BSS population of the galactic globular cluster M5.

The accurate determination of the cluster center of gravity from the high-resolution data gives $\alpha(\mathrm{J2000}) = 15^{\rm h}\,18^{\rm m}\,33\overset{\rm s}{.}53$, $\delta(\mathrm{J2000}) = +2^{\rm o}\,4'\,57\overset{''}{.}06$, with a 1σ uncertainty of $0\overset{''}{.}5$ in both α and δ. The cluster density profile, determined from direct star counts, is well fit by a King model with core radius $r_c = 27''$ and concentration $c = 1.68$, thus suggesting that M5 has not yet suffered the core collapse.

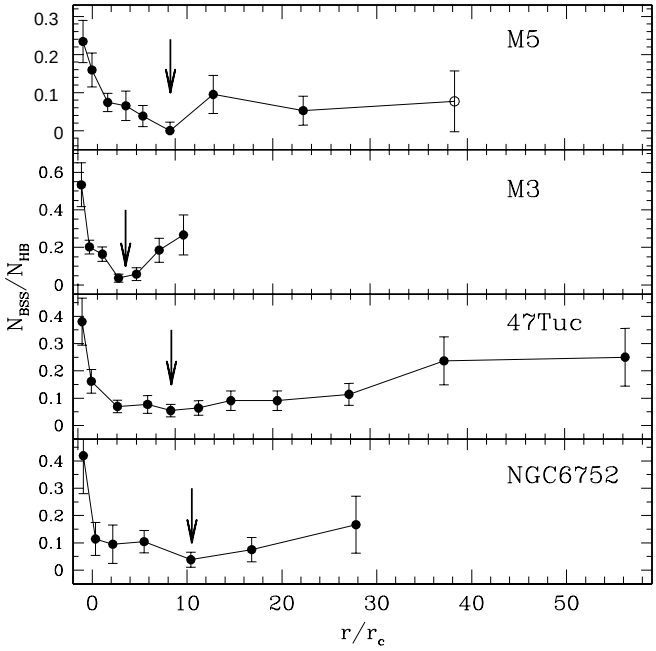

Figure 2.12: Radial distribution of the population ratio $N_{\rm BSS}/N_{\rm HB}$ for M5, M3, 47 Tuc, and NGC 6752, plotted as a function of the radial distance from the cluster center, normalized to the core radius r_c (from Mapelli et al. 2006, $r_c \simeq 30'', 21'', 28''$ for M3, 47 Tuc, and NGC 6752, respectively). The arrows indicate the position of the minimum of the distribution in each case. The outermost point shown for M5 (empty circle) corresponds to BSS-58, lying at $r \simeq 995''$. This star has not been considered in the quantitative study of the BSS radial distribution since only a negligible fraction of the annuls between $800''$ and r_t is sampled by our observations.

The BSS population of M5 amounts to a total of 59 objects, with a quite asymmetric projected distribution (see Figure 2.1) and a high degree of segregation in the cluster center. With respect to the sampled luminosity and to HB stars, the BSS radial distribution is bimodal: highly peaked at $r \lesssim r_c$, decreasing to a minimum at $r \simeq 10\, r_c$, and rising again outward (see Figures 2.10 and 2.11).

The comparison with results of W06 has revealed that 43 (out of 59) bright BSS identified by these authors at $r \lesssim 450''$ are in common with our sample. Moreover, 4 additional stars classified as faint BSS in their study are in common with our BSS sample at $r \lesssim 450''$. Considering that we find 56 BSS within the same radial distance from the center, this corresponds to 84% matching of our catalogue. The discrepancies are explained by different data reduction procedures, photometric analysis, and adopted selection criteria, other than the spurious identification of 8 BSS

by W06, due a strongly saturated star in their sample. The central peak of the $R_{\rm BSS}$ distribution in our study is slightly higher (but compatible within the error bar) compared to that of W06, and we extend the analysis to larger distance from the center (out to $r > 800''$), thus unveiling the external upturn and the possible flattening of the BSS distribution in the cluster outskirts.

Moreover, we have compared the BSS radial distribution of M5 with that observed in other GCs studied in a similar way. In Figure 2.12 we plot the specific frequency $F_{\rm BSS}^{\rm HB}$ as a function of (r/r_c) for M5, M3, 47 Tuc, and NGC 6752. Such a comparison shows that the BSS radial distributions in these clusters are only *qualitatively* similar, with a high concentration at the center and an upturn outward. However, significant quantitative differences are apparent: (1) the $F_{\rm BSS}^{\rm HB}$ peak value, (2) the steepness of the decreasing branch of the distribution, (3) the radial position of the minimum (marked by arrows in the figure), and (4) the extension of the "zone of avoidance," i.e., the intermediate region poorly populated by BSS. In particular M5 shows the smallest $F_{\rm BSS}^{\rm HB}$ peak value: it turns out to be ~ 0.24, versus a typical value $\gtrsim 0.4$ in all the other cases. It also shows the mildest decreasing slope: at $r \approx 2\,r_c$ the specific frequency in M5 is about a half of the peak value, while it decreases by a factor of 4 in all the other clusters. Conversely, it is interesting to note that the value reached by $F_{\rm BSS}^{\rm HB}$ in the external regions is $\sim$ 50-60% of the central peak in all the studied clusters. Another difference between M5 and the other systems concerns the ratio between the radius of avoidance and the tidal radius: $r_{\rm avoid} \simeq 0.2\,r_t$ for M5, while $r_{\rm avoid} \lesssim 0.13\,r_t$ for 47 Tuc, M3, and NGC 6752 (see Tables 1 and 2 in Mapelli et al. 2006).

The dynamical simulations discussed in Section 2.3.1 suggest that the majority of BSS in M5 are collisional, with a content of MT-BSS ranging between 20% and 40% of the overall population. This fraction seems to be smaller than that (40-50%) derived for M3, 47 Tuc and NGC 6752 by Mapelli et al. (2006), in qualitative agreement with the smaller value of $r_{\rm avoid}/r_t$ estimated for M5, which indicates that the fraction of cluster currently depopulated of BSS is larger in this system than in the other cases. More in general, the results shown in Figure 2.11 exclude a pure collisional BSS content for M5.

Our study has also revealed the presence of a candidate BSS at $\sim 24'$ from the center, i.e., beyond the cluster tidal radius (see Figures 2.2 and 2.6 and BSS-59 in Table 2.1). If confirmed, this could represent a very interesting case of a BSS previously belonging to M5 and then evaporating from the cluster (a BSS kicked off from the core the because of dynamical interactions?).

Table 2.1: The BSS population of M5. The first 41 BSS have been identified in the WFPC2 sample; BSS-42–46 are from the complementary ACS observations; BSS-47–59 are from the WFI data-set. BSS-59 lies beyond the cluster tidal radius, at $\sim 24'$ from the center. The last column list the corresponding BSS in W06 sample, with "CR" indicating their "Core BSS" and "OR" their "Outer Region BSS".

Name	RA[degree]	Dec[degree]	m_{255}	U	B	V	I	W06
BSS-1	229.6354506	2.0841090	16.52	16.15	15.88	15.71	-	CR2
BSS-2	229.6388102	2.0849660	17.95	17.38	17.40	17.04	-	CR4
BSS-3	229.6383433	2.0842640	18.21	17.63	17.64	17.32	-	CR3
BSS-4	229.6416234	2.0851791	17.59	17.22	17.05	16.90	-	CR5
BSS-5	229.6416518	2.0836794	16.28	15.99	15.79	15.70	-	CR1
BSS-6	229.6381953	2.0810119	17.36	16.99	16.81	16.65	-	CR21
BSS-7	229.6403657	2.0824062	17.40	17.07	16.97	16.76	-	CR12
BSS-8	229.6412279	2.0823768	17.91	17.47	17.41	17.15	-	CR13
BSS-9	229.6376256	2.0793288	17.84	17.12	16.99	16.77	-	CR23
BSS-10	229.6401139	2.0794858	17.57	16.98	16.87	16.62	-	CR22
BSS-11	229.6396566	2.0784944	17.51	17.20	17.12	16.92	-	CR24
BSS-12	229.6432834	2.0797197	18.12	17.64	17.78	17.54	-	-
BSS-13	229.6384406	2.0776614	17.36	16.88	16.88	16.59	-	CR25
BSS-14	229.6274500	2.0864896	18.07	17.63	17.64	17.33	-	CR8
BSS-15	229.6204246	2.0879629	18.33	17.61	17.75	17.36	-	CR11
BSS-16	229.6209379	2.0917858	17.80	17.28	17.26	16.98	-	CR18
BSS-17	229.6264834	2.0960870	16.32	16.22	16.20	16.13	-	CR20
BSS-18	229.6368731	2.0896002	16.56	16.30	16.11	16.01	-	CR14
BSS-19	229.6367309	2.0917639	18.27	17.35	17.58	17.07	-	CR17
BSS-20	229.6345837	2.0906438	17.88	16.81	16.96	16.43	-	CR16
BSS-21	229.6382677	2.0934706	18.25	17.58	17.71	17.35	-	CR19
BSS-22	229.6340227	2.0853879	17.67	17.32	17.22	17.03	-	CR7
BSS-23	229.6332685	2.0875294	17.69	17.34	17.21	17.08	-	CR10
BSS-24	229.6366685	2.0807168	18.23	17.78	17.67	17.37	-	-
BSS-25	229.6393544	2.0762832	18.11	17.79	17.72	17.50	-	-
BSS-26	229.6378381	2.0779999	17.86	17.52	17.43	17.27	-	-
BSS-27	229.6349851	2.0807202	18.17	17.51	17.74	17.30	-	CR70
BSS-28	229.6397645	2.0736403	18.19	17.60	17.69	17.28	-	CR33
BSS-29	229.6370495	2.0770798	16.83	16.56	16.57	17.75	-	CR26
BSS-30	229.6358816	2.0747883	18.25	17.81	17.79	17.51	-	CR31
BSS-31	229.6361653	2.0720147	18.29	17.77	17.81	17.47	-	CR36
BSS-32	229.6339822	2.0723032	16.73	16.10	16.16	15.95	-	CR35
BSS-33	229.6281392	2.0756490	17.74	17.41	17.22	17.09	-	CR29
BSS-34	229.6241278	2.0750261	18.21	17.50	17.65	17.27	-	CR79
BSS-35	229.6332759	2.0603761	17.48	17.17	16.95	16.86	-	CR48
BSS-36	229.6270877	2.0662947	17.33	17.18	17.06	16.95	-	CR47

(continued on next page)

Table 2.1 – continued from previous page

Name	RA[degree]	Dec[degree]	m_{255}	U	B	V	I	W06
BSS-37	229.6244175	2.0693612	16.89	16.41	16.51	15.71	-	CR46
BSS-38	229.6180419	2.0724090	17.37	17.23	17.12	17.00	-	CR34
BSS-39	229.6311963	2.0857800	18.31	17.33	17.40	16.76	-	-
BSS-40	229.6297499	2.0664961	18.16	17.58	-	17.27	-	CR76
BSS-41	229.6443367	2.0872809	-	-	17.50	17.23	-	CR9
BSS-42	229.6448646	2.0738335	-	-	16.53	16.06	15.95	CR32
BSS-43	229.6460645	2.0748695	-	-	16.64	16.44	16.66	CR30
BSS-44	229.6481631	2.0718829	-	-	16.72	16.61	16.87	CR37
BSS-45	229.6433942	2.0760163	-	-	17.03	16.79	16.91	CR28
BSS-46	229.6439884	2.0775670	-	-	17.44	16.99	16.81	-
BSS-47	229.6180420	2.0598328	-	-	-	17.18	17.12	-
BSS-48	229.6092873	2.1680914	-	-	16.85	16.68	-	OR2
BSS-49	229.6723094	2.0882827	-	-	16.94	16.64	-	OR9
BSS-50	229.6006551	2.0814678	-	-	17.00	16.74	-	OR10
BSS-51	229.6669956	1.9781808	-	-	17.20	16.74	-	OR1
BSS-52	229.5949935	2.0469325	-	-	17.69	17.46	-	OR4
BSS-53	229.6706625	2.0695464	-	-	17.82	17.50	-	-
BSS-54	229.6667908	2.1149550	-	-	17.82	17.72	-	-
BSS-55	229.7370667	2.0323392	-	-	17.80	17.42	-	OR23
BSS-56	229.5476990	2.0112610	-	-	16.88	16.60	-	OR5
BSS-57	229.6711255	1.9415566	-	-	16.98	16.64	-	-
BSS-58	229.4381714	2.0302088	-	-	17.75	17.33	-	-
BSS-59	229.7408412	2.3399166	-	-	17.49	17.08	-	-
BSS-60	229.3218200	2.3271022	-	-	16.34	16.09	-	-

r_i''	r_e''	$N_{\rm BSS}$	$N_{\rm HB}$	$L^{\rm samp}/L^{\rm samp}_{\rm tot}$
0	27	22	94	0.14
27	50	15	94	0.16
50	115	10	135	0.26
115	150	3	46	0.09
150	210	2	52	0.10
210	300	0	45†	0.10
300	450	4	42†	0.09
450	800	2	38†	0.06

Table 2.2: † The $N_{\rm HB}$ values listed here are those corrected for field contamination (i.e., 1, 2 and 8 stars have been subtracted to the observed number counts in these three external annuli, respectively).

Chapter 3

The surprising external upturn of the Blue Straggler radial distribution in M55

Based on the results published in:

Lanzoni, B.; Dalessandro, E.; Perina, S.; Ferraro, F. R.; Rood, R. T.; Sollima, A.;

2007ApJ, 670.1065L

Abstract

By combining high-resolution HST and wide-field ground based observations, in ultraviolet and optical bands, we study the Blue Straggler Star (BSS) population of the low density galactic globular cluster M55 (NGC 6809) over its entire radial extent. The BSS projected radial distribution is found to be bimodal, with a central peak, a broad minimum at intermediate radii, and an upturn at large radii. Similar bimodal distributions have been found in other globular clusters (M3, 47 Tucanae, NGC 6752, M5), but the external upturn in M55 is the largest found to date. This might indicate a large fraction of primordial binaries in the outer regions of M55, which seems somehow in contrast with the relatively low ($\sim 10\%$) binary fraction recently measured in the core of this cluster.

3.1 Observations and data analysis

3.1.1 The Data Sets

The present study is based on a combination of two different photometric data sets:

1. The high-resolution set – It consists of a series of *HST*-WFPC2 images of the cluster center (Prop. 10524, P.I. Ferraro), obtained through filter F255W (medium UV, for a total exposure time

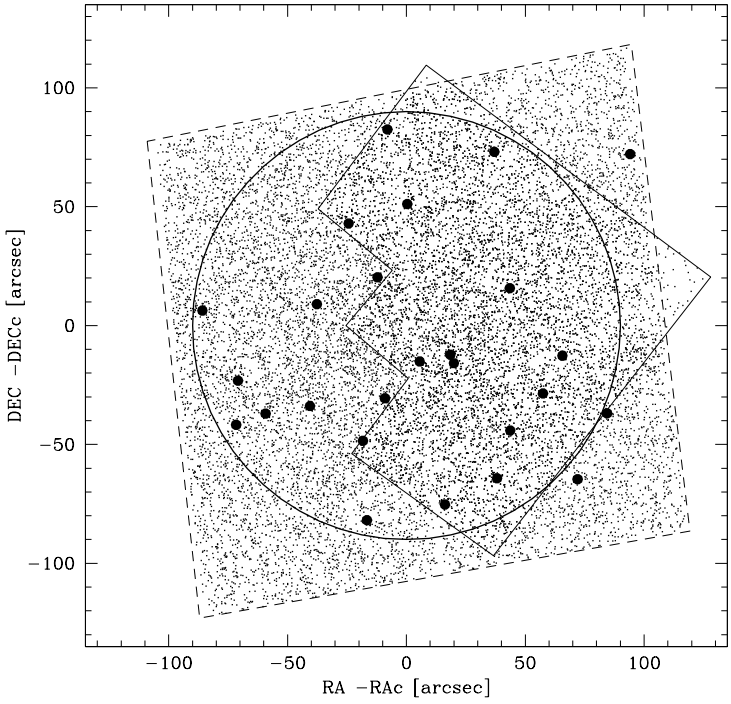

Figure 3.1: Map of the HSTsample, with coordinates referred to the derived center of gravity Cgrav: $C_{\rm grav}$ to be $\alpha(\mathrm{J2000}) = 19^{\rm h}\,39^{\rm m}\,59\overset{\rm s}{.}54$, $\delta(\mathrm{J2000}) = -30^{\rm o}\,57'\,45\overset{''}{.}14$. The solid and dashed thin lines delimit the HST-WFPC2 and HST-ACS fields of view, respectively. The selected BSSs (heavy dots) and the annulus with radius $r = 90''$ used to study their projected radial distribution (compare Table 3.2) are also shown.

$t_{exp} = 2000$ s) and F336W (approximately corresponding to an U filter, with $t_{exp} = 1600$ s). To efficiently resolve the stars in the highly crowded central regions, the Planetary Camera has been pointed approximately on the cluster center, while the three Wide Field Cameras (WFC) have been used to sample the surrounding regions. The photometric reduction of the images was carried out using ROMAFOT (Buonanno et al. 1983), a package developed to perform accurate photometry in crowded fields and specifically optimized to handle under-sampled point spread functions (Buonanno et al. 1989), as in the case of the WFC chips. Additional *HST* images of the cluster center, obtained with the ACS-Wide Field Channel (Prop. 10775, P.I. Sarajedini) have been retrieved from the ESO-STECF Science Archive. Only the short exposures (10 sec each) in filters F606W (V) and F814W (I) have been used in the present work. The adopted data reduction procedure is described in detail in (Sollima et al. 2007). For a schematic view look at Fig. 3.1.

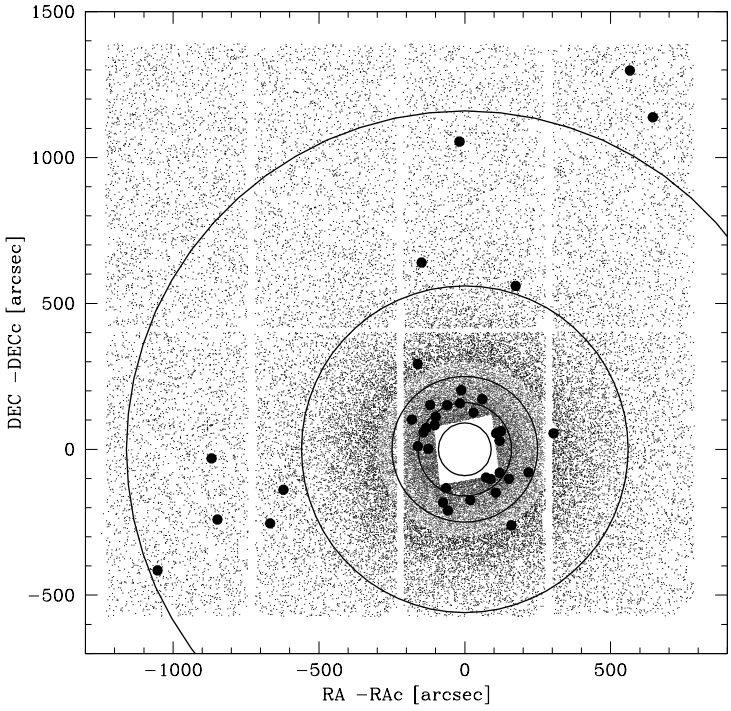

Figure 3.2: Map of the complementary WFI sample, with coordinates referred to Cgrav. The empty central region corresponds to the HST-ACS FOV (Fig. 3.1, dashed line). All the detected BSSs aremarked as heavy dots, and the concentric annuli used to study their projected radial distribution (compare Table 3.2) are shown as filled circles, with the inner annulus corresponding to $r = 90''$ and the outer one corresponding to the tidal radius $r_t = 1160''$. The two candidate BSSs lying beyond rt most probably are field stars.

2. The wide-field set - A complementary set of public wide-field B and V images obtained with the Wide Field Imager (WFI) at the 2.2m ESO-MPI telescope was retrieved from the ESO Science Archive. Thanks to the wide ($34' \times 34'$) FoV of WFI, these data almost cover the entire cluster extension (see Fig. 3.2). The raw WFI images were corrected for bias and flat field, and the overscan regions were trimmed using IRAF[1] tools. The PSF fitting procedure was then performed independently on each image using DoPhot (Schechter et al. 1993).

3.1.2 Astrometry and Photometric Calibration

The *HST* and WFI catalogs have been placed on the absolute astrometric system by adopting the procedure described in (Ferraro et al. 2001, 2003). The new astrometric Guide Star Catalog

[1]IRAF is distributed by the National Optical Astronomy Observatory, which is operated by the Association of Universities for Research in Astronomy, Inc., under cooperative agreement with the National Science Foundation.

(GSC-II[2]) was used to search for astrometric standard stars in the WFI FoV, and a specific cross-correlation tool has been employed to obtain an astrometric solution for each of the 8 CCDs. Several hundred GSC-II reference stars were found in each chip, thus allowing an accurate absolute positioning. Then, a few hundred stars in common between the WFI and the *HST* FoVs have been used as secondary standards to place the *HST* catalogs on the same absolute astrometric system. At the end of the procedure the global uncertainties in the astrometric solution are of the order of $\sim 0\farcs2$, both in right ascension (α) and declination (δ).

The photometric calibration of the optical (B and V) magnitudes has been performed by using the Stetson Photometric Standard catalog[3]. After cross correlating the WFI and Stetson catalogs, we have used the stars in common for the calibration of the WFI B and V magnitudes. Then, the ACS V magnitudes have been converted to the WFI system by using the stars in common. Since the Stetson standard field does not overlap with the ACS FoV, the calibration of the ACS I magnitudes has been performed by using the stars in common with the catalog of (Desidera et al. 1998), after converting the latter to the Stetson photometric system. Finally, the WFPC2 m_{255} and U magnitudes have been calibrated to the (Holtzman et al. 1995) zero-points. The resulting CMDs, both in the UV and optical bands, are shown in Figures 3.3 and 3.4, respectively.

Unless otherwise specified, in the following analysis we adopt the combined *HST* catalog (ACS and WFPC2 data) for the cluster central regions (see Fig. 3.1), and the complementary WFI sample for the external parts.

3.1.3 Center of Gravity, and Density Profile

Given the absolute positions and the magnitudes of individual stars, the center of gravity $C_{\rm grav}$ has been determined by averaging the coordinates α and δ of all stars brighter than $V = 19$ lying in the FoV of WFI CCD $\#7$. We have chosen to use the WFI (instead of the *HST*) data, because in such a loose cluster the FoV of the WFPC2 planetary camera is too small to provide an adequately large sample for the accurate determination of the center of gravity, while the ACS FoV is crossed by the gap between the two chips. Following the iterative procedure described in Montegriffo et al. (1995), we have determined $C_{\rm grav}$ to be $\alpha({\rm J2000}) = 19^{\rm h}\,39^{\rm m}\,59\fs54$, $\delta({\rm J2000}) = -30^{\rm o}\,57'\,45\farcs14$, with a 1σ uncertainty of $0\farcs5$ in both α and δ. This value of $C_{\rm grav}$ is located $\sim 2''$ south-east ($\Delta\alpha = 2\farcs1$, $\Delta\delta = -1\farcs1$) from that previously derived by Harris et al. (1996) on the basis of the surface brightness distribution.

[2]Available at `http://www-gsss.stsci.edu/Catalogs/GSC/GSC2/GSC2.htm`.
[3]`http://www1.cadc-ccda.hia-iha.nrc-cnrc.gc.ca/community/STETSON/standards/`.

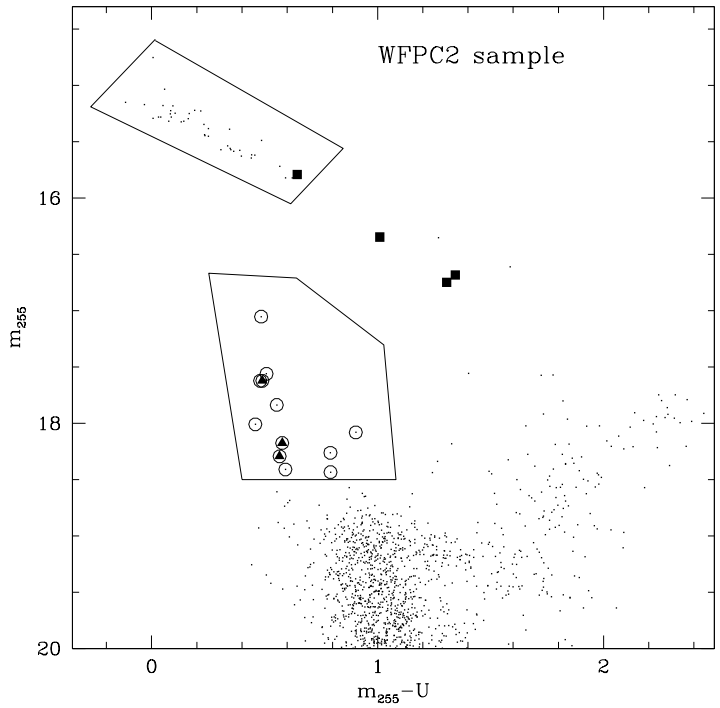

Figure 3.3: Ultraviolet CMD of the *HST*-WFPC2 sample. The adopted BSS and HB selection boxes are shown. The resulting fiducial BSS are marked with *empty circles*. *Triangles* correspond to the SX Phoenicis variables identified by Pych et al.(2001), while the *squares* mark the RRLyrae identified by Olech et al. (1999) and included in our HB sample.

By exploiting the optimal combination of high-resolution and wide-field sampling provided by our observations, we have determined the projected density profile by direct star counts over the entire cluster radial extent, from $C_{\rm grav}$ out to $\sim 1400'' \sim 23'$. To avoid biases due to incompleteness, we have considered only stars brighter than $V = 19$ from the ACS and the complementary WFI catalogs (see Fig. 3.4). The brightest red giant branch (RGB) stars that are strongly saturated in the ACS data set have been excluded from the analysis, but since they are few in number and the ACS pixel scale is only of $0.05''/pixel$, the effect on the resulting density profile is negligible. Following the procedure described in Ferraro et al. (1999a; 2004), we have divided the entire *HST*+WFI sample in 26 concentric annuli, each centered on $C_{\rm grav}$ and split in an adequate number of sub-sectors. The number of stars lying within each sub-sector was counted, and the star density was obtained by dividing these values by the corresponding sub-sector areas. The stellar density in each annulus was then obtained as the average of the sub-sector densities, and its standard deviation was estimated from the variance among the sub-sectors. The

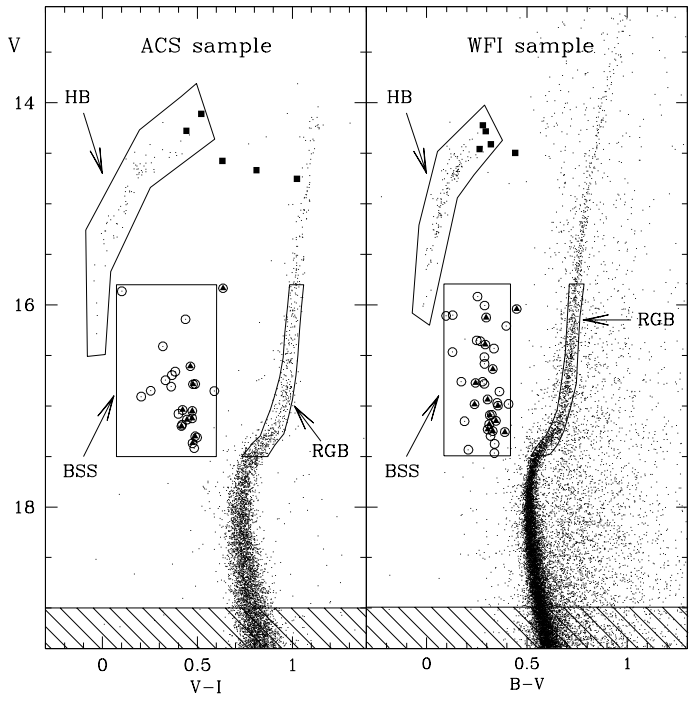

Figure 3.4: Optical CMDs of the *HST*-ACS and of the complementary WFI samples. The adopted BSS, HB, and RGB selection boxes are shown. Symbols are as in Figure 3.3. The hatched regions indicate the magnitude limit ($V \leq 19$) adopted for the computation of the cluster surface density profile.

radial density profile thus derived is shown in Figure 3.5, and the average of the three outermost ($r \gtrsim 17'$) measures has been used to estimate the background contribution (corresponding to ~ 3 stars arcmin^{-2}). Figure 3.5 also shows the best-fit mono-mass King model and the corresponding values of the core radius and concentration: $r_c = 114''$ (with a typical error of $\sim \pm 2''$) and $c = 1$, respectively. These values are in agreement with those quoted by McLaughlin & van der Marel (2005) ($r_c = 126\farcs4$ and $c = 0.93$), and by Irwin & Trimble (1984) ($r_c \sim 120''$ and $c \sim 1$). Concentration parameters as low as ~ 0.8 as quoted, e.g., by Z97 and Harris et al. (1996) provide significantly worse fits to the observed profile. The difference with respect to Z97 (who also computed the surface density profile by direct star counts), is probably due to the fact that their ground-based observations are saturated at $V \lesssim 14$, and have a pixel scale much larger than that of ACS, so they have lost a number of faint stars in the central regions of the cluster.

Assuming the distance modulus $(m - M)_0 = 13.82$ Ferraro et al. (1999b; $d \sim 5.8$ Kpc), our value of r_c corresponds to ~ 3.2 pc. These values can then be used to redetermine the other

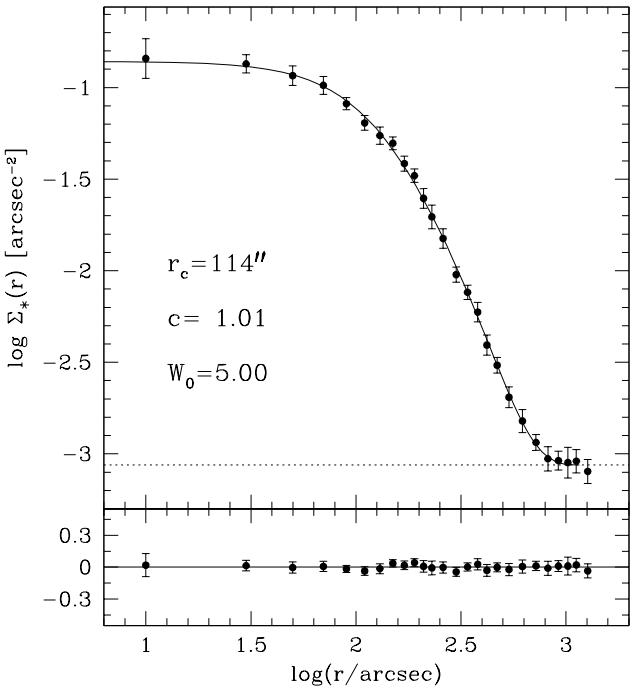

Figure 3.5: Observed surface density profile (*dots and error bars*) and best-fit King model (*solid line*). The radial profile is in units of number of stars per square arcseconds. The *dotted line* indicates the adopted level of the background, and the model characteristic parameters (core radius r_c, concentration c, dimensionless central potential W_0) are marked in the figure. The lower panel shows the residuals between the observations and the fitted profile at each radial coordinate.

structure parameters of the cluster. By assuming $\mu_0 = 19.13$ mag/arcsec^2 as the central surface brightness Harris et al. (1996), and $E(B-V) = 0.07$ as reddening Ferraro et al. 1999b), we estimate that the extinction-corrected central surface brightness of the cluster is $\mu_{V,0}(0) \simeq 18.91$ mag/arcsec^2. Following the procedure described in Djorgovski (1993) (see also Beccari et al. 2006a), we derive $\log \nu_0 \simeq 2.23$, where ν_0 is the central luminosity density in units of $L_\odot\,\mathrm{pc}^{-3}$. By assuming a mass-to-light ratio $M/L_V = 3$, the derived central mass density measured in $M_\odot/\mathrm{pc}^3$ is $\log \rho_0 = 2.7$, which is a factor ~ 1.6 higher than that quoted by Pryor & Meylan (1993). This value corresponds to $n_0 \simeq 1000$ stars pc^{-3} if a mean stellar mass of $0.5\,M_\odot$ is assumed.

3.2 Cluster Population Selection

3.2.1 The BSS Population

At UV wavelengths BSS are among the brightest objects in a GC, and RGB stars are particularly faint. By combining these advantages with the high-resolution capability of *HST*, the usual problems associated with photometric blends and stellar crowding are minimized, and BSS can be most reliably recognized and separated from the other populations in the UV CMDs (Ferraro et al. 2004). For these reasons our primary criterion for the definition of the BSS sample is based on the position of stars in the ($m_{255},\ m_{255}-U$) plane. In order to avoid incompleteness bias and to limit the possible contamination from TO and SGB stars, we have chosen a limiting magnitude of $m_{255}=18.5$ (roughly 1 magnitude brighter than the cluster TO). The adopted selection box and the resulting 12 BSS identified in the UV plane are shown in Figure 3.3. Once selected in the UV CMD, the BSS lying in the field in common with the ACS sample have been used to define the selection box and the limiting magnitude in the ($V,\ V-I$) plane. The latter is $V\simeq 17.5$, and the adopted selection box is shown in the left-hand panel of Figure 3.4. One of the BSS candidates (that lies close to the reddest edge of the box) has been rejected from the sample on the basis of its position in the UV plane, where it is ~ 0.2 magnitudes fainter than the adopted m_{255} limit and has a color of $m_{255}-U=1$, thus clearly belonging to the SGB star population. A total of 24 BSS have been identified within the ACS selection box, of which 11 are in common with the WFPC2 sample. Finally, in order to select the BSS population in the complementary WFI data set, we have adopted the same V magnitude limits as for the ACS sample. Since field star contamination is critical in M55, particularly in the external regions of the cluster, the definition of the $B-V$ color edges of the selection box has required a detailed study of the color-magnitude distribution of field stars. To do this, we have exploited both the outermost portion of the WFI observations (beyond the tidal radius), and the Galaxy model of Robin et al. (2003) in the direction of the cluster. In order to limit both the risk of field star and SGB blend contamination, we pick $B-V\simeq 0.41$ as a conservative value for the red-edge of the BSS selection box. As blue limit, we have chosen $B-V\simeq 0.08$. The adopted selection box in the ($V,\ B-V$) plane is shown in the right-hand panel of Figure 3.4, and the number of enclosed BSS is 38.

Since M55 is known to harbor a large population of SX Phoenicis (SX Phe) variables in the BSS region Pych et al. (2001), we have cross-correlated the SX Phe catalog with our data set. All of the 24 SX Phe identified by Pych et al. (2001) are contained in our sample (see *triangles* in Figs. 3.3 and 3.4), and all but two lie within our BSS selection boxes. The two outliers (V21

and V26 in their catalog) are indeed only slightly redder than the adopted limits, and most likely are genuine BSS (in fact, BSS frequently show the pulsating properties of SX Phe stars; see, e.g. Mateo 1996). Thus, they have been also included in our BSS sample. The SX Phe population of M55 is truly remarkable, second only to the always weird ω Centauri (Kaluzny et al. 2004). Considering that we have identified 56 BSS within the FoV in common with Pych et al. (2001) and that 24 of them are SX Phe variables, we see that almost half (43%) of the BSS in M55 are pulsating.

The coordinates and magnitudes of all the selected BSS (65) are listed in Table 3.1. Two candidate BSS (namely, BSS 64 and 65 in Table 3.1) lie at $r > r_t$. Since Z97 suggest that there is tidal distortion in the north-east direction, these BSS could be part of a cluster tidal tail. However, our observations do not indicate any significant distortion in the cluster stellar distribution (although a more extended mapping of the surrounding regions might be needed), and we therefore conclude that they probably are field stars. Thus, they are not encircled in the right-hand panel of Figure 3.4, and have not been considered in the following analysis.

No quantitative comparison between our selected BSS population and that presented in Z97 is possible, since they provide neither selection criteria nor the coordinates of the identified BSS. Within the FoV (the inner $4' \times 4'$) in common with Mandushev et al. (1997), we find 33 BSS; for comparison, by using the published BSS magnitudes, we have verified that 30 of their stars are included in our BSS selection boxes, thus showing a very good agreement between the two studies. The remaining 44 BSS identified by these authors are fainter and/or redder than the limits adopted in the present work.

3.3 The Reference Populations

To study the BSS projected radial distribution and detect possible peculiarities, a reference population which is representative of the normal cluster stars must be properly defined. For this purpose we have chosen the horizontal branch (HB) and the RGB populations, both of which are expected to have a non-peculiar radial distribution within the cluster.

The adopted HB selection boxes in the optical CMDs are shown in Figure 3.4, and are designed to include the bulk of this population. The box in the UV plane defined by the stars in common between the ACS and the WFPC2 samples is shown in Figure 3.3, and confirms the suitability of the adopted selection. By cross-correlating the coordinates of our catalog with the catalog of RR Lyrae variables detected by Olech et al. (1999) we have identified 10 stars (*filled squares* in Fig.

3.4) out of a total of 13, the remaining three falling in the gaps of the WFI chips.
The few RR Lyrae that lie outside the selection boxes have been also included in our HB sample. Thus, the total number of selected HB stars is 237 (78 in the ACS data set, and 159 in the WFI sample) [4]

In selecting the RGB sample, we have considered only the magnitude range $15.8 \leq V \leq 17.5$ (the same adopted for the BSS), since the brightest RGB stars are saturated in the ACS observations. We have drawn narrow selection boxes around the RGB mean ridge line in the CMDs, in order to limit the contamination by field stars. The adopted boxes are shown in Figure 3.4, and the resulting number of RGB stars found at $r \leq r_t$ is 1504.

3.3.1 Field Contamination

As apparent from the right-hand panel of Figure 3.4, field star contamination is a critical issue in the study of M55, particularly for the cluster outer regions. In order to estimate the impact of the field contamination on the cluster population selections, we have considered the CMD in the outermost ($r > r_t$) portion of the WFI data set. By considering that the sampled area is of $\sim 252\,\mathrm{arcmin}^2$, counts of stars within the adopted BSS, HB, and RGB selection boxes yield the number densities of field stars contaminating the selected cluster populations. As a further check, we have performed the same analysis on the synthetic data Galaxy model of Robin et al. (2003) in the B and V bands, considering a much larger area (1 square degree) in the direction of M55. The number densities derived from the two methods agree within a factor of $\sim$ 2–3, and we have finally adopted densities obtained from the Galaxy model, because of the much larger sampled area. The estimated contamination is roughly 8, 4, and 550 field stars per square degree for the selected populations of BSS, HB, and RGB stars, respectively. By using the V and I data of the synthetic Galaxy model, we have verified that the same values are also appropriate for decontaminating the cluster populations in the inner $202'' \times 202''$ (the ACS FoV) of our sample, where the selection has been performed in these photometric bands. The quoted values have been adopted in the following analysis to statistically decontaminate the star counts.

3.4 The BSS projected radial distribution

As for other clusters studied in a similar way (see references in Lanzoni et al. 2007b), we have searched for possible peculiarities in the BSS radial distribution by comparing it with that of HB

[4] Only one object lying in the HB box has been excluded because it is located at $r > r_t$

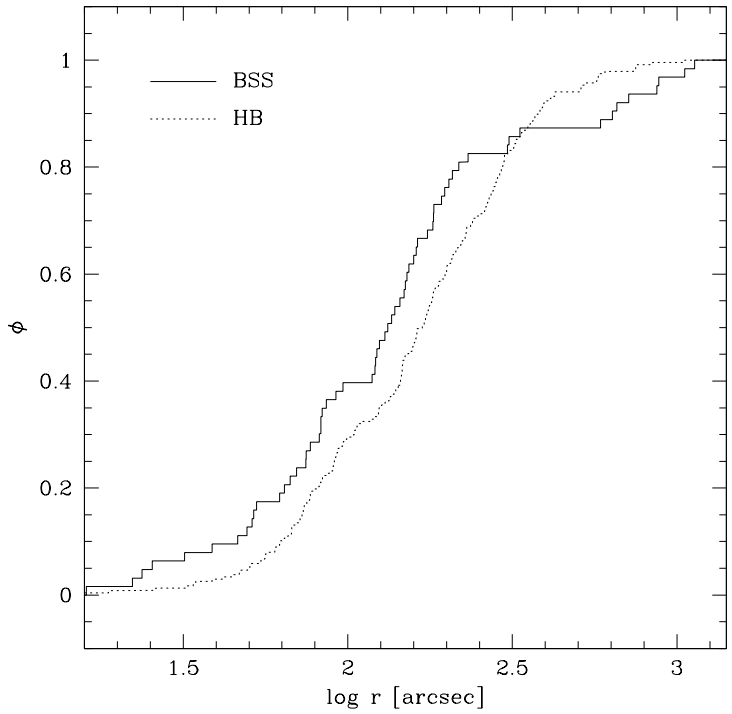

Figure 3.6: Cumulative projected radial distribution of BSS (*solid line*) and HB stars (*dotted line*).

and RGB stars, that are expected to be distributed as "normal" cluster stars.

We have used the Kolmogorov-Smirnov (KS) test to search for statistical differences between the cumulative projected radial distributions of BSS and HB stars (the comparison with the RGB population has not been performed because of the non-negligible degree of field star contamination). As shown in Figure 3.6, BSS appear to be more concentrated than normal cluster stars within $\sim 300''$ from the center, and less concentrated outward. The statistical significance of this result, however, is rather poor: the overall KS probability that BSS and HB stars are not extracted from the same parent population is ~ 0.90 (corresponding to $\sim 1.6\,\sigma$ significance level). If the analysis is restricted to the inner $300''$, BSS are more concentrated than HB stars at $\sim 1.9\,\sigma$ level. For $r > 300''$, where less than 20% of the total BSS and HB populations are located, the BSS are less concentrated at the $3\,\sigma$. A similar trend, with a similar statistical significance, was also found by Z97, who, however, performed the comparison with the RGB population.

For a more quantitative analysis, the surveyed area has been divided into 5 concentric annuli, and the number of BSS, HB, and RGB stars ($N_{\rm BSS}$, $N_{\rm HB}$, and $N_{\rm RGB}$, respectively) within each annulus has been counted. The resulting number counts have then been corrected for

field contamination by taking into account the fraction of annulus area effectively sampled by our observations, and the estimated density of contaminating field stars for each population (see previous section). The values thus obtained are listed in Table 3.2 and have been used to compute the specific frequencies $N_{\rm BSS}/N_{\rm HB}$, $N_{\rm BSS}/N_{\rm RGB}$, and $N_{\rm HB}/N_{\rm RGB}$. Since the number of stars in any post-MS stage is proportional to the duration of the evolutionary phase itself (Renzini & Buzzoni 1986), the specific frequencies $N_{\rm HB}/N_{\rm RGB}$ is expected to be constant and equal to the ratio between the evolutionary time scales of the HB phase and of the RGB portion in the magnitude range $15.8 \leq V \leq 17.5$, where the stars have been counted. In order to verify this, we have used the BASTi[5] evolutionary model library (Pietrinferni et al. 2006 and reference therein), selecting the $\alpha-$enhanced low-temperature opacities tracks computed for metallicities $[{\rm Fe/H}] = -1.84$ and $[{\rm M/H}] = -1.49$ (the closest to the observed values $[{\rm Fe/H}] = -1.61$ and $[{\rm M/H}] = -1.41$; Ferraro et al. 1999b). From these models we have estimated that the time spent by a 0.8 $M_{\odot}$ star along the RGB sequence in the range $15.8 \leq V \leq 17.5$ is $t_{\rm RGB} \sim 0.6$ Gyr, while the duration of the HB phase for a 0.63 $M_{\odot}$ is $t_{\rm HB} \sim 0.09$ Gyr; thus, $t_{\rm HB}/t_{\rm RGB} \simeq 0.15$, in good agreement with the observed value of the $N_{\rm HB}/N_{\rm RGB}$ ratio (see the *dotted line* in the lower panel of Figure 3.7).

A very similar result is also found by using the theoretical stellar tracks of the Pisa Evolutionary Library[6] (see references in Cariulo et al. 2004) , and it ensures that the selected (and decontaminated) HB and RGB populations are indeed representative of the normal cluster stars. As for the BSS, the specific frequency $N_{\rm BSS}/N_{\rm HB}$ shows a completely different projected radial distribution, with a clearly bimodal behavior: from a central value of ~ 0.4, the BSS specific frequency decreases to a minimum at about $4\,r_c$, and rises again at larger radii. A very similar trend (with the central peak at ~ 0.07) is also found for $N_{\rm BSS}/N_{\rm RGB}$, in agreement with Z97.

By integrating the density profile from the best-fit King model (see Sect.3.1.3), and assuming the values of central surface brightness, reddening and distance modulus quoted in Sect. 3.1.3, we have also computed the luminosity sampled in each annulus ($L^{\rm samp}$), and the total sampled luminosity ($L^{\rm samp}_{\rm tot}$) taking into account the incomplete spatial coverage of the most external annulus (see Fig. 3.2). The resulting ratios between these two quantities in each annulus are listed in Table 3.2, and have been used to compute the double normalized ratio (see Ferraro et al. 1993):

[5]Available at `http://www.te.astro.it/BASTI/index.php`
[6]Available at `http://astro.df.unipi.it/SAA/PEL/Z0.html`

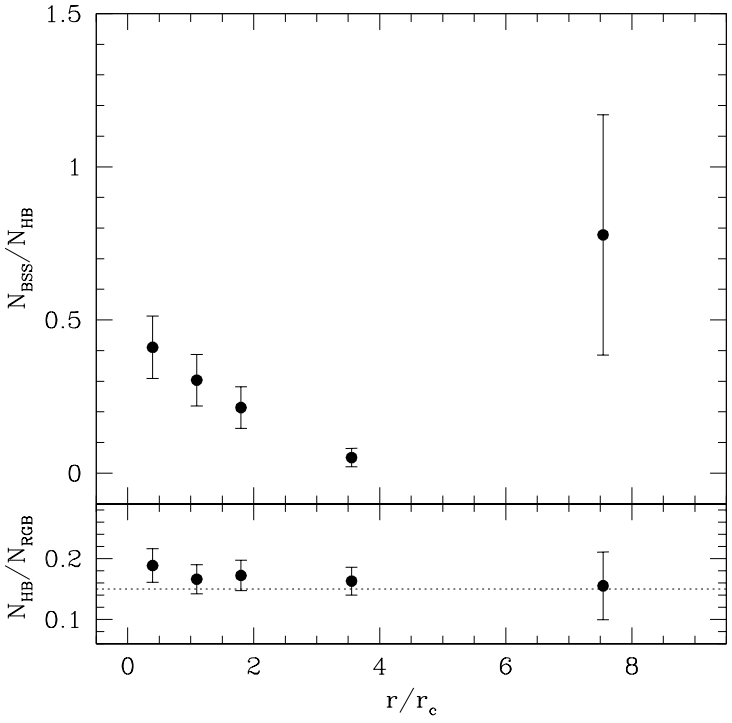

Figure 3.7: *Upper panel:* Projected radial distribution of the specific frequency $N_{\rm BSS}/N_{\rm HB}$, as a function the radial distance from the cluster center, expressed in units of the core radius. *Lower panel:* The same as above, for the specific frequency $N_{\rm HB}/N_{\rm RGB}$. The *dotted line* corresponds to the value (~ 0.15) predicted by the population synthesis models of Pietrinferni et al. 2006 for the ratio between the evolutionary time-scales of the HB and RGB (in the range $15.8 \leq V \leq 17.5$) phases.

$$R_{\rm pop} = \frac{(N_{\rm pop}/N_{\rm pop}^{\rm tot})}{(L^{\rm samp}/L_{\rm tot}^{\rm samp})}, \tag{3.1}$$

where $\rm pop =$ BSS, HB, RGB.

The radial trend of $R_{\rm HB}$ (as well as that of $R_{\rm RGB}$) is essentially constant, with a value close to unity (see Fig. 3.8). This is just what expected on the basis of the stellar evolution theory, which predicts that the fraction of stars in any post-MS evolutionary stage is strictly proportional to the fraction of the sampled luminosity (Renzini & Fusi Pecci 1988). Conversely, the trend of $R_{\rm BSS}$ is bimodal and indicates that, with respect to the sampled luminosity, the fraction of BSS is higher in the central regions and (particularly) in the cluster outskirts, and smaller at intermediate radii, with respect to the fraction of normal cluster stars.

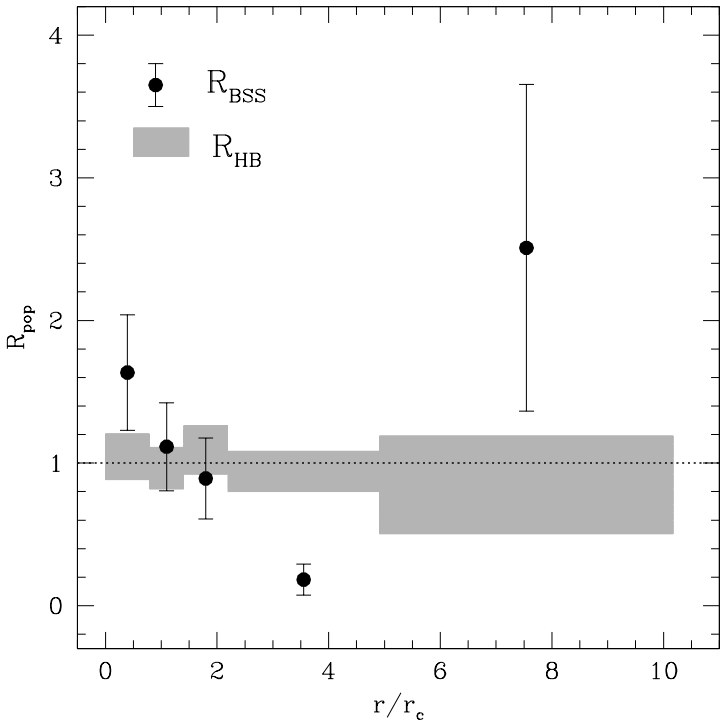

Figure 3.8: Projected radial distribution of the double normalized ratios of BSS (*dots*) and HB stars (*gray rectangles*), as defined in equation (3.1). The error bars (represented by the vertical sizes of the rectangles in the case of $R_{\rm HB}$) are computed as described in Sabbi et al. 2004. The *dotted line* corresponds to the value ($R_{\rm pop} = 1$) expected for any normal post-MS population in the cluster (see Sect.3.4).

3.5 Discussion

We have found that the BSS projected radial distribution in M55 is bimodal, i.e., peaked in the center, decreasing at intermediate radii, and rising again in the exterior. This is in agreement with the findings of Z97 from the analysis of a much smaller fraction of the cluster, and puts their result on much more solid statistical basis.

Such a bimodality is similar to that found in M3 (Ferraro et al. 1997), 47 Tuc (Ferraro et al. 2004), NGC 6752 (Sabbi et al. 2004), and M5 (Warren et al. 2006, Lanzoni et al. 2007a). As in those GCs, also in M55 the position of the observed minimum approximately corresponds to the radius of avoidance $r_{\rm avoid}$ of the system, i.e., the radius within which all the stars as massive as $1.2\,M_{\odot}$ (which is assumed to be the typical BSS mass) are expected to have already sunk to the core due to dynamical friction and mass segregation processes. In fact, by using the dynamical friction timescale formula (from, e.g., Mapelli et al. 2006) with the best-fit King model and the

central stellar density presented in Sect. 3.1.3, and assuming $\sigma \simeq 4.9\,\mathrm{km\,s^{-1}}$ as the central velocity dispersion (Pryor & Meylan 1993), and 12 Gyr as the cluster age, we estimate that $r_{\rm avoid} \simeq 4.5\,r_c$, in reasonable agreement with the position of the observed minimum.

The BSS specific frequency in the center of M55 ($N_{\rm BSS}/N_{\rm HB} \simeq 0.4$) is also similar to that measured in the other bimodal GCs (cfr. Fig.3.7, with Fig. 12 of Lanzoni et al. 2007a and see also Lanzoni et al. 2007b), where the central peak of the distribution is found to be mainly generated by COL-BSS (see also Mapelli et al. 2006). However, the central density in M55 is much lower (by a factor of 100 or more), and stellar collisions are expected to be less important in this system. Indeed, the cluster central density is quite similar to that of NGC 288 (only a factor of two higher), where most of the central BSS are thought to be MT-BSS (Bellazzini et al. 2002). A remarkable difference in the central value of $N_{\rm BSS}/N_{\rm HB}$ in these two low density clusters is however apparent. In fact, by considering only the brightest portion of the BSS population in NGC 288, (Ferraro et al. 1993) measured $N_{\rm BSS}/N_{\rm HB} \simeq 1$, which is the highest BSS frequency ever found in a GC (together with that of M80 Ferraro et al. 1999a) , it is more than twice that of M55. What is the origin of this difference? One possibility is a different primordial binary fraction. However, Sollima et al. 2007 have recently estimated that the binary fractions in the core of the two clusters are the same ($\sim 10\%$). Another possibility is a substantial difference in the collision rate. By using equation (14) from Leonard 1989, we estimate that the central binary-binary collision rate in M55 is only a factor of ~ 2 higher than that in NGC 288. Moreover, the binary survival rate (defined as the ratio between the formation and destruction rates; see Verbunt 2003) is about twice as high in M55 than in NGC 288. Thus, our results indicate that two clusters with similar environments (and collision rates) and similar primordial binary content can produce quite different central BSS populations. Unfortunately, the BSS study in NGC 288 was restricted to two WFPC2 frames, and an investigation covering the entire cluster extension is urged in order to compare the global BSS population and its radial distribution in the two systems.

Compared to the other bimodal GCs, the external rising branch in M55 is much more prominent. It is the largest upturn found to date ($N_{\rm BSS}/N_{\rm HB} \simeq 0.8 \pm 0.4$ compared to the previous maximum value of $\simeq 0.25 \pm 0.11$, found in 47 Tuc). This is even more surprising if we consider that only 10% of the total cluster light is contained between $r_{\rm avoid}$ and r_t in M55, while it amounts to 32% in the case of 47 Tuc. As discussed in Mapelli et al. 2006, (see also Lanzoni et al. 2007a), the external rising branch is thought to be made of MT-BSS, generated in binary systems evolving in isolation in the cluster outskirts (this finding is also confirmed by the recent N-body

simulations of Hurley et al. 2007). Thus, such a prominent upturn of the BSS distribution would imply a significantly higher primordial binary fraction in M55, compared to the other GCs. This seems in contrast with the results of Sollima et al. 2007, who measured the binary fractions in the core of 13 galactic GCs and found that M55 has one of the lowest fractions ($\sim 10\%$), with respect to the others, which range up to $\sim 50\%$ (in Terzan 7). However a better understanding of the evolution of the binary fraction in the core, as a function of the cluster dynamical age, is needed to better address this point. In fact, the theoretical expectations for the time evolution of the core binary fraction are still controversial: while Ivanova et al. 2005 suggest that such a fraction significantly decreases in time, the opposite trend is found by Hurley et al. 2007. Moreover, since a careful investigation of the BSS radial distribution has not yet been performed in any of the other remaining clusters studied by Sollima et al. 2007, a comprehensive comparison of the BSS population properties in these systems is not yet possible.

The nature of the central BSS and of those producing the external rising branch in M55 is thus an open question. Appropriate dynamical simulations and detailed spectroscopic studies (see, e.g., Ferraro et al. 2006a) are therefore urged. We defer such studies to a forthcoming paper, where the results of our entire sample of clusters will be compared and discussed.

Table 3.1: The BSS population of M55. The first 12 BSS have been identified in the WFPC2; BSS 2–26 are from the ACS observations, the first 11 being in common with the WFPC2 sample; BSS 27–65 are from the complementary WFI data set. BSS 64 and 65 lie beyond the cluster tidal radius, at $\sim 22'$ and $24'$ from the center, respectively, and have not been considered in the analysis of the BSS radial distribution. The last column list the corresponding SX Phe stars identified by Pych et al. 2001.

Name	RA[degree]	Dec[degree]	m_{255}	U	B	V	I	SX Phe
BSS 1	294.9998920	-30.9667245	18.26	17.47	-	-	-	-
BSS 2	294.9954953	-30.9396261	18.08	17.18	-	16.85	16.26	-
BSS 3	295.0121689	-30.9581611	17.05	16.57	-	16.14	15.71	-
BSS 4	294.9982015	-30.9483228	17.56	17.05	-	16.66	16.28	-
BSS 5	295.0166912	-30.9704646	17.62	17.14	-	16.69	16.33	-
BSS 6	295.0193344	-30.9660591	17.84	17.28	-	16.81	16.45	-
BSS 7	295.0045478	-30.9669382	18.01	17.55	-	16.91	16.70	-
BSS 8	295.0033265	-30.9834341	18.43	17.64	-	17.19	16.77	-
BSS 9	295.0104327	-30.9803687	18.41	17.82	-	17.42	16.93	-
BSS 10	295.0122305	-30.9747912	17.62	17.13	-	16.61	16.15	V41
BSS 11	295.0040550	-30.9659563	18.29	17.73	-	17.30	16.81	V31
BSS 12	294.9902115	-30.9506018	18.17	17.60	-	17.37	16.90	V19
BSS 13	294.9849393	-30.9719486	-	-	-	15.87	15.76	-
BSS 14	294.9748793	-30.9741471	-	-	-	16.41	16.09	-
BSS 15	294.9858796	-30.9600404	-	-	-	16.85	16.60	-
BSS 16	294.9702800	-30.9607749	-	-	-	17.08	16.68	-
BSS 17	295.0254214	-30.9727945	-	-	-	16.78	16.30	-
BSS 18	295.0100545	-30.9422429	-	-	-	16.75	16.41	-
BSS 19	295.0214094	-30.9804905	-	-	-	17.31	16.82	-
BSS 20	294.9951572	-30.9710352	-	-	-	16.78	16.31	V38
BSS 21	294.9921499	-30.9759958	-	-	-	17.04	16.62	V32
BSS 22	295.0285621	-30.9424951	-	-	-	17.05	16.58	V18
BSS 23	294.9788871	-30.9728224	-	-	-	17.12	16.65	V20
BSS 24	294.9751258	-30.9689860	-	-	-	17.14	16.69	V27
BSS 25	294.9941390	-30.9568945	-	-	-	17.20	16.78	V42
BSS 26	294.9927055	-30.9852788	-	-	-	15.84	15.20	V21
BSS 27	294.9793701	-31.0208092	-	-	16.17	15.92	-	-
BSS 28	294.7966919	-31.0010357	-	-	16.21	16.11	-	-
BSS 29	295.0544434	-30.8069954	-	-	16.23	16.10	-	-
BSS 30	295.0268860	-30.9911098	-	-	16.30	16.01	-	-
BSS 31	295.0368652	-30.9847641	-	-	16.60	16.47	-	-
BSS 32	295.0367126	-30.9545650	-	-	16.60	16.35	-	-
BSS 33	295.0966492	-30.9473000	-	-	16.61	16.21	-	-
BSS 34	294.9940796	-30.9063625	-	-	16.63	16.36	-	-
BSS 35	294.9552917	-30.9421539	-	-	16.77	16.43	-	-

(continued on next page)

Table 3.1 – continued from previous page

Name	RA[degree]	Dec[degree]	m_{255}	U	B	V	I	SX Phe
BSS 36	295.0687561	-30.9846306	-	-	16.81	16.52	-	-
BSS 37	295.0217285	-30.9895248	-	-	16.87	16.58	-	-
BSS 38	294.7169495	-30.9712677	-	-	16.93	16.76	-	-
BSS 39	294.9458923	-30.8814220	-	-	17.04	16.76	-	-
BSS 40	294.9922485	-30.6695671	-	-	17.07	16.78	-	-
BSS 41	295.0174561	-30.9149532	-	-	17.22	16.86	-	-
BSS 42	294.7818298	-31.0331841	-	-	17.32	16.97	-	-
BSS 43	294.7232361	-31.0292740	-	-	17.34	17.15	-	-
BSS 44	294.9502563	-30.7848854	-	-	17.39	16.98	-	-
BSS 45	294.9739380	-31.0131721	-	-	17.41	17.09	-	-
BSS 46	295.0329895	-30.9473553	-	-	17.62	17.30	-	-
BSS 47	294.6565247	-31.0778027	-	-	17.64	17.43	-	-
BSS 48	294.9787292	-30.9204979	-	-	17.72	17.38	-	-
BSS 49	294.9926758	-30.9187489	-	-	17.81	17.47	-	-
BSS 50	294.9646912	-30.9394836	-	-	16.42	16.13	-	V25
BSS 51	294.9772644	-30.9996738	-	-	16.69	16.39	-	V33
BSS 52	294.9597473	-30.9203262	-	-	16.97	16.64	-	V35
BSS 53	294.9522705	-30.9460793	-	-	17.02	16.77	-	V36
BSS 54	295.0324402	-31.0037651	-	-	17.24	16.94	-	V22
BSS 55	294.9576721	-30.9620571	-	-	17.22	16.98	-	V37
BSS 56	295.0382690	-30.9452572	-	-	17.35	17.00	-	V16
BSS 57	294.9394226	-30.9343033	-	-	17.41	17.09	-	V24
BSS 58	295.0471497	-30.9905624	-	-	17.49	17.15	-	V17
BSS 59	295.0498962	-31.0348148	-	-	17.49	17.18	-	V39
BSS 60	295.0078125	-30.9275074	-	-	17.54	17.23	-	V40
BSS 61	295.0041809	-31.0107975	-	-	17.58	17.25	-	V34
BSS 62	294.9658203	-30.9315720	-	-	17.65	17.26	-	V23
BSS 63	294.9459534	-30.9596825	-	-	16.49	16.04	-	V26
BSS 64	295.2062378	-30.6464367	-	-	17.82	17.41	-	-
BSS 65	295.1806946	-30.6018009	-	-	16.53	16.34	-	-

r_i''	r_e''	$N_{\rm BSS}$	$N_{\rm HB}$	$N_{\rm RGB}$	$L^{\rm samp}/L^{\rm samp}_{\rm tot}$
0	90	23	56	297 (1)	0.23
90	160	17	56	337 (2)	0.25
160	250	12	56	325 (5)	0.22
250	560	3	59	362 (33)	0.26
560	1160	7 (1)	9 (1)	58 (84)	0.04

Table 3.2: The values listed out of the parenthesis correspond to the number of stars assumed to belong to the cluster (and thus used in the analysis), while those in the parenthesis are estimated to be contaminating field stars (see Sect. 3.3.1).

Chapter 4

Multiwavelength photometry of the Globular Cluster M2

Based on the results published in:

Dalessandro, E.; Beccari, G.; Lanzoni, B.; Ferraro, F. R.; Rood, R. T.; Schiavon P.R.

submitted to ApJ

Abstract

We present a multiwavelength photometric analysis of the globular cluster M2. The data-set has been obtained by combining high-resolution (HST/WFPC2 and ACS) and wide-field (GALEX) space observations and ground based (MEGACAM-CFHT, EMMI-NTT) images. The photometric sample covers the entire cluster extension from the very central regions up to the tidal radius and beyond. It allows an accurate determination of the cluster center of gravity and other structural parameters derived from the star count density profile. Moreover we study the BSS population and its radial distribution. A total of 123 BSS has been selected, and their radial distribution has been found to be bimodal (highly peaked in the center, decreasing at intermediate radii and rising outward), as already found in a number of other clusters. The radial position of the minimum of the BSS distribution is consistent with the radius of avoidance caused by the dynamical friction of massive ($1.2M_{\odot}$) objects over the cluster age. We also searched for gradients in the red giant branch (RGB) and the asymptotic giant branch (AGB) populations. We found an overabundance of AGB stars within the core radius. Sohn et al.(1996) had previously found that the central region of M2 is bluer than the outer part. We confirm this result on the basis of resolved star photometry and we show that it is due to a deficit of very luminous RGB stars in the central region.

4.1 Observation and data reduction

4.1.1 The data sets

The present work is based on a combination of different high-resolution and wide-field data-sets. The high resolution set consists of a series of WFPC2 and ACS images taken at various wavelengths ranging from the UV to the optical bands. The WFPC2 images (Prop 8709, P.I. Ferraro) were obtained through the UV filters $F160BW$ and $F255W$ with total exposure times $t_{\rm exp} = 1800$ s and $t_{\rm exp} = 2000$ s respectively, and through the optical filters $F336W$ and $F555W$ with exposure times $t_{\rm exp} = 1800$ s and $t_{\rm exp} = 106$ s. The center of the cluster is located in the WF2 chip (pixel scale $\sim 0.1''\!.\mathrm{pixel}^{-1}$). The photometric reduction of these data was performed using ROMAFOT (Buonanno et al. 1983) a package developed to obtain accurate photometry in crowded regions and specifically optimized to handle under-sampled point spread functions (Buonanno & Iannicola 1989). The ACS data-set is a series of images in $F606W$ ($\sim V$) and $F814W$ ($\sim I$) with $t_{\rm exp} = 20$ s and $t_{\rm exp} = 20$ s (Prop. 10775, P.I. Sarajedini). The images were corrected for geometrical distortions and effective flux (Sirianni et al. 2005). The photometric reduction was performed using the photometric package SExtractor (Bertin & Arnouts 1996).

The wide field set is composed of data obtained with 3 different instruments:

a) EMMI-ESO-NTT – B and V images (with $t_{\rm exp} = 40$ s and $t_{\rm exp} = 20$ s) were taken with the ESO Multi Mode Instrument (EMMI) at the NTT during an observing run in July 2007 (P.I. Ferraro, Prop 079.D-0325). We used the EMMI Red CCD that is composed of 2 chips of 2048×4093 pixels each with a pixel scale of about $0.33''\!.\mathrm{pixel}^{-1}$ and an effective field of view (FOV) of about $9.0' \times 9.9'$. The images were corrected for bias and flat field by using standard IRAF tools. The data reduction was performed with SExtractor (Bertin & Arnouts 1996).

b) MEGACAM-CFHT – A combination of short and long MEGACAM exposures taken through the g ($t_{\rm exp} = 24$ s and $t_{\rm exp} = 240$ s) and r ($t_{\rm exp} = 48$ s and $t_{\rm exp} = 480$ s) filters was retrieved from the Canadian Astronomy Data Centre (CADC4). The wide field imager MEGACAM is mounted at Canadian-French-Hawaiian Telescope (CFHT) and consists of 36 CCDs of 2048×4612 pixels each. For this work we used two different pointings in which the cluster center is located between chip #27 and chip #36, and #19 and #28 respectively. This allowed a coverage of an area of $2 \times 1\ \mathrm{deg}^2$ and a complete sampling of the cluster well beyond its tidal radius. The data were pre-processed, astrometrized and calibrated by using

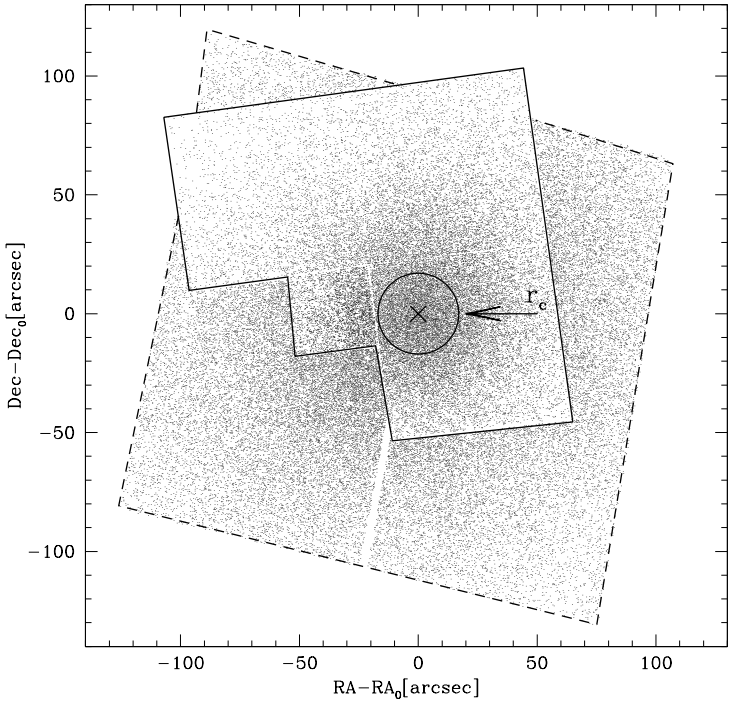

Figure 4.1: Map of the WFPC2 sample (solid line) and the ACS sample (dashed line) with the coordinates referred to the right ascension RA_0 and the declination Dec_0 of the cluster center of gravity (cross). The circle marks the core radius of the cluster as determined in Sect. 4.2.2.

the Elixir pipeline. We performed the data reduction using SExtractor (Bertin & Arnouts 1996). Each chip in each image was reduced separately and then combined with all the others for obtaining a catalog with g and r magnitudes and positions of the detected stars.

c) GALEX – A complete coverage of the cluster in the UV bands was obtained using GALEX data (FOV of about 1 deg^2) through the FUV (1350–1750Å) and NUV (1750–2800Å) detectors (program GI-056, P.I. Schiavon). Because of the high concentration of M2 and the low angular resolution of the GALEX channels ($4''$ in FUV and $6''$ in NUV) we used the GALEX data only for $r \geq 200''$ from the center of gravity (see below). The reduction of GALEX data was performed independently for each filter with DAOPHOTII/ALLFRAME (Stetson 1987).

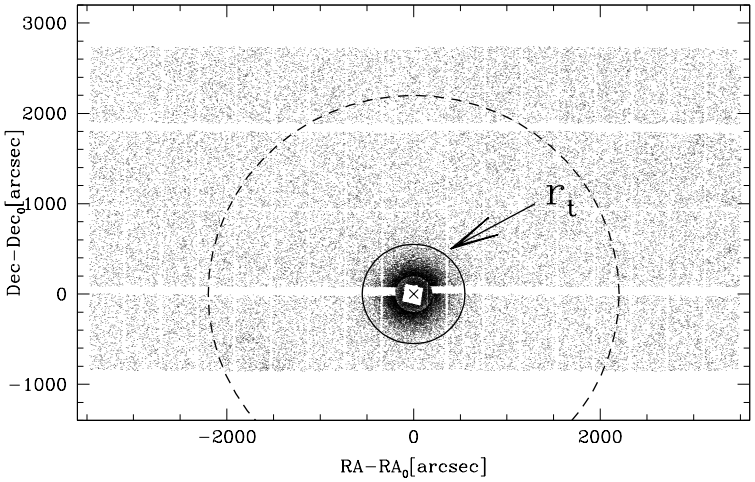

Figure 4.2: Map of the EMMI and MEGACAM/GALEX sample. The circle with radius $r_t = 550''$ marks the estimated tidal radius, while the dashed circle indicates the GALEX FOV.

4.2 Definition of the photometric catalogs

4.2.1 Astrometry and photometric calibration

All the catalogs were put on the absolute astrometric system using a large number of stars in common with the Sloan Digital Sky Survey (SDSS) catalog. As a first step we obtained the astrometric solution of the 72 chips of MEGACAM by using the procedure described in Ferraro et al. (2001, 2003) and a specific cross-correlation tool. All the stars in common with the GALEX, EMMI and HST samples were then used as secondary astrometric standards in order to put all the catalogs in the same astrometric system. Several hundred astrometric standards have been found in each step, allowing a very precise astrometry for each catalog. At the end of the procedure the estimated error in the absolute positions, both in right ascension (α) and declination (δ) is about $0.2''$.

All the WFPC2 magnitudes (m_{160}, m_{255}, m_{336} and m_{555}) were calibrated in the STMAG system using the equations and zeropoints listed in Holtzmann et al. (1995) and the same procedure described in Ferraro et al. (1997, 2001). Then the stars in common between the

other catalogs and the WFPC2 sample were used to transform all the magnitudes to the same photometric system. In particular, the $F606W$ of the ACS catalog, the EMMI instrumental V magnitudes and MEGACAM g magnitudes were transformed to the V STMAG by using appropriate color equations. The EMMI B instrumental magnitudes were put in the STMAG system. The ACS $F814W$ magnitudes were calibrated in the STMAG system using the prescriptions of Sirianni et al. (2005), and the r MEGACAM mag was transformed to the SDSS system. The GALEX instrumental FUV and NUV magnitudes were calibrated to STMAG system using the stars in common with the WFPC2.

4.2.2 Center of Gravity

The center of gravity has been obtained following the procedure adopted in our previous works (see for example Lanzoni et al. 2007b). A first estimate of the cluster center was performed by eye on the WF2 chip of the WFPC2 image, then the exact measure of $C_{\rm grav}$ was obtained by means of an iterative procedure that averages the absolute positions of stars lying within $\sim 10''$ from the first guess center. In order to avoid biases and spurious effects, we considered two samples with two different limiting magnitudes ($V < 19.7$ and $V < 19.2$). The values of $C_{\rm grav}$ obtained with the two samples agree within $1''$. We adopt the mean value as the best estimate of $C_{\rm grav}$: $\alpha = 21^{\rm h}33^{\rm m}27^{\rm s}$ $(RA = 323.3623340)$ and $\delta = -0°49'22.8''$ $(Dec = -0.82304665)$. This new determination is substantially different from the center reported by Harris et al. (1996) on the basis of the surface brightness profile and using photographic plates: our $C_{\rm grav}$ is located at $\sim 35''$ west ($\Delta\alpha \sim 35''$, $\Delta\delta \sim 0''$) from Harris center.

4.2.3 Sample definition

Once all the data-sets have been photometrically homogenized and put in the same reference frame, and the cluster center has been determined, we have built a single catalog by combining the following sub-samples: *i)* the WFPC2 sample, composed of all the stars detected in the WFPC2 FOV; *ii)* the ACS sample, comprising all the stars in the ACS FOV complementary to the WFPC2 one; *iii)* the EMMI sample, complementary to the previous two and including only stars with distance $r < 200''$ from $C_{\rm grav}$ and *iv)* the MEGACAM/GALEX sample made of stars with $r \geq 200''$ included in the MEGACAM FOV (of course only a fraction of these stars also has GALEX magnitudes). The criteria used for these definitions have been chosen to sample the highly crowded central regions of the cluster with the highest spatial resolution and UV band data (thus to maximally limit the effects of photometric errors and stellar blends), while covering the

entire cluster extension by means of wide-field images. The maps of the adopted samples are shown if Figurs 4.1 and 4.2. In Fig. 4.3 the ($V,\ U-V$) CMD of the WFPC2 sample is shown.

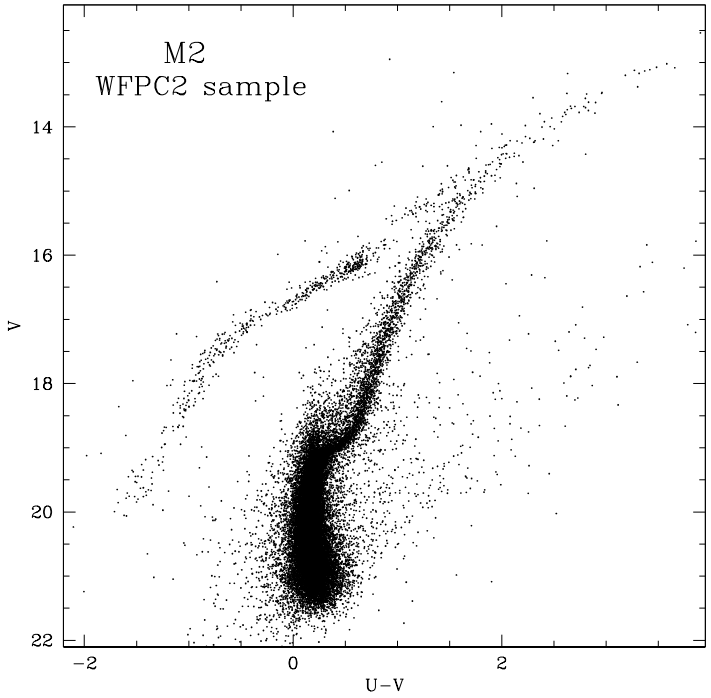

Figure 4.3: The ($V,\ U-V$) CMD of the WFPC2 sample.

4.2.4 Density profile

We have determined the projected density profile of M2 by measuring the star counts over the entire cluster extension. Only stars with $15.2 < V < 19.2$ in the combined sample, covering the cluster extension from $C_{\rm grav}$ to $r = 1800''$ were considered. The area was divided in 36 annuli all centered on $C_{\rm grav}$. Each annulus was divided into an adequate number of sub-sectors in which the stellar density has been calculated as the ratio between the number of stars and the sub-sector area. For each annulus the resulting density is given by the average of the corresponding sub-sector densities and the error is quoted as the square root of the variance of the sub-sector densities. In this procedure we have also taken into account the incomplete area coverage of the most external annuli and the largest CCD gap in the MEGACAM FOV.

The observed density profile is plotted in Fig. 4.4. The sample nicely covers the entire cluster extension. The four outermost annuli (with $r > 600''$) show a flattening of star counts giving

a direct estimate of the stellar background in the cluster direction: for $15.2 < V < 19.2$ the background star density is ~ 0.7 stars/arcmin^2. The observed profile is well reproduced by an isotropic single-mass King model with concentration $c \simeq 1.51$ and core radius $r_c \simeq 17''$. The corresponding tidal radius is $r_t \simeq 550''$. Since there is an uncertainty of about 15% in the determination of r_t, in our analysis below we will consider all stars lying within $r < 650''$. The newly determined cluster parameters are substantially different from those reported by Harris et al. (1996) based on the luminosity center and the surface brightness distribution ($c = 1.8$ and $r_c = 20''$) and from the even higher concentration model found by Pryor & Meylan (1993; $c = 1.9$ and $r_c = 20''$). As shown in Fig. 4.4 (dashed line), a King model with the parameters quoted by Harris et al. (1996) does not reproduce the observed profile. On the contrary, a reasonable agreement (within the errors) is found with the values estimated by McLaughlin & van der Marel (2005; $c = 1.59$ and $r_c = 19''$). Assuming a distance modulus $(m - M)_V = 15.49$ and a reddening $E(B - V) = 0.06$ (Harris et al. 1996) we find a real distance $d \simeq 12.5$ kpc, and a core radius $r_c \simeq 1.02$ pc.

The best-fit model reproduces the observed profile out to $400''$ very well, while at larger distances the observed star counts show an excess with respect to the model. While this discrepancy is not statistically significant, it deserves further investigation since it could be the signature of tidal distortion in the outer regions (see Leon et al. 2000 for more details). Another interesting feature of density profile is that the innermost point seems to deviate from the canonical flat-core King model. This is also worthy of future investigation since similar features might be related to the presence of an intermediate mass-black hole (e.g. Miocchi 2007, Lanzoni et al. 2007d).

4.3 The BSS and reference population selection

4.3.1 The BSS selection

In this section we describe the procedure that we have followed to select the BSS population and to construct the BSS radial distribution in M2. At the UV wavelengths, hot populations like BSS and extreme-HB stars are the brightest objects, while cool populations (like RGB stars) appear quite faint (see Fig. 4.5). Because of this, we always prefer to use the UV-CMD as the reference plane for the BSS selection. Moreover, since the HST spatial resolution dramatically reduces problems connected with crowding and blends, we have primarily selected the BSS population by considering the WFPC2 sample in the (m_{255}, $m_{255} - U$) plane. In order to avoid contamination

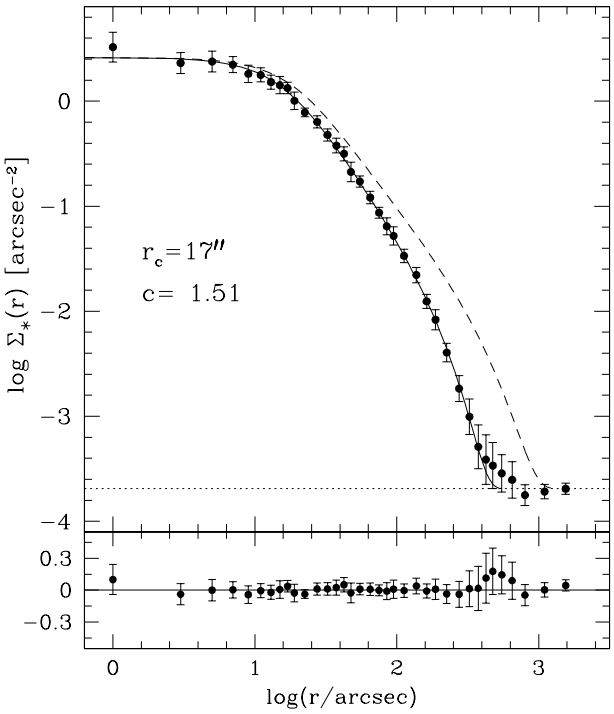

Figure 4.4: Observed surface density profile (dots and error bars) and best-fit King model (solid line). The radial profile is in units of number of stars per square arcsecond. The dotted line indicates the adopted level of the background (corresponding to 0.7 stars arcmin^{-2} in the range $15.2 < V < 19.2$). The model parameters are $r_c = 17''$ and $c = 1.51$. The lower panel shows the residuals between the observations and the fitted profile. The dashed line is the King-model obtained using the structural parameters quoted by Harris et al. (1996; see Sect. 4.2.4.

from the SGB stars, we selected only stars with $m_{255} < 19.55$, that is about 1 magnitude brighter than the TO point ($m_{255} \simeq 20.5$). The number of BSS thus selected in the WFPC2 sample is 82.

As in previous studies, we used the UV-selected BSS in common with the ACS sample to define a selection box in the (V, $V-I$) plane. We have adopted a limiting magnitude $V \sim 19.2$, and the red edge is at $(V-I) = 0.55$ (see Fig. 4.6). The total number of BSS found in the ACS sample is 20.

In the EMMI catalog the BSS have been selected in the (V, $B-V$) CMD, using the same cut in the V filter as for ACS sample. Considering the quality of the diagram the color limit was set to $(B-V) < 0.32$ to avoid spurious detections and blends from TO and SGB stars: 9 BSS have been selected in this way (see Fig. 4.7). In the most external region sampled by our observations ($r \geq 200''$) the combination of the MEGACAM and the GALEX samples allows

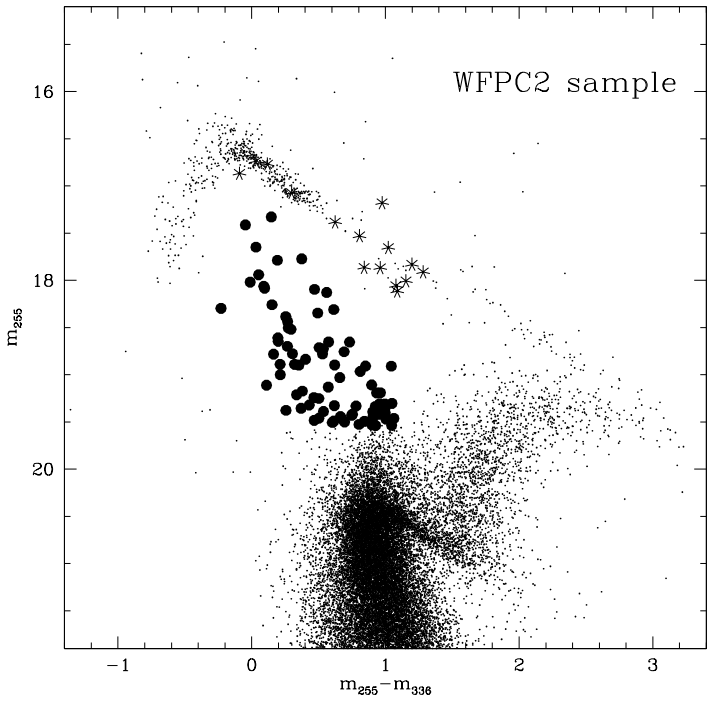

Figure 4.5: Ultraviolet CMD of the WFPC2 sample. The selected BSS population is marked as filled dots, and RR Lyrae stars as asterisks.

the construction of an UV CMD. Since both the GALEX NUV and the HST m_{255} magnitudes have been calibrated on the STMAG photometric system (see Sect. 4.2.1), we have used the same threshold ($NUV < 19.55$) adopted for the WFPC2 sample to define the selection box in the (NUV, $NUV - V$) plane. The result is shown in Fig. 4.8, where 12 BSS have been selected for $r \geq 200''$. The right panel of Fig. 4.8 shows the location of the selected BSS in the (V, $V - r$) plane. In summary a total of 123 BSS have been selected in M2 (see Table 4.1).

4.3.2 The reference populations

As discussed in other papers (see Ferraro 2006 and references in Dalessandro et al. 2008a) we also need to select a reference population which is representative of the "normal" cluster population. As in other works of this series, we have used the HB and RGB stars as reference populations. The selection of the RGB stars has been performed in the optical planes. For all of the samples a magnitude cut at $V < 18$ has been adopted. However for our analysis only stars with $V > 16$ were used in order to avoid saturated stars in the ACS and MEGACAM/GALEX sample (Fig. 4.6 and

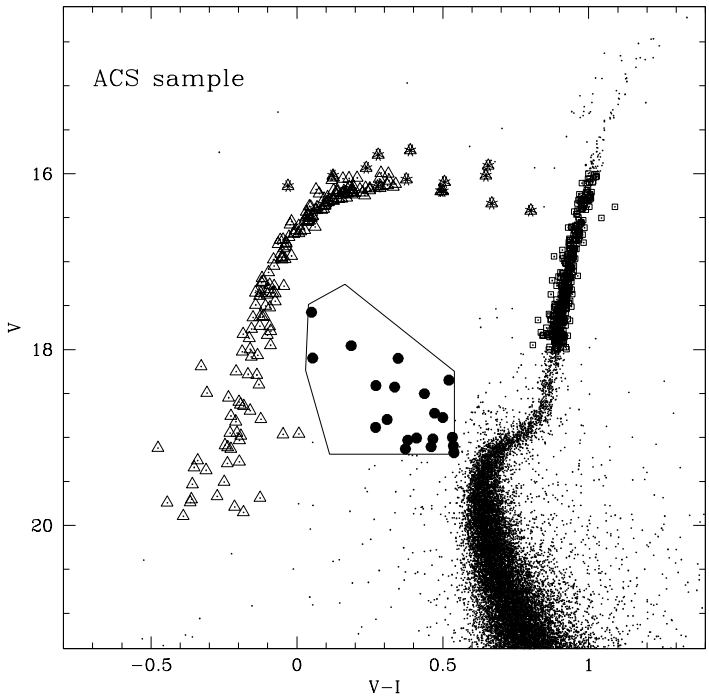

Figure 4.6: (V, $V-I$) CMD of the ACS sample. The different stellar populations discussed in the paper are marked with different symbols (same as in Fig. 4.5 plus squares and triangles for the RGB and HB stars respectively).

Fig. 4.8). The color limits of the selection boxes have been chosen to follow the RGB ridge mean line in each CMD while avoiding regions with high probability of field star contamination (the selected RGB stars are marked with empty squares in Fig. 4.6, 4.7 and 4.8). We found 2121 RGB within $r < 650''$ (1223 in WFPC2, 460 in ACS, 270 in EMMI and 168 in MEGACAM/GALEX samples, respectively). The magnitude range of the RGB reference population is the same as that adopted for the "faint" RGB discussed below.

In the WFPC2 and MEGACAM/GALEX samples the HB stars have been selected on the basis of their positions in the (m_{255}, $m_{255}-V$) and (NUV,NUV-V) CMDs respectively (see left panel of Fig. 4.8 for the wide-field sample). The positions in the optical MEGACAM/GALEX plane of the selected HB stars (Fig. 4.8 right panel) have been used to define the selection box for the ACS and EMMI samples (see Figs. 4.6 and 4.7). By cross-correlating our catalog with the catalogs of RR Lyrae stars found by Lee & Carney (1999) and Lazaro et al. (2006), we have identified all of the 42 known variables (they are marked as asterisks in Fig. 4.5, 4.6, 4.7 and 4.8) and we have

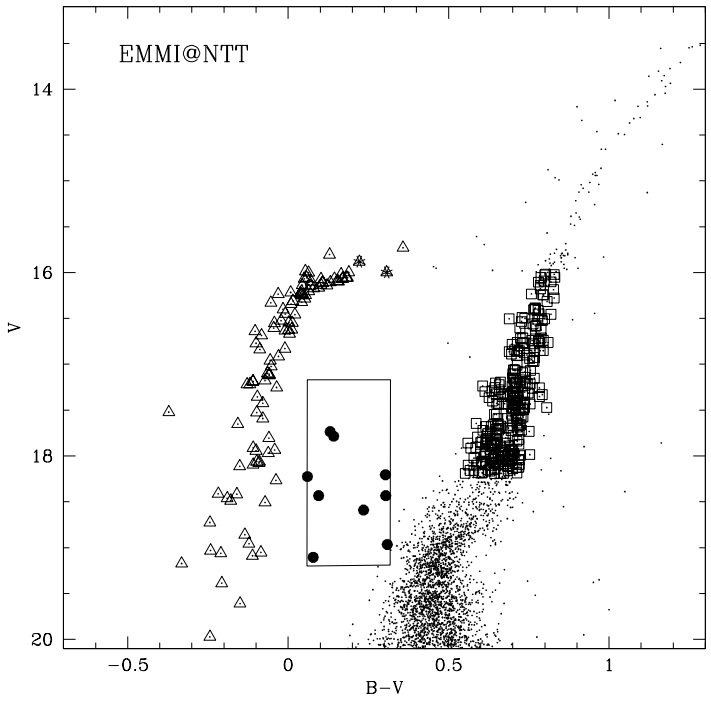

Figure 4.7: Optical CMD of the EMMI sample. The symbols have the same meaning as in Fig. 4.6.

included them in our HB sample. The total number of HB stars within $r < 650''$ is 875 (525 in WFPC2, 184 in ACS, 104 in EMMI and 62 in MEGACAM/GALEX samples).

4.4 Results

4.4.1 The BSS radial distribution

Having defined the reference populations we can now examine the BSS radial distribution. The BSS cumulative radial distribution is shown in Fig. 4.9 with the distributions of the HB and RGB stars shown for comparison. The BSS population is more segregated in the central regions and less concentrated in the outer parts than either the HB and the RGB stars. The KS test gives a probability of $\sim 10^{-6}$ (4σ significance level) that the radial distribution of the BSS is extracted from the same parent distribution of the reference population.

For a more quantitative analysis we computed the population ratios $N_{\rm BSS}/N_{\rm HB}$ and $N_{\rm BSS}/N_{\rm RGB}$ (where $N_{\rm pop}$ is the number of stars belonging to a given population) in 6 concentric annuli centered on $C_{\rm grav}$. To do this we had to evaluate the impact of field star contamination on

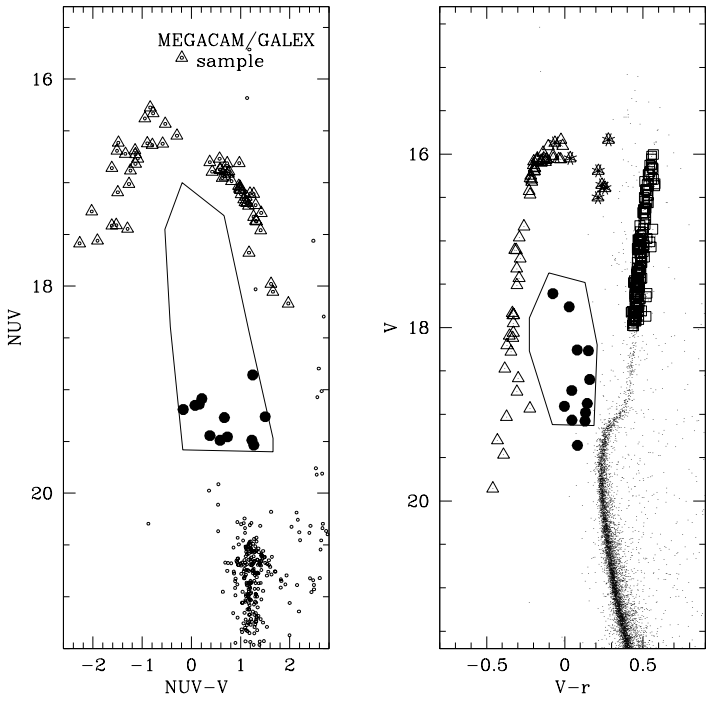

Figure 4.8: Ultraviolet (left panel) and optical (right panel) CMDs of the MEGACAM/GALEX sample. The NUV magnitudes have been obtained by matching the optical data with GALEX observations. The symbols have the same meaning as in Fig. 4.6.

each population. The field stars predominantly lie in a vertical sequence at $0.2 < (V - r) < 0.5$ and dramatically affect the RGB population . An estimate of the field star contamination can be directly obtained from our sample by considering an annulus at $1900'' < r < 2400''$ ($\sim 70\%$ of which is sampled by the MEGACAM data) far beyond the tidal radius of the cluster ($r_t \sim 550''$). We counted the number of field stars in this annulus lying within the BSS, HB and RGB selection boxes shown in Figs. 4.6, 4.7, and 4.8, and we derived the following values for their density: $\rho_{\rm BSS} \sim 0.01$ stars/arcmin^2, $\rho_{\rm RGB} \sim 0.06$ stars/arcmin^2, while no field stars have been found within the HB selection box. These values have been used to statistically decontaminate the star counts in each annulus.

The star counts for each annulus are listed in Table 4.2. These values have been used to compute the ratios $N_{\rm BSS}/N_{\rm HB}$ and $N_{\rm BSS}/N_{\rm RGB}$. The radial distribution of these ratios is shown in Fig. 4.10 (central and upper panels, respectively). They are clearly bimodal, with a high BSS frequency in the central and outer regions, and with a broad minimum at about $120''$ ($\sim 9r_{\rm c}$) from

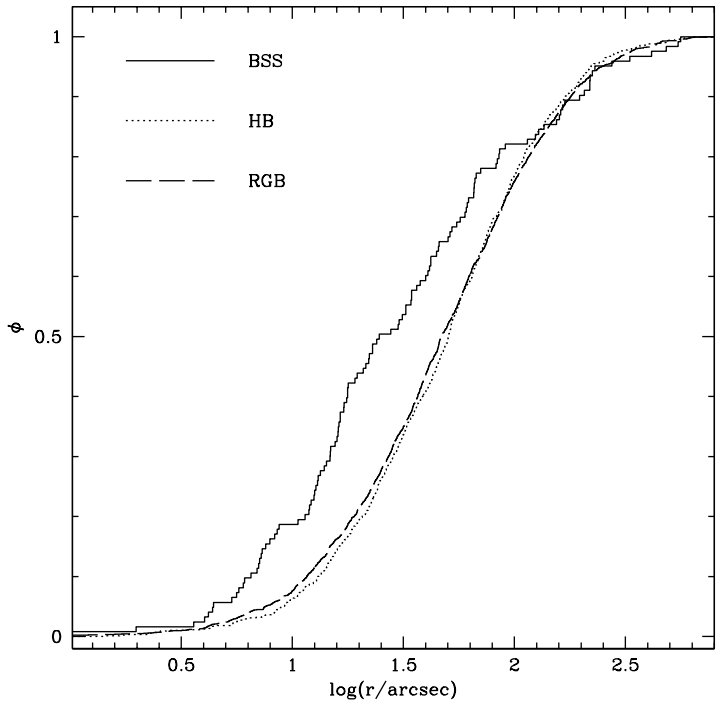

Figure 4.9: Cumulative radial distribution of BSS (solid line), HB (dotted line) and RGB (dashed line) stars as a function of the projected distance from $C_{\rm grav}$.

$C_{\rm grav}$. On the contrary the $N_{\rm HB}/N_{\rm RGB}$ ratio (plotted in the bottom panel of Fig. 4.10) shows a flat distribution across the cluster extension, as expected for "normal" populations.

As a further confirmation of the BSS bimodality, we also computed the double normalized ratio as defined in Ferraro et al. (1993):

$$R_{\rm pop} = \frac{N_{\rm pop}/N_{\rm pop}^{\rm tot}}{L^{\rm samp}/L_{\rm tot}^{\rm samp}}. \tag{4.1}$$

where pop = BSS, HB. The total sampled luminosity ($L_{\rm tot}^{\rm samp}$), as well as the luminosity sampled in each annulus ($L^{\rm samp}$), has been estimated from the King model by using the cluster structural parameters, distance modulus and reddening quoted in Section 4.2.4, and the central surface brightness reported by Harris et al. (1996). The incomplete spatial coverage due to the largest ($\sim 1'$) gap between the MEGACAM CCDs has been taken into account. As shown in Fig. 4.11, $R_{\rm HB}$ is constant with a value close to 1 out to $r = 650''$. This is just as expected: the fraction of HB (as any post-MS) stars is proportional to the fraction of sampled light, as shown in Renzini & Fusi Pecci (1988). Conversely the radial distribution of the BSS double normalized ratio ($R_{\rm BSS}$)

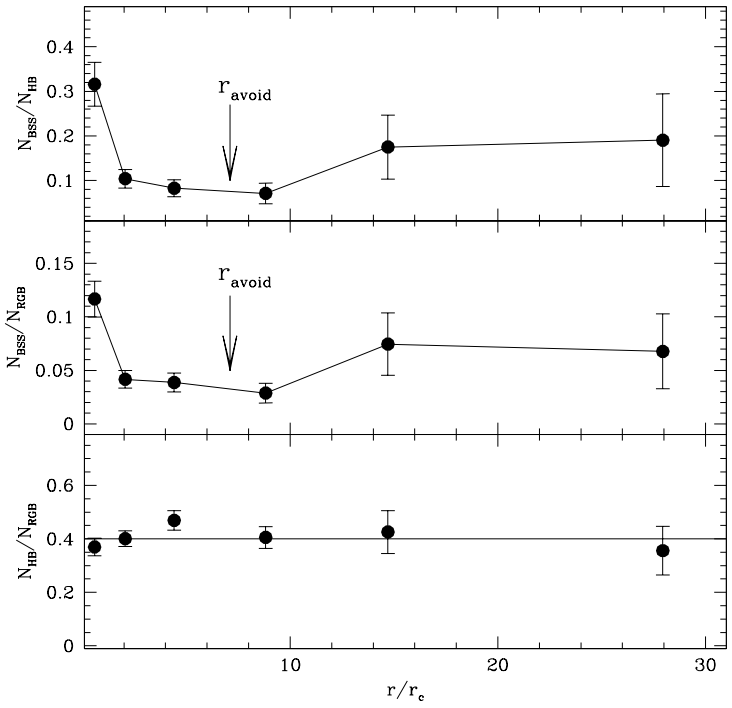

Figure 4.10: Radial distribution of the population ratios $N_{\rm HB}/N_{\rm RGB}$, $N_{\rm BSS}/N_{\rm HB}$ and $N_{\rm BSS}/N_{\rm RGB}$ as a function of the radial distance from the cluster center, expressed in units of the core radius. The arrows mark the position of the radius of avoidance (see Sect. 4.4.1).

confirms the bimodal behaviour: it is peaked in the central regions, decreases to a minimum value at about $9r_c$ and then rises again in the cluster outskirts.

The location of this minimum at $r \sim 9r_c$ can be related to the dynamical evolution of the cluster and in particular to the radius of avoidance ($r_{\rm avoid}$). This parameter is defined as the radius within which all the stars as massive as $1.2M_{\odot}$ (the assumed mass for BSS) have already sunk to the center because of mass segregation (Mapelli et al. 2004, 2006). Using the dynamical friction time-scale formula (e.g. Mapelli et al. 2006) under the assumption of a cluster age $t = 12\,{\rm Gyr}$, a central velocity dispersion of $\sigma_0 = 8.2\,{\rm km\,s^{-1}}$ (Pryor & Meylan 1993), we obtained $r_{\rm avoid} \sim 7r_c$. This position is fully compatible with the position of the observed minimum.

4.4.2 The AGB problem

Beccari et al. (2006a) found a significant overabundance of AGB stars in the very central regions of 47 Tuc. This excess could be due to contamination of genuine AGBs by massive (1.1–1.5 $M_{\odot}$) objects in late evolutionary stages (e.g. in the horizontal branch phase, as suggested by Sills et al.

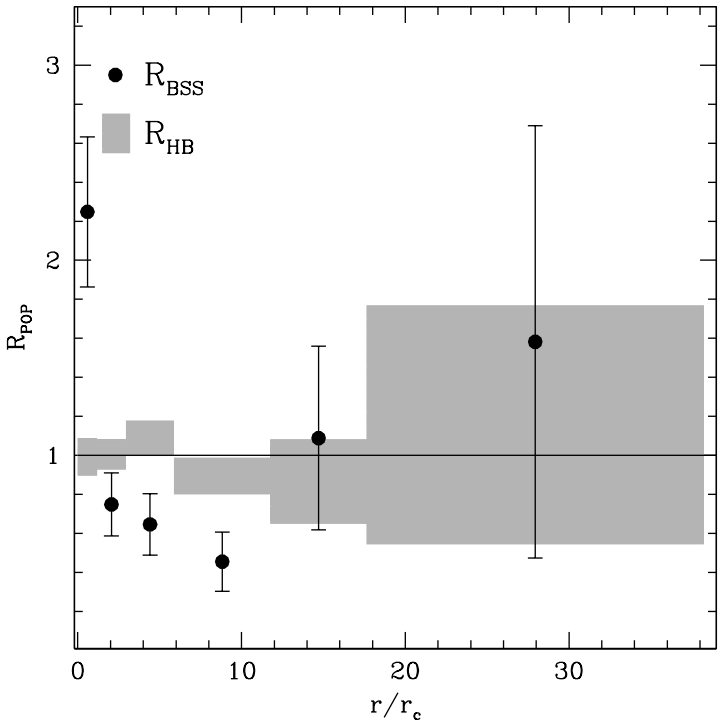

Figure 4.11: Radial distribution of the doubled normalized ratio of BSS (large dots) and HB stars (grey rectangular regions). The vertical size of the grey rectangles correspond to the error bars.

2008). Presumably these objects arise from binary systems (mainly BSS) segregated in the cluster core because of dynamical effects. To search for a similar result in M2, we used the WFPC2 and the EMMI sample where the brightest evolutionary sequences are well defined up to the RGB tip at $V \sim 13$. We selected AGB stars in the (V, $U-V$) plane for the WFPC2 sample and in the (V, $B-V$) for the EMMI sample as shown in Fig. 4.12. It was not possible to use either the ACS or the MEGACAM/GALEX samples because of saturation problems.

To study the radial distribution we divided the covered region into 5 concentric annuli centered on $C_{\rm grav}$ and counted the number of AGBs and HBs lying in each annulus. It was not possible to do a statistical decontamination of the AGB population because the MEGACAM/GALEX sample saturates at $V \sim 15.5$. However, we would expect that in the central regions it does not appreciably affect the observed radial distribution. Fig. 4.13 upper panel shows the behaviour of the population ratios $N_{\rm AGB}/N_{\rm HB}$ as a function of the distance from the cluster center. As apparent from the figure, while the mean value of the 4 outermost annuli is $\sim 0.12 \pm 0.03$, fully consistent with the value expected from the evolutionary timescales (Renzini & Fusi Pecci 1988),

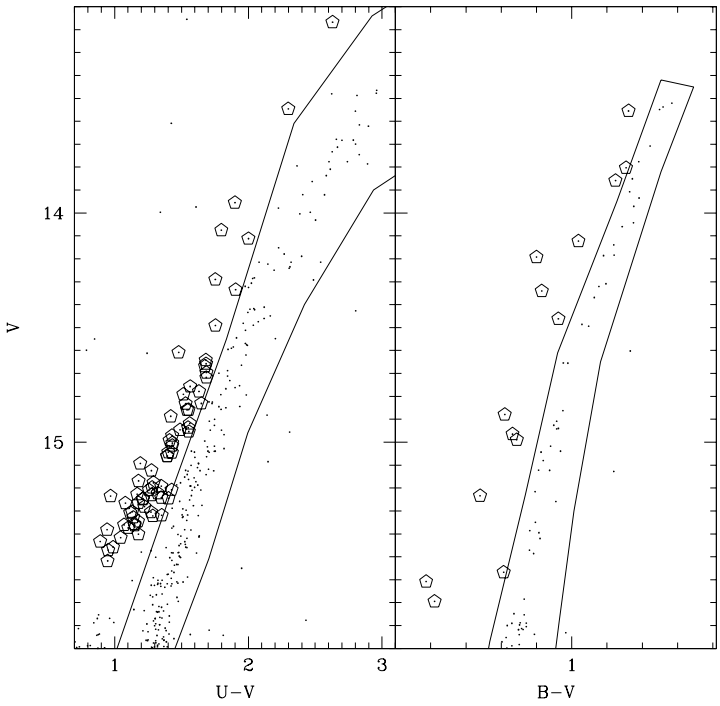

Figure 4.12: Brightest portion of the (V, $U-V$) CMD for the WFPC2 sample (left panel) and of (V, $B-V$) CMD for the EMMI sample (right panel). The selected AGB stars are marked as pentagons.

the ratio turns out to be higher ($\sim 0.19 \pm 0.03$) in the innermost annulus (corresponding to r_c). This central overconcentration of the AGB population corresponds to an excess of about 30% (or 9-10 more stars) in the first annulus. This value is compatible with the life-times and populations ratios computed by Sills et al. (2008) for evolved collisional products, supporting the idea of a possible contamination by evolved BSS. To further investigate this feature we also computed the double normalized ratio. The incomplete spatial coverage has been taken into account. The radial distribution of $R_{\rm AGB}$ (see Fig. 4.13 bottom panel) fully confirms this behaviour, showing a central peak ($R_{\rm AGB} \sim 1.4$) within r_c, while in the outer part the ratio remains constant at $R_{\rm AGB} \sim 1$ fully in agreement with $R_{\rm HB}$.

Purely on the basis of small number statistics introduced by binning, the AGB central peak is marginally significant ($< 2\sigma$). However the significance of the peak can also be evaluated with a KS test on the cumulative distribution, which is shown in Fig. 4.14. The probability that the AGBs are drawn from a different distribution from the HBs is 93% ($\sim 1.8\sigma$). The BSS distribution is also

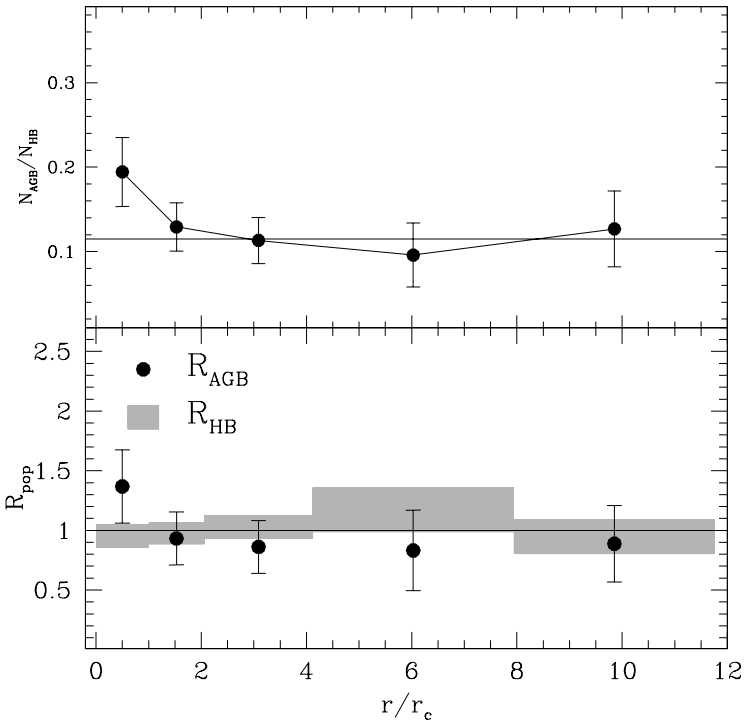

Figure 4.13: Radial distribution of the population ratios $N_{\rm AGB}/N_{\rm HB}$ (upper panel) and double normalized ratio (bottom panel) for AGB (dots) and HB (grey rectangles) as a function of the distance from $C_{\rm grav}$ in units of the core radius. The vertical size of the grey rectangles corresponds to the error bars.

shown in Fig. 4.14. While AGBs are more concentrated than HBs, they are less concentrated than BSS, with a 98% probability that they are extracted from a different parent family. In this respect they are different from the AGBs in 47 Tuc where AGBs and BSS have similar radial distributions.

4.4.3 Color gradients

Sohn et al. (1996), hereafter S96, found that M2 has a radial color gradient, in the sense that the central regions are bluer than the outer parts, with a variation of about $(B-V) \sim 0.1$. To investigate this interesting feature we computed the $(U-V)$ integrated color within $90''$ from $C_{\rm grav}$ which approximately corresponds to the region used by S96. We divided the WFPC2 sample in 5 concentric annuli (the first corresponding to r_c), and computed the color of each annulus from the resolved stars by considering three different magnitude cuts: $V < 16$, $16 \leq V < 20$ and $V < 20$. As shown in Fig. 4.15 (upper panel) we found that when only the brightest stars are included ($V < 16$, black and open dots in Fig. 4.15) a color difference $\Delta(U-V) \sim 0.18$ between the center

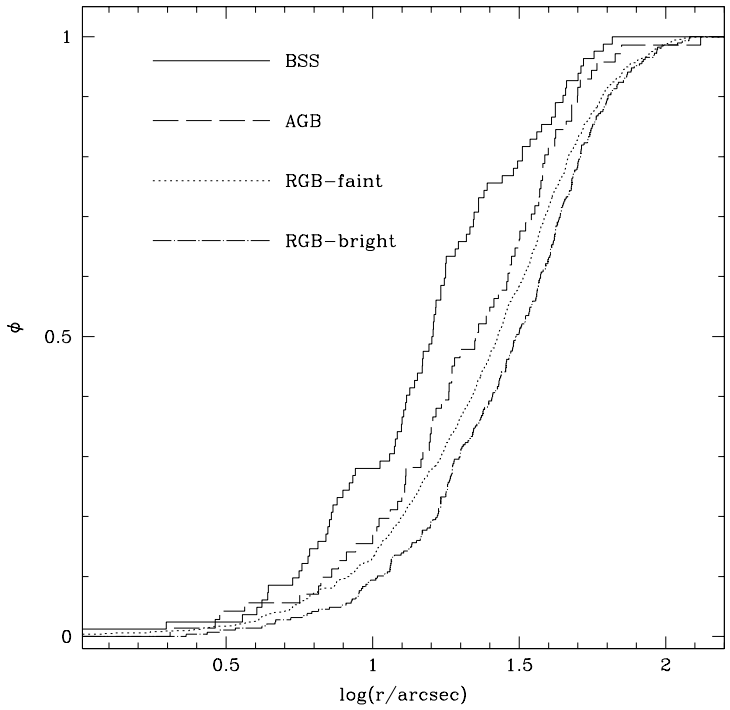

Figure 4.14: Cumulative radial distribution of BSS, AGB, bright-RGB and faint-RGB as selected in the WFPC2 sample.

(bluer) and the outer annuli is apparent. Even if this is a less than 2σ result, it is consistent with the finding of S96. When also fainter stars are included (i.e. for $V < 20$), the color gradient decreases, and if the brightest stars are excluded ($16 \leq V < 20$) it completely disappears and $(U-V)$ remains constant all over the considered radial range. To further investigate this behaviour we made the same computation for the ACS sample using the $(V - I)$ color. In this sample saturation occurs at about $V = 15$, so the test is limited to the population with $16 < V < 20$. No color gradient is visible in the bottom panel of Fig 4.15. Our results therefore indicate that the observed color gradient is due to the brightest stars and not to an over-concentration of BSS or blue faint objects. This seems in disagreement with the conclusion of S96, who found the color gradient only when using resolved stars with $V < 16$. However, as already discussed by these authors, the poor seeing conditions and the spatial resolution of the instrument ($0.56''\,\mathrm{pixel}^{-1}$) used in their analysis did not allow them to sample all the populations with acceptable photometric accuracy.

To more deeply understand the origin of the detected color gradient, we further investigated the properties of the brightest populations in the very central regions of M2. Since the AGB is

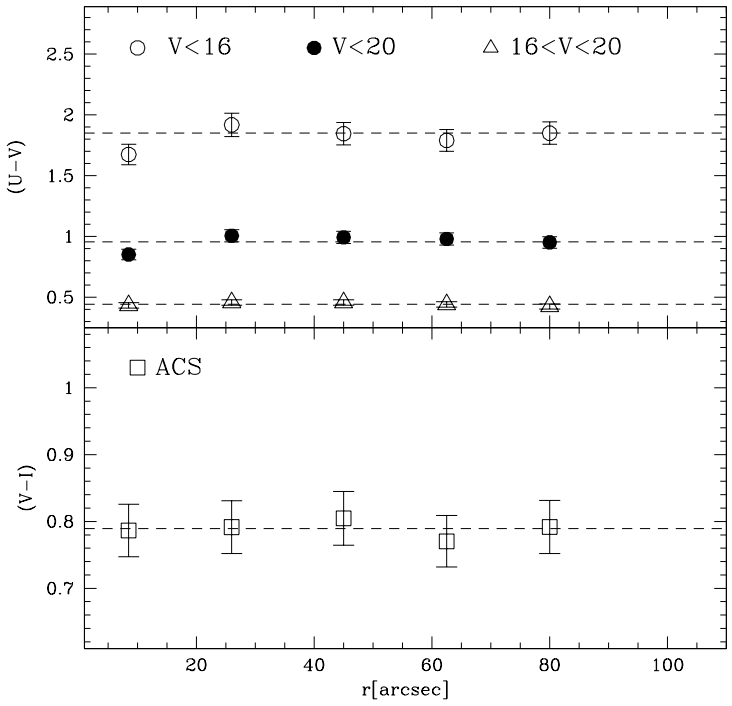

Figure 4.15: Top panel: radial distribution of the $(U-V)$ color computed from the WFPC2 resolved stars, for three different magnitude cuts (see labels). The dashed lines mark the average color computed from the four most external points. Lower panel: same for the $(V-I)$ color computed from the ACS sample.

0.2-0.3 mag bluer than the RGB in $(U-V)$, we first investigated whether the AGB central excess (Sect. 4.4.2) could account for the observed color gradient. We therefore artificially cancelled the AGB central peak, by randomly excluding 10 stars from the innermost bin, and re-computed the central color: this still yields a center bluer than the exterior. Very bright RGB stars therefore remain the only candidates. In order to test this hypothesis we compared the radial distribution of the brightest portion of the RGB ($V < 16$) in the WFPC2 sample (see Fig. 4.12, left panel) to the faint ($V \geq 16$) one. The radial distributions of these populations clearly show that the brightest giants are less concentrated than the faintest ones, with a 99% probability (about 2.5σ) that they are extracted from a different parent family (see Fig. 4.14 and the upper panel of Fig. 4.15). We have therefore re-computed the central color after having artificially increased the number of bright RGBs in the innermost bin, thus to flatten the radial distribution of the bright-to-faint RGB ratio (to this purpose, we have randomly extracted 25 bright RGBs from the observed luminosity function). This completely removes the color gradient (bottom panel of Fig. 4.15). Hence we conclude the

the color gradient found by S96 and confirmed here is due to a deficit of bright RGB stars in the center rather than a surplus of fainter blue stars.

4.5 Summary

The BSS population of M2 can be characterized as what is emerging as *"normal"*: a bimodal radial distribution with a minimum in the zone of avoidance, and with a value of the central BSS specific frequency ($N_{\rm BSS}/N_{\rm HB}$) which is also typical. Bimodal distributions are a very common feature of the Galactic GC BSS populations (Dalessandro et al. 2008a). Only two clusters, NGC 2419 and ω Cen, deviate significantly from this pattern. Both of these systems are very large. There is even some doubt that ω Cen is a true GC (Bekki & Freeman 2003). Of the bimodal clusters only two, NGC 6388 (Dalessandro et al. 2008a) and NGC 5024 (Beccari et al. 2008), have minima in their BSS radial distributions which differ significantly from $r_{\rm avoid}$. Presumably this arises because of a lower efficiency of the dynamical friction in these two clusters, for reasons yet to be explained.

As Beccari et al. (2006a) found for 47 Tuc, we find an excess of AGB stars in the center of M2. Because of the smallish sample size, the excess is only marginally significant, and unlike in 47 Tuc, the AGB population is not as concentrated as the BSS one.

In agreement with S96 we find that the integrated color of the central region of M2 is bluer that the exterior. We show that this color gradient is due to a deficit of bright RGB stars, and not to an excess of faint blue objects, such as BSS or HB stars. A similar deficit of bright RGB stars has also been found in the very massive GC NGC 2808 (Sandquist et al. 2007). They do not explore the radial dependence of their result, and neither of the two mechanisms they discuss for producing a deficit (neutrino losses and extra mass loss) would have an obvious radial dependence. We view our AGB surplus and bright RGB deficit as suggestive and worthy of followup in other clusters. It would be highly desirable that future photometric studies of GCs were designed in such a way that unsaturated photometry of the brightest stars was possible.

Table 4.1: The BSS population of M2

Name	RA[degree]	Dec[degree]	m_{255}	U	B	V	I	r
BSS 1	323.3714411	-0.8178864	18.296	18.526	-	17.276	15.678	-
BSS 2	323.3696276	-0.8177717	17.413	17.460	-	17.828	16.353	-
BSS 3	323.3634359	-0.8316575	18.095	17.625	-	17.147	16.653	-
BSS 4	323.3622994	-0.8218842	18.652	18.077	-	17.638	16.720	-
BSS 5	323.3596901	-0.8205591	17.787	17.595	-	17.394	17.256	-
BSS 6	323.3604809	-0.8240422	18.654	17.922	-	17.589	16.988	-
BSS 7	323.3586469	-0.8235375	18.128	17.567	-	17.444	17.301	-
BSS 8	323.3646741	-0.8224144	18.519	18.225	-	17.880	17.171	-
BSS 9	323.3647064	-0.8187827	18.756	18.065	-	17.704	17.179	-
BSS 10	323.3684421	-0.8221813	18.965	18.154	-	17.809	17.175	-
BSS 11	323.3743785	-0.8154098	18.908	18.057	-	17.797	17.199	-
BSS 12	323.3631231	-0.8183633	17.772	17.398	-	17.120	17.135	-
BSS 13	323.3623206	-0.8242631	18.018	18.029	-	17.823	17.685	-
BSS 14	323.3639051	-0.8281268	18.258	18.106	-	17.810	17.600	-
BSS 15	323.3588726	-0.8234170	18.083	17.987	-	17.776	17.613	-
BSS 16	323.3653858	-0.8152311	19.303	18.254	-	17.926	17.216	-
BSS 17	323.3615362	-0.8236454	18.062	17.972	-	17.874	17.697	-
BSS 18	323.3580481	-0.8224657	19.360	18.365	-	18.476	17.324	-
BSS 19	323.3651272	-0.8239863	18.437	18.168	-	17.906	17.759	-
BSS 20	323.3505252	-0.8278143	17.940	17.888	-	17.829	17.758	-
BSS 21	323.3666814	-0.8216585	18.725	18.190	-	18.049	17.499	-
BSS 22	323.3608046	-0.8242143	18.896	18.276	-	18.088	17.417	-
BSS 23	323.3645416	-0.8237411	19.309	18.312	-	18.142	17.381	-
BSS 24	323.3486643	-0.8180583	18.780	18.250	-	17.961	17.727	-
BSS 25	323.3619854	-0.8210425	18.609	18.413	-	18.166	17.670	-
BSS 26	323.3590958	-0.8195844	19.444	18.781	-	18.201	17.310	-
BSS 27	323.3686913	-0.8255542	18.503	18.230	-	18.063	17.831	-
BSS 28	323.3642889	-0.8229899	19.500	18.605	-	18.346	17.412	-
BSS 29	323.3636626	-0.8218238	19.533	18.632	-	18.500	17.511	-
BSS 30	323.3618965	-0.8244621	19.430	18.682	-	18.550	17.494	-
BSS 31	323.3645099	-0.8323754	19.389	18.852	-	18.517	17.527	-
BSS 32	323.3636755	-0.8072825	18.836	18.433	-	18.142	17.980	-
BSS 33	323.3657166	-0.8279525	18.777	18.473	-	18.200	17.920	-
BSS 34	323.3611863	-0.8196342	18.889	18.569	-	18.232	17.905	-
BSS 35	323.3579516	-0.8224698	19.331	18.551	-	18.351	17.631	-
BSS 36	323.3590562	-0.8178549	18.699	18.432	-	18.176	18.019	-
BSS 37	323.3613701	-0.8154069	19.393	18.488	-	18.321	17.673	-
BSS 38	323.3668016	-0.8209522	19.242	18.777	-	18.479	17.629	-
BSS 39	323.3597941	-0.8254617	19.130	18.557	-	18.335	17.824	-
BSS 40	323.3661322	-0.8254125	18.646	18.448	-	18.330	18.127	-
BSS 41	323.3610070	-0.8215795	19.526	18.724	-	18.373	17.752	-
BSS 42	323.3623248	-0.8235960	19.418	18.665	-	18.604	17.826	-

(continued on next page)

Table 4.1 – continued from previous page

Name	RA[degree]	Dec[degree]	m_{255}	U	B	V	I	r
BSS 43	323.3637456	-0.8191804	19.500	18.805	-	18.550	17.965	-
BSS 44	323.3649401	-0.8188352	19.466	18.793	-	18.640	18.015	-
BSS 45	323.3639143	-0.8195230	19.173	18.794	-	18.548	18.147	-
BSS 46	323.3614854	-0.8261032	19.212	18.876	-	18.673	18.270	-
BSS 47	323.3653940	-0.8262986	18.889	18.677	-	18.602	18.350	-
BSS 48	323.3636094	-0.8187332	19.462	18.399	-	18.029	17.954	-
BSS 49	323.3703157	-0.8145398	19.506	18.903	-	18.665	18.277	-
BSS 50	323.3602190	-0.8345394	19.483	19.016	-	18.791	18.361	-
BSS 51	323.3601378	-0.8229104	19.111	19.000	-	19.421	18.632	-
BSS 52	323.3528976	-0.8074247	18.385	18.130	-	20.235	18.370	-
BSS 53	323.3519143	-0.8095657	19.190	18.228	-	18.042	19.210	-
BSS 54	323.3633727	-0.8106859	18.898	18.546	-	19.888	19.325	-
BSS 55	323.3622427	-0.8090928	19.356	18.987	-	-	19.177	-
BSS 56	323.3620338	-0.8104039	18.712	18.208	-	15.777	19.532	-
BSS 57	323.3648729	-0.8120021	18.909	17.865	-	16.890	19.772	-
BSS 58	323.3695432	-0.8159710	18.782	18.619	-	20.927	19.384	-
BSS 59	323.3696150	-0.8177490	17.328	17.181	-	16.852	-	-
BSS 60	323.3662335	-0.8244178	18.309	17.695	-	17.217	-	-
BSS 61	323.3577723	-0.8227478	18.346	17.853	-	17.466	-	-
BSS 62	323.3623052	-0.8246038	17.648	17.616	-	17.901	-	-
BSS 63	323.3656601	-0.8182961	19.191	18.257	-	18.009	-	-
BSS 64	323.3637405	-0.8239484	19.108	18.211	-	18.110	-	-
BSS 65	323.3585287	-0.8219793	19.307	18.350	-	18.134	-	-
BSS 66	323.3560959	-0.8207169	19.030	18.371	-	18.188	-	-
BSS 67	323.3641747	-0.8257777	19.336	18.411	-	18.269	-	-
BSS 68	323.3636246	-0.8241400	19.418	18.470	-	18.287	-	-
BSS 69	323.3641677	-0.8222208	19.536	18.490	-	18.305	-	-
BSS 70	323.3607973	-0.8234748	19.377	18.415	-	18.378	-	-
BSS 71	323.3633715	-0.8234670	19.465	18.562	-	18.402	-	-
BSS 72	323.3634901	-0.8234524	19.251	18.749	-	18.546	-	-
BSS 73	323.3683405	-0.8208891	18.999	18.786	-	18.564	-	-
BSS 74	323.3606431	-0.8178698	19.472	18.467	-	18.579	-	-
BSS 75	323.3657301	-0.8176387	19.493	18.650	-	18.589	-	-
BSS 76	323.3633587	-0.8209047	19.321	18.891	-	18.732	-	-
BSS 77	323.3649179	-0.8208760	19.491	18.878	-	18.744	-	-
BSS 78	323.3648497	-0.8252105	19.327	18.709	-	18.787	-	-
BSS 79	323.3622419	-0.8265946	19.461	18.959	-	18.858	-	-
BSS 80	323.3627198	-0.8189658	19.377	19.121	-	19.042	-	-
BSS 81	323.3621778	-0.8228222	19.538	18.612	-	-	-	-
BSS 82	323.3645597	-0.8274454	19.404	18.406	-	-	-	-
BSS 83	323.3610603	-0.8382443	-	-	-	18.097	18.043	-
BSS 84	323.3393973	-0.8228098	-	-	-	18.348	17.827	-
BSS 85	323.3460753	-0.8143716	-	-	-	18.427	18.092	-
BSS 86	323.3572856	-0.8478265	-	-	-	18.724	18.252	-

(continued on next page)

Table 4.1 – continued from previous page

Name	RA[degree]	Dec[degree]	m_{255}	U	B	V	I	r
BSS 87	323.3660478	-0.8408961	-	-	-	18.998	18.465	-
BSS 88	323.3470995	-0.8411325	-	-	-	19.017	18.551	-
BSS 89	323.3441953	-0.8202620	-	-	-	19.007	18.597	-
BSS 90	323.3484068	-0.8546253	-	-	-	19.095	18.559	-
BSS 91	323.3667036	-0.8301313	-	-	-	17.576	17.526	-
BSS 92	323.3787647	-0.8319397	-	-	-	17.956	17.770	-
BSS 93	323.3817364	-0.8368805	-	-	-	18.101	17.754	-
BSS 94	323.3698348	-0.8318011	-	-	-	18.410	18.139	-
BSS 95	323.3712416	-0.8373826	-	-	-	18.502	18.065	-
BSS 96	323.3696574	-0.8290844	-	-	-	18.773	18.273	-
BSS 97	323.3771084	-0.8359012	-	-	-	18.796	18.487	-
BSS 98	323.3746327	-0.8342835	-	-	-	18.885	18.615	-
BSS 99	323.3854244	-0.8201446	-	-	-	19.031	18.651	-
BSS 100	323.3680668	-0.8325097	-	-	-	19.106	18.646	-
BSS 101	323.3695032	-0.8293585	-	-	-	19.173	18.635	-
BSS 102	323.3795559	-0.8221806	-	-	-	19.130	18.758	-
BSS 103	323.3896247	-0.9723055	18.857	-	-	17.608	-	17.684
BSS 104	323.3788152	-0.9135828	19.261	-	-	17.761	-	17.732
BSS 105	323.3622100	-0.8838157	19.488	-	-	18.258	-	18.178
BSS 106	323.5156768	-0.8517169	19.536	-	-	18.267	-	18.116
BSS 107	323.2354925	-0.8665373	19.456	-	-	18.725	-	18.680
BSS 108	323.3984464	-0.8676260	19.087	-	-	18.876	-	18.732
BSS 109	323.3183620	-0.7810710	-0.989	-	-	18.907	-	18.909
BSS 110	323.3559166	-0.8850258	19.140	-	-	18.981	-	18.848
BSS 111	323.3613786	-0.7077548	19.444	-	-	19.067	-	19.021
BSS 112	323.3404829	-0.7662234	19.151	-	-	19.077	-	18.947
BSS 113	323.4109976	-0.7642350	19.191	-	-	19.358	-	19.277
BSS 114	323.4193408	-0.8521266	19.270	-	-	18.599	-	18.440
BSS 115	323.4056858	-0.8112486	-	-	17.867	17.736	-	-
BSS 116	323.3255372	-0.8315272	-	-	17.927	17.785	-	-
BSS 117	323.4041892	-0.8414969	-	-	18.285	18.225	-	-
BSS 118	323.3961240	-0.8517851	-	-	18.508	18.205	-	-
BSS 119	323.3733585	-0.7932605	-	-	18.737	18.433	-	-
BSS 120	323.4136921	-0.8414584	-	-	18.826	18.591	-	-
BSS 121	323.4048915	-0.8170858	-	-	19.275	18.966	-	-
BSS 122	323.4061515	-0.8066183	-	-	18.529	18.434	-	-
BSS 123	323.3773334	-0.7905988	-	-	19.183	19.105	-	-

r_i''	r_e''	$N_{\rm BSS}$	$N_{\rm HB}$	$N_{\rm RGB}$	$L^{\rm samp}/L^{\rm samp}_{\rm tot}$
0	20	54	171	454	0.20
20	50	27	260	636	0.30
50	100	20	242	513	0.25
100	200	10	141	348 (2)	0.18
200	300	7	40	94 (3)	0.05
300	650	4 (1)	21	59 (12)	0.02

Table 4.2: The values listed out of the parenthesis correspond to the number of stars assumed to belong to the cluster (and thus used in the analysis), while those in the parenthesis are estimated to be contaminating field stars (see Sect. 4.4.1).

Chapter 5

Another Non-segregated Blue Straggler Population in a Globular Cluster: the Case of NGC 2419

Based on the results published in:

Dalessandro, E.; Lanzoni, B.; Ferraro, F. R.; Vespe, F.; Bellazzini, M.; Rood, R. T.

2008ApJ, 681, 311D

Abstract

We have used a combination of ACS-HST high-resolution and wide-field SUBARU data in order to study the Blue Straggler Star (BSS) population over the entire extension of the remote Galactic globular cluster NGC 2419. The BSS population presented here is among the largest ever observed in any stellar system, with more than 230 BSS in the brightest portion of the sequence. The radial distribution of the selected BSS is essentially the same as that of the other cluster stars. In this sense the BSS radial distribution is like that of ω Centauri and unlike that of all Galactic globular clusters studied to date which have highly centrally segregated distributions and in most cases a pronounced upturn in the external regions. As in the case of ω Centauri, this evidence indicates that NGC 2419 is not yet relaxed even in the central regions. This observational fact is in agreement with estimated half-mass relaxation time, which is of the order of the cluster age.

5.1 Introduction

In many GCs the projected radial distribution of BSS has been found to be bimodal: highly peaked in the center, with a clear-cut dip at intermediate radii, and with an upturn in their external regions. Such a behaviour has been confirmed in at least 7 GCs: M3, 47 Tuc, NGC 6752, M5, and M55,

NGC 6388 (see next Chapter) and M53 (Beccari et al. 2008). Dynamical simulations (Mapelli et al. 2006; Lanzoni et al. 2007a,b) suggest that the observed central peak is mainly due to COL-BSS formed in the core and/or MT-BSS sunk into the center because of dynamical friction, while the external rising branch is made of MT-BSS evolving in isolation in the cluster outskirts. In these bimodal clusters the BSS always appear to be significantly more segregated in the central regions than the reference cluster stars. The only exception to these general observational features is ω Centauri (hereafter ω Cen). The large population of BSS discovered by Ferraro et al. (2006b; hereafter F06) in this giant stellar system has the same radial distribution of the normal cluster stars. This is clear evidence that ω Cen is not fully relaxed, even in the central regions, and therefore, the dynamical evolution of the cluster has not significantly altered the radial distribution of these stars. It is likely that the vast majority of BSS observed in this cluster are the progeny of primordial binaries evolved in isolation (see also Mapelli et al. 2006).

Here we direct our attention to another massive cluster which shares a number of properties with ω Cen: NGC 2419. This remote object ($d \sim 81$ kpc, Harris et al. 1997) is one of the most luminous clusters in the Galaxy ($M_V = -9.4$; see Bellazzini 2007, hereafter B07) similar to ω Cen and M54 (NGC 6715). It has been suggested that both of the latter clusters are the remnants of stripped cores of dwarf spheroidals (see, e.g., Layden & Sarajedini 2000; Bekki & Freeman 2003). With its high luminosity and half-light radius ($r_h \simeq 25$ pc; B07), NGC 2419 lies (together with ω Cen and M54) in the $(r_h,\ M_V)$ plane well above the locus defined by all the other Galactic GCs. Indeed, it is the most significant outlier, thus suggesting that it also might be the stripped core of a former dwarf galaxy (van den Bergh & Mackey 2004; Mackey & van den Bergh 2005). Further, Newberg et al. (2003) suggested that NGC 2419 could be somehow connected with the Sagittarius (Sgr) dwarf spheroidal, since it seems to be located in a region with an overdensity of type-A stars which is in the same plane as the tidal tails of Sgr. However, the high-quality Color-Magnitude Diagrams (CMDs) of NGC 2419 recently published by Ripepi et al. (2007, hereafter R07; see also B07) do not show any evidence of multiple stellar populations, in contrast to ω Cen (Lee et al. 1999, Pancino et al. 2000, Bedin et al. 2004, Rey et al. 2004, Sollima et al. 2005) and possibly M54 (Layden & Sarajedini 2000; see also Monaco et al. 2005). It is however possible that for such a metal-poor cluster ($[Fe/H] = -1.97$; Ferraro et al. 1999b), the range in metallicities for the sub-population components is so small that different sequences cannot be seen in the CMD (Mackey & van den Bergh 2005; Federici et al. 2007).

In order to further investigate the dynamical status and the stellar populations of this remote

cluster, here we present a multi-wavelength study of BSS in NGC 2419. By combining HST high-resolution data, with wide-field SUBARU images, we sampled the total radial extension of the cluster. This allowed us to study and compare the projected radial distributions of BSS and other cluster stars in different evolutionary stages. The data and photometric reductions are described in Section 5.2. A general overview of the CMD is discussed in Section 5.3. The BSS population is described in Section 5.4, and the Discussion is presented in Section 5.6.

5.2 Observations and data analysis

5.2.1 The data sets

To study the crowded cores of high-density systems and simultaneously cover the total cluster extensions, we must use a combination of high resolution observations of the central regions and complementary wide-field images.

1. High resolution set – This is composed of a series of public images obtained with the Wide Field Channel of the Advanced Camera for Surveys (ACS) on board the Hubble Space Telecope (HST): two F435W ($\sim B$ filter) images with $t_{\rm exp} = 800$ sec each, two F555W ($\sim V$ filter) images with $t_{\rm exp} = 720$ sec, and two F814W ($\sim I$ filter) images with $t_{\rm exp} = 676$ sec (Prop GO9666, P.I. Gilliland). These are the highest resolution ($\sim 0.05'' \, {\rm pixel}^{-1}$) observations available to date for NGC 2419. Unfortunately the ACS images are off-centered (see Figure 5.1), and they do not completely sample the most central region of the cluster. As in previous works (see, e.g., Dalessandro et al. 2008a), average ACS images were obtained in each filter, and they were corrected for geometric distortion and effective flux (Sirianni et al. 2005). The data reduction has been performed using the ROMAFOT package (Buonanno et al. 1983), specifically developed to perform accurate photometry in crowded regions (Buonanno & Iannicola 1989).

2. Wide field set – We have used a set of public V and I images obtained with the SUBARU Prime Focus Camera (Suprime-Cam) of the 8.2 m SUBARU telescope at the Hawaii National Astronomical Observatory of Japan. The Suprime-Cam is a mosaic of ten 2048×4096 CCDs, which covers a $34' \times 27'$ field of view (FoV) with a pixel scale of $0.2''$. A combination of long-exposures ($t_{\rm exp} = 180$ sec) and median exposure ($t_{\rm exp} = 30$ sec) images has been retrieved from the Subaru Archive Web site (SMOKA). As shown in Figure 5.2, the cluster is centered in the chip #2 and it is totally included in the five adjacent chips; therefore only these six chips have been considered in the present study. We have applied standard pre-reduction procedures (correction

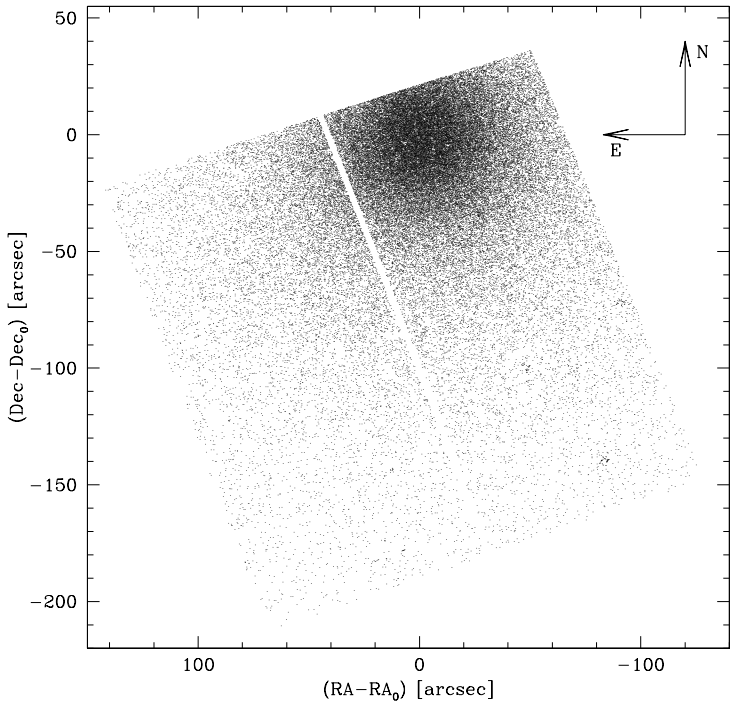

Figure 5.1: Map of the *HST sample*.

for bias, flat-field and overscan) using IRAF[1] tools. The reduction was performed independently for each image using the PSF fitting software DoPhot (Schechter et al. 1993).

5.2.2 Astrometry, center of gravity and photometric calibration

The ACS and SUBARU data have been placed on the absolute astrometric system by using the stars in common between each single chip and the SDSS data set used by B07, that, in turn, was astrometrized on the GSC-II astrometric reference star catalog. Hundreds of stars have been matched in each chip, thus allowing a very precise determination of the stellar absolute positions in our catalogs. The resulting rms residuals (a measure of the internal astrometric accuracy) were of the order of $\sim 0''.3$ both in Right Ascension (α) and Declination (δ).

The photometric calibration of the ACS catalog has been performed in the VEGAMAG system using the relations and zero-points described in Sirianni et al. (2005). Then, the SUBARU catalog has been homogenized to the ACS one. In order to transfer the instrumental Subaru magnitudes

[1]IRAF is distributed by the National Optical Astronomy Observatory, which is operated by the Association of Universities for Research in Astronomy, Inc., under cooperative agreement with the national Science Foundation

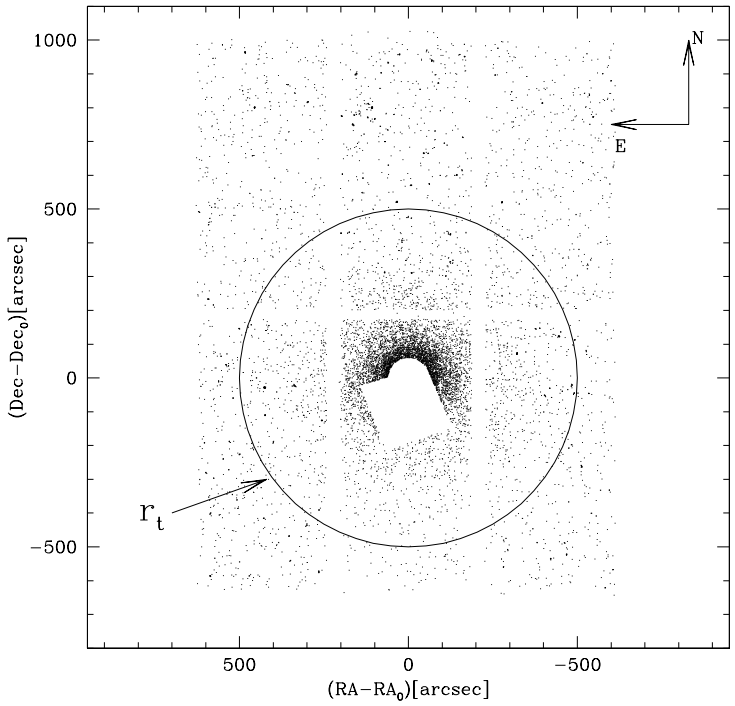

Figure 5.2: Map of the *SUBARU sample*. The circle with radius $r_t = 500''$ (adopted as tidal radius) centered in the cluster center is shown as a solid line.

into the ACS VEGAMAG system, a subsample of a few hundred stars in common between the Subaru and the ACS FOVs has been selected, and the following relations have been obtained:

$$I_{\rm ACS} - i_{\rm Subaru} = 0.55(V-I)_{\rm ACS} + 27.41 \tag{5.1}$$

$$V_{\rm ACS} - v_{\rm Subaru} = -0.20(V-I)_{\rm ACS} + 27.46 \tag{5.2}$$

where $i_{\rm Subaru}$ and $v_{\rm Subaru}$ are the instrumental I and V magnitudes in the Subaru sample referred to 1s exposure. In this way a final list of absolute positions and homogeneous (VEGAMAG) magnitudes for all the stars in the two catalogs was obtained.

In order to determine the Center of Gravity ($C_{\rm grav}$) of the cluster, we have computed the barycenter of all the stars found in the ACS catalog at a distance $r < 10''$ from the center quoted by Harris (1996). A circular region of $10''$ radius is the maximum available area completely covered by the ACS observations (see Fig. 5.1). The absolute positions (α, δ) of the stars have been averaged using iterative technique described in previous works (e.g., Montegriffo et al. 1995;

Ferraro et al. 2003). We have excluded stars brighter than $V = 19.5$ since they are saturated in the ACS images. The same procedure has been repeated for three different magnitude cuts ($V < 24$, $V < 23.5$, and $V < 23$) in order to check for any possible statistical or spurious fluctuations. The three measures agree within $\sim 1''$ and their mean value has been adopted as best estimate of $C_{\rm grav}$: $\alpha = 7^{\rm h}\,38^{\rm m}\,8\overset{s}{.}47^{s}$ and $\delta = 38^{\circ}\,52'\,55\overset{''}{.}0$, with an uncertainty of $0\overset{''}{.}5$ in both α and δ. This new determination is in agreement with that listed by Harris (1996).

Given the coordinates of $C_{\rm grav}$, we have divided the dataset in two main samples: the *HST sample*, which includes all the stars found in the ACS catalog, and the *SUBARU sample*, that consists of stars not included in the ACS FoV and lying at $r > 60''$ from the cluster center. The latter choice implies that a small region (a segment of a circle located $\sim 20''$ North from the cluster center) is covered neither by the HST nor by the SUBARU sample (see Fig.5.2). This conservative choice is made to avoid incompleteness effects of the ground based observations in the most crowded central regions of the cluster.[2]

5.3 CMD overall characteristics and the HB morphology

The CMD of stars in the HST sample is shown in Figure 5.3. All the main cluster evolutionary sequences are clearly defined and well populated. This is the deepest CMD ever published for NGC 2419, reaching down to $B \sim 27$. The stars in the brightest ($B < 19.5$) portion of the red giant branch (RGB) are not shown in the figure, because they are heavily saturated in these exposures. Particularly notable is the horizontal branch (HB) morphology, which looks quite complex, with a long HB blue tail (BT) extending well below the cluster MS-TO. The peak of the HB population is located at $B \sim 20.7$ and $(B - I) \sim 0.2$. The HB population significantly decreases with decreasing luminosity along the BT. A poorly populated region (a gap?) is visible at $B \sim 23.4$, separating the extreme extention of the BT and a clump of stars extending down to $B \sim 25$. Following the nomenclature adopted in Dalessandro et al. (2008a), these are extreme HB (EHB) with the faintest probably being Blue Hook (BHk) stars. Definitive assignment to these groups will require UV photometry.

In Figure 5.4 we show a direct comparison between the HB of NGC 2419, and that of ω Cen (from Ferraro et al. 2004), suitably shifted (by ~ 5.6 magnitudes) in order to match the HB level of NGC 2419. The two HBs show very similar extension and morphology. The only significant difference is that EHB/BHk stars in NGC 2419 are much more spread-out in color $\delta(B - I) \sim 1$

[2]However, note that the annular region between $20''$ and $60''$ from the cluster center is well sampled (at $\sim 70\%$) by the ACS sample.

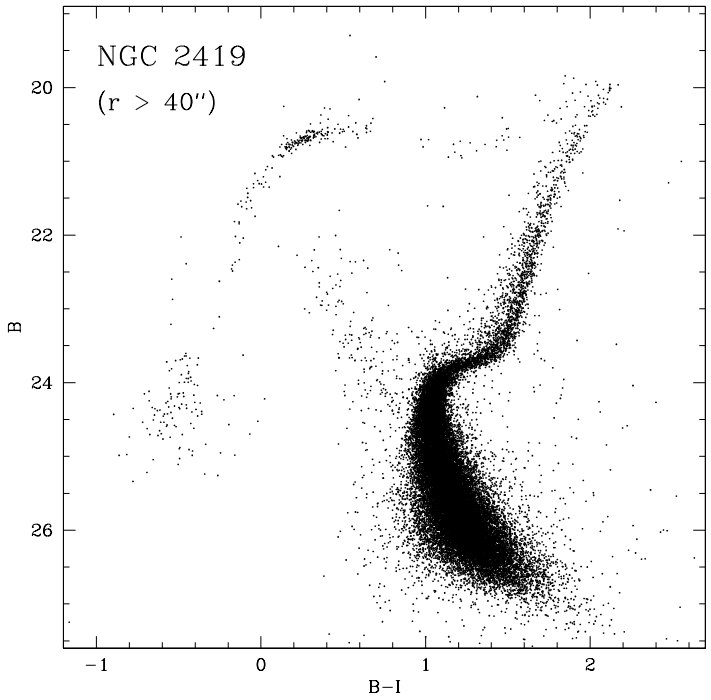

Figure 5.3: $(B,\, B-I)$ CMD of the *HST sample* for $r > 40''$ from the center, reaching down $B \sim 27$.

than to the same population in ω Cen. The rms scatter between the magnitude measurements in the two single images, both in the B and I bands is $\sigma_B \sim 0.1$ and $\sigma_I \sim 0.24$ mag) thus the photometric error in $B-I$ is $\sigma_{B-I} \sim 0.26$ mag at the level of BHk stars. The observed color spred is about 4σ and may thus be real.

Whether the color distribution is different from that of ω Cen is an open question. To demonstrate more clearly the striking similarity of these HBs, in Figure 5.5 we show the normalized magnitude distribution of HB stars as a function of the B magnitude in the two clusters. The percentage of stars in three portions of the branch is also designated in the figure. Beyond general appearance the HBs are quantitatively similar: *(i)* both the HBs extend for almost 4.5 mag; *(ii)* both the distributions show a well defined peak, an extended tail and a EHB/BHk clump; *(iii)* the bulk of the HB population ($\sim 58\%$) is localized in the brightest 1 magnitude portion of the branch; *(iv)* the BT is 10–12% of the population; *(v)* both the EHB/BHk clumps extend for roughly 1.5 magnitudes and they comprise $\sim 30\%$ of the total HB population.

As discussed in Dalessandro et al. (2008a), the nature of BHk stars is still unclear: they

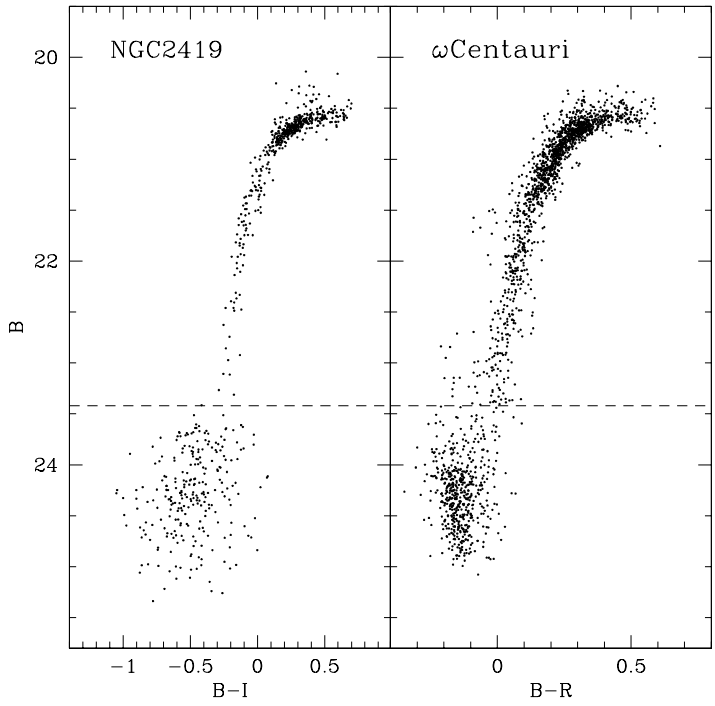

Figure 5.4: Comparison of the HB morphology of NGC 2419 and ω Cen (from F06). Only stars in the ACS FoV are plotted. The HB of ω Cen has been shifted by $\delta B = 5.6$ to match that of NGC 2419. The dashed line marks the brightest boundary of the BHk population.

may be related to the so-called late hot flashers (Moehler et al. 2004, Catelan 2007), or due to high helium abundances (as suggested by Busso et al. 2007, in the case of NGC 6388; see also Caloi & D'Antona 2007; D'Antona et al. 2005), or related to the evolution of binary systems (Heber et al. 2002). However, the detection of a population of BHk stars in a low-metallicity cluster as NGC 2419 clearly demonstrates that the process producing these extremely hot HB stars can efficiently work in any metallicity environment: NGC 6388 ($[Fe/H] \sim -0.4$), NGC 2808 ($[Fe/H] \sim -1.1$), ω Cen ($[Fe/H] \sim -1.6$), M54 ($[Fe/H] \sim -1.8$) and NGC 2419 ($[Fe/H] \sim -2$). NGC 2419 is very massive as are the other BHk clusters. We have also checked the EHB/BHk radial distributions with respect to the brightest portion of the HB and the RGB. The significance of the difference has been quantified with a Kolmogorov-Smirnov (KS) test: the radial distribution of the BHk population is consistent with that of normal cluster stars, in agreement with similar findings in NGC 6388 (Rich et al. 1997, Dalessandro et al. 2008a), ω Cen (Ferraro et al. 2004). However, the evidence presented in Sect. 5.5 demonstrates that NGC 2419 is not relaxed

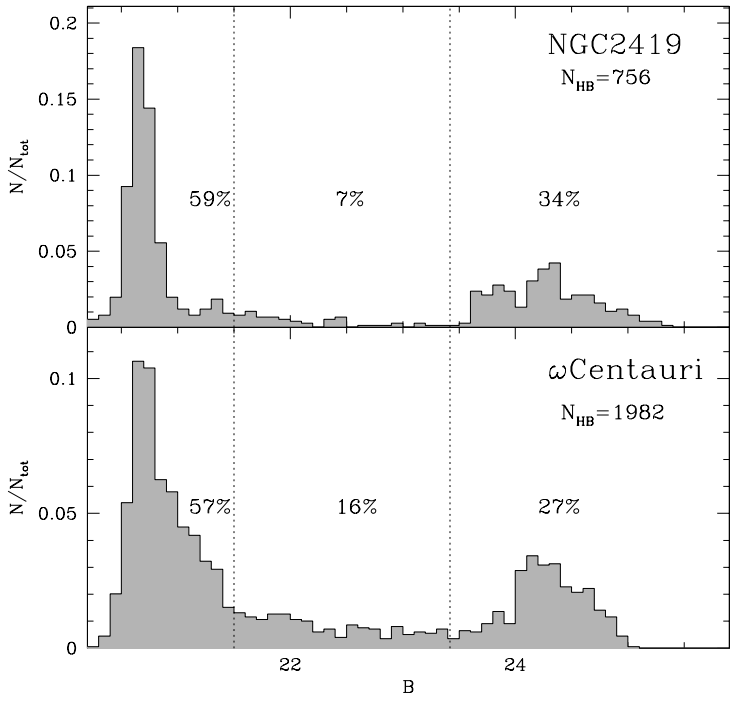

Figure 5.5: Normalized magnitude distributions of the HB stars of NGC 2419 (upper panel) and ω Cen (bottom panel, from F06) plotted in Fig. 5.4. The vertical dotted lines mark three (arbitrary) portions of the HB separting the bulk of the population, the BT HB and the BHk.

even in the central regions, hence no segregation is expected for these stars even in the case they were binaries. However, as discussed in Dalessandro et al. (2008a), it is important to remember that the lack of segregation of the EHB/BHk population is not firm proof of the non-binarity of EHB/BHk stars, since they could be low-mass binaries, with a total mass similar (or even lower) than "normal" cluster stars (for example, a 0.5 $M_{\odot}$ He-burning star with a 0.2 $M_{\odot}$ He white dwarf companion).

5.3.1 Density profile and distance modulus estimate

The $(V,\ V-I)$ CMDs of the HST and SUBARU samples defined in Section 5.2.2 are shown in Figure 5.6. Thanks to the high-resolution ACS images of the cluster core and the wide FoV of the SUBARU observations, we have properly sampled the stellar population over the entire cluster extension. We have then used this data-set to determine the projected density profile of NGC 2419 using direct star counts, from $C_{\rm grav}$ out to about $1000''$.

Stars with $V > 19.5$ are saturated in the ACS sample and therefore have been excluded from

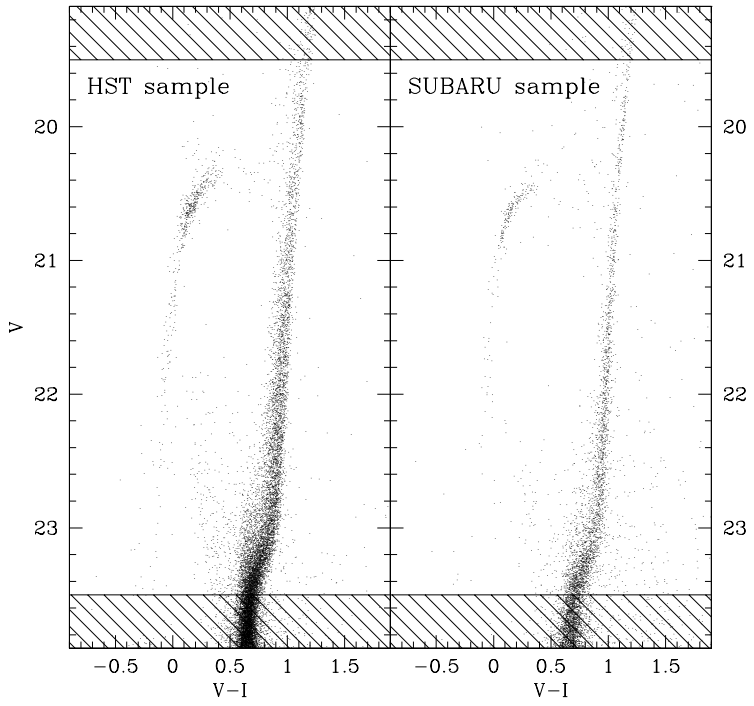

Figure 5.6: CMDs used to derive the surface density profile of NGC 2419. The hatched regions indicate stars that have been excluded because they are saturated in the *HST sample* (those with $V < 19.5$) , or in order to avoid incompleteness effects (stars fainter than $V = 23.5$).

the analysis; however, since they are small in number, this produces a negligible effect on the global result. In order to avoid incompleteness biases we have also excluded stars fainter than $V = 23.5$. Using the same procedure described in Ferraro et al. (1999a) the whole sample has been divided in 24 concentric annuli, each centered on $C_{\rm grav}$ and suitably split in a number of subsectors. The number counts have been calculated in each subsector and the corresponding densities were obtained dividing them by the sampled area (taking into account the incomplete spatial coverage of the region between $20''$ and $60''$). The stellar density of each annulus has then be defined as the average of the subsector densities and its standard deviation is computed from the variance among the subsectors. The resulting projected surface density profile is plotted in Figure 5.7. As apparent, the outermost two points show a flattening of the stellar number density, and their average (corresponding to ~ 4 stars/arcmin^2) has therefore been used as an estimate of the background contribution. The derived radial density profile is well fit by an isotropic single-mass King model, with concentration $c = 1.36$ and core radius $r_c = 20''$ (solid line in Fig. 5.7),

yielding a "formal" value of the cluster tidal radius of $r_t \sim 460''$ and a half-mass radius of $r_h \sim 58''$. These parameters are essentially equal to those obtained by B07 and in good agreement with other previous determinations (see, e.g., Table 2 in B07).

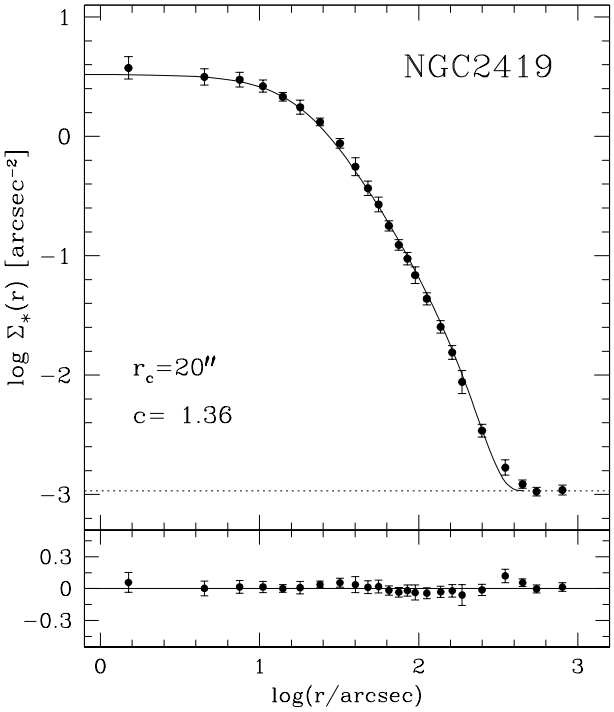

Figure 5.7: Observed surface density profile (*dots and error bars*) and best-fit King model (*solid line*). The radial profile is in units of number of stars per square arcseconds. The *dotted line* indicates the adopted level of the background (corresponding to ~ 4 stars/arcmin^2), and the model characteristic parameters (core radius r_c and concentration c) are marked in the figure. The lower panel shows the residuals between the observations and the fitted profile at each radial coordinate.

We have used the available high-quality data set also for deriving an independent estimate of the distance to NGC 2419. To do this, we compared the CMD shown in Fig. 5.3, to that of M92 (NGC 6341), one of the "prototype" Galactic GCs, with similar metallicity ([Fe/H]$= -1.97$ and -2.16 for NGC 2419 and M92, respectively; Ferraro et al. 1999b). We have used a combination of WFPC2 and ACS data of M92, obtained through filters F555W ($\sim V$) and F814W ($\sim I$). We have shifted the CMD of M92 onto that of NGC 2419 until a good match between the main evolutionary sequences (RGB, HB, sub-giant branch and TO region) of the two clusters was reached (see Figure 5.8). This has required a color shift $\delta(V-I) = 0.14$ and $\delta V = 5.25$, similar to that obtained by Harris et al. (1997) from an analogous comparison based on independent data sets.

Figure 5.8 shows that a really nice matching of all the evolutionary sequences of the two clusters can be achieved. This evidence also suggests that the two clusters have a similar age (in agreement with Harris et al 1997, who estimated an age difference of ~ 1 Gyr for the two objects).

By assuming the distance modulus $(m-M)_0 = 14.78$ and the reddening $E(B-V) = 0.02$ for M92 (Ferraro et al. 1999b), and by using the standard absorption coefficient ($A_V = 3.1$ and $A_I = 1.7$), we have obtained $E(B-V) = 0.12 \pm 0.03$ and $(m-M)_V = 20.09$, corresponding to a true distance modulus $(m-M)_0 = 19.72$, for NGC 2419. The reddening obtained from this procedure is in good agreement with the value derived by Harris et al. (1997), who quoted $E(B-V) = 0.11$, and it is also agreement with the value $E(B-V) = 0.08$ adopted by R07 within the errors. Taking a conservative estimate of $\sigma \sim 0.1$ mag, we finally adopt $(m-M)_0 = 19.7 \pm 0.1$.

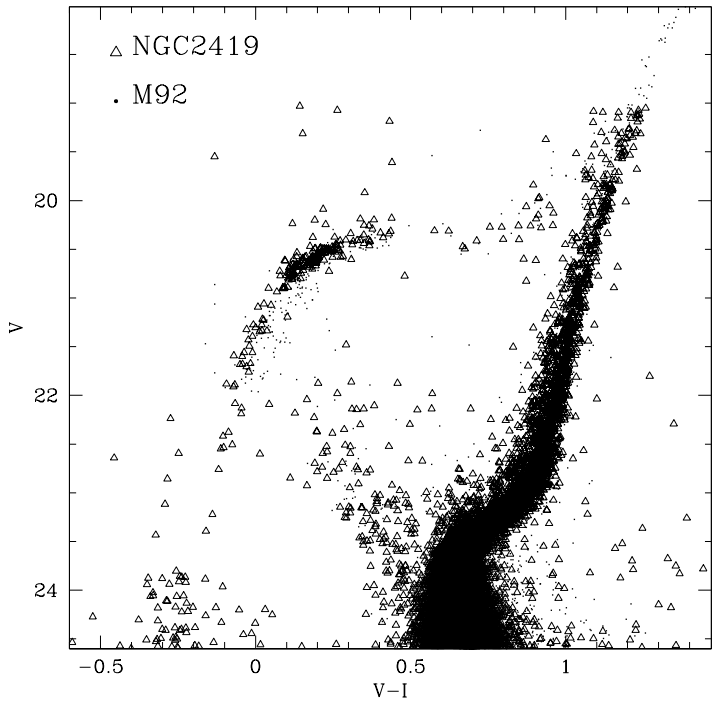

Figure 5.8: $(V, V-I)$ CMD of M92 (*dots*) superimposed onto that of NGC 2419 (*triangles*) after a magnitude shift of $\delta V = 5.25$ and a color shift of $\delta(V-I) = 0.14$.

This yields a real distance $d \simeq 87 \pm 4$ kpc. Within the uncertainties, this estimate is in agreement with both that found by Harris et al. (1997; $d = 81 \pm 2$ kpc) and that obtained by R07 using the mean luminosity of the RR Lyrae stars ($d = 83.2 \pm 1.9$ kpc). Assuming this

distance, the physical dimension of the core radius and of the half-mass radius of the cluster can be obtained: given $r_c = 20''$ and $r_h = 58''$ (see above), we obtain $r_c = 8.4$ pc and $r_h = 24.5$ pc, respectively. By adopting the total integrated magnitude $V_t = 10.47$ quoted by B07, the absolute cluster magnitude is $M_V = -9.6$. This value, combined with the size of the half-mass radius, confirms the anomalous position of NGC 2419 in the r_h versus M_V plane (van den Bergh & Mackey 2004).

5.4 The population of BSS

5.4.1 Population selection

To select the BSS population we have chosen to use the $(B,\ B-I)$ CMD, in which the BSS sequence is better defined. To avoid spurious effects due to sub-giant branch star blends and Galaxy field star contamination, only stars brighter than $B \simeq 23.6$ (corresponding to ~ 1 mag above the TO) and with $B - I < 0.75$ have been selected (see Figure 5.9). The resulting number of BSS in the *HST sample* is 183. The position of the bulk of these stars in the ACS $(V,\ V-I)$ CMD has then been used to define the BSS selection box for the *SUBARU sample*. This is shown in Figure 5.10, with the faint and red edges corresponding to $V \simeq 23.3$ and $V - I < 0.48$, respectively. The resulting number of BSS found in the entire SUBARU sample is 67, out of which 49 are found within the "safe" distance of $\sim 500''$ from the cluster center. This distance is slightly larger than the "formal" tidal radius obtained in Sect. 5.3.1 and takes into account possible uncertainties in the determination of the latter. The positions and magnitudes of the all the 232 BSS thus selected are listed in Table 5.1.[3]

Reference populations representative of the "normal" cluster stars and needed to properly study the BSS radial distribution. We considered both the HB and the RGB. Since the HST and the SUBARU samples have the V and I filters in common, we performed a homogeneous selection of these populations in the $(V,\ V-I)$ plane. The HB selection box (see Fig. 5.10) has been drawn to limit the contribution of field contamination in the bright-red portion of the sequence (i.e., we have required that $V - I < 0.65$ at $V \sim 20$) and in order to exclude the EHB/BHk clump ($V \lesssim 23.6$). The EHB/BHk stars populate a region located ~ 1 magnitude below the MS-TO (see Fig. 5.8), which is very close to the detection limit of the V and I observations. Thus, they could be severely affected by incompleteness bias, and we have therefore preferred not to include

[3] Several SX Phoenicis variables have been found by R07. However a direct comparison between these stars and our BSS sample is not possible, since the R07 catalog is not yet published.

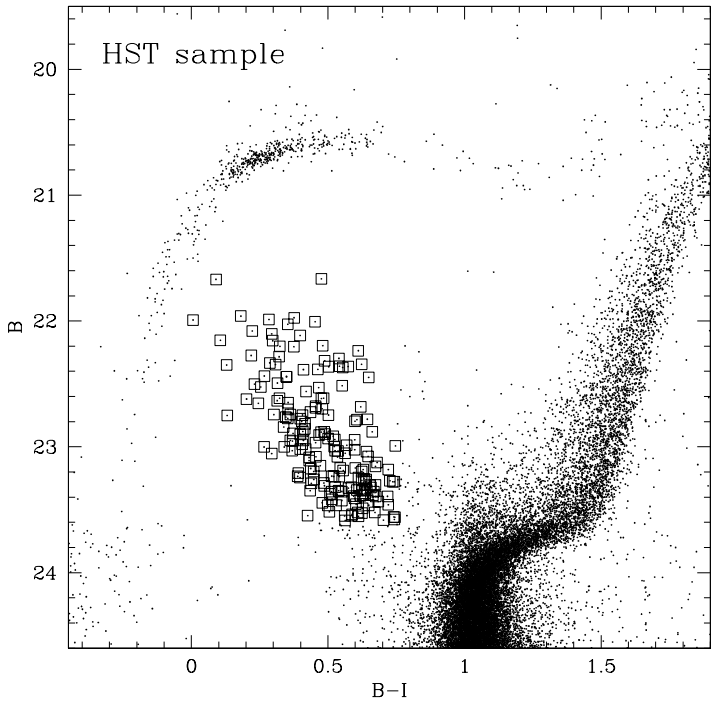

Figure 5.9: BSS population (squares) selected in the $(B,\ B-I)$ CMD of the *HST sample*.

them in the HB reference population. However, since their radial distribution is indistinguishable from that of the other HB stars, this exclusion has negligible effect on the following results. The total number of HB stars thus selected within $500''$ is 765, with 528 found in the HST sample and 237 in the SUBARU one. The RGB population has been selected along the RGB mean ridge line between $V \simeq 19.9$ and $V \simeq 22.5$ (see the selection box in Fig. 5.10). This choice has been dictated by the fact that the brightest portion of the RGB sequence is saturated in the HST sample, and its faintest portion is contaminated by Galactic field stars, especially in the SUBARU sample. The total number of these stars within $500''$ is 3250, with 2337 found in the HST sample and 913 in the SUBARU one.

5.5 BSS radial distribution

A first qualitative comparison between the cumulative radial distribution of BSS and that of the reference populations (see Figure 5.11) has been performed using the KS test. This gives 70% and 50% probabilities that the BSS population is extracted from the same population as the HB and RGB stars, respectively. Hence there is preliminary evidence that the radial distribution of BSS is

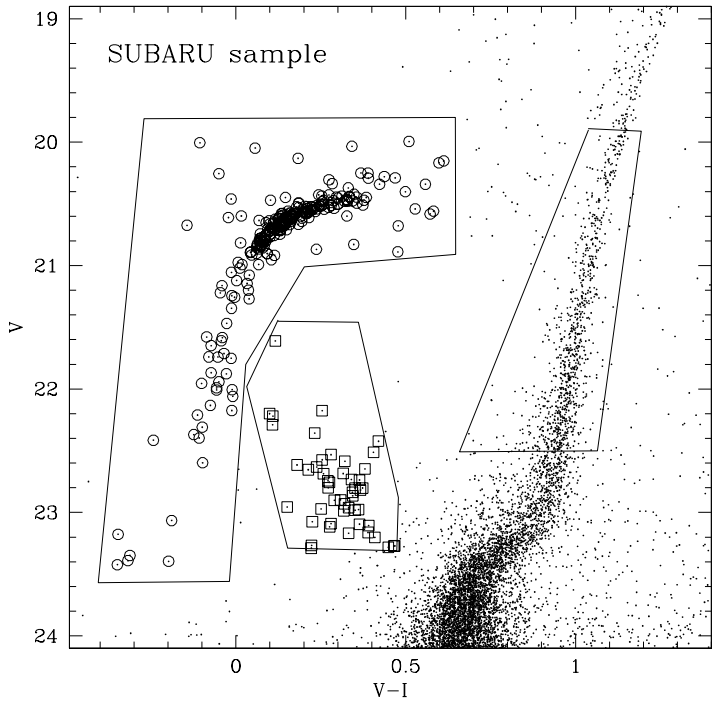

Figure 5.10: $(V,\, V-I)$ CMD of the SUBARU sample for $r < 500''$ from the center, with the adopted BSS, HB and RGB selection boxes highlighted. The selected BSS and HB populations are also marked with open squares and circles, respectively.

indistinguishable from that of the "normal" cluster population, in contrast to what found in most of the typical GCs (see references in Dalessandro et al. 2008a).

For a more detailed analysis, we have used the same technique described in previous works (see, e.g., F06). The sampled area within $r = 500''$ has been divided in 5 concentric annuli centered on $C_{\rm grav}$. In each of these we have counted the number of BSS, HB and RGB stars. However, the examination of the external regions ($r > 500''$) of the SUBARU sample CMD suggests that the selected (BSS, HB, and RGB) populations can be affected by contamination from stars in the Galactic field. In order to account for this effect we adopted the statistical correction as used in previous papers (see, e.g., Dalessandro et al. 2008a). To do this we selected a rectangular region of $\sim 70\,{\rm arcmin}^2$ located at $r > 650''$, i.e. well beyond the formal tidal radius of the cluster. The CMD of this region clearly shows that the Galaxy field population is dominant relative to the cluster one. Then we counted the number of stars in this region lying in the BSS, HB and RGB selection boxes showed in Fig. 5.6 and derived the following values of the field star densities:

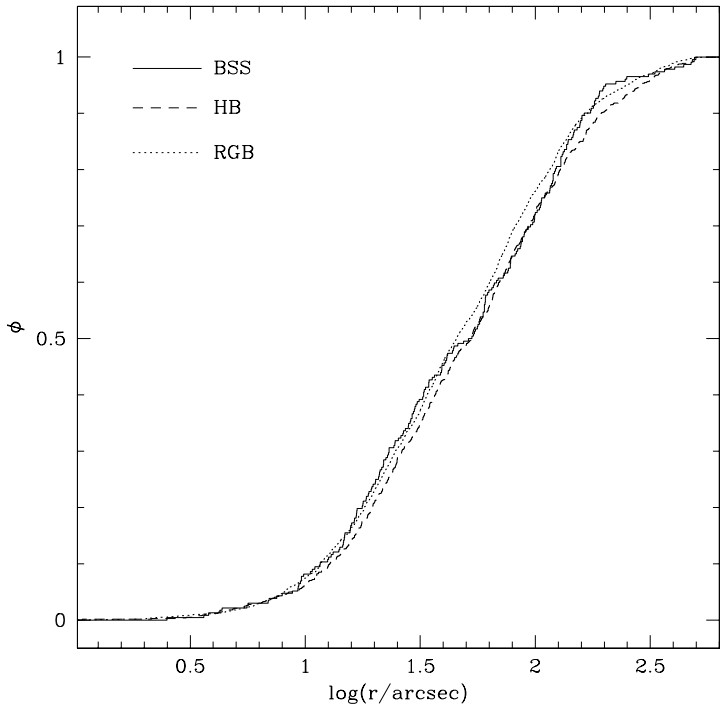

Figure 5.11: Cumulative radial distribution of BSS (solid line), HB (dashed line) and RGB stars (dotted line) as a function of the projected distance from the cluster center, for the combined HST+SUBARU sample at $r < 500''$. The populations show essentially the same radial distribution.

$D_{\rm BSS}^{\rm field} = 0.03\,{\rm stars\,arcmin}^{-2}$, $D_{\rm HB}^{\rm field} = 0.06\,{\rm stars\,arcmin}^{-2}$ and $D_{\rm RGB}^{\rm field} = 0.14\,{\rm stars\,arcmin}^{-2}$. These quantities allow us to estimate the impact of the field contamination on the selected samples: 6 BSS ($\sim 2\%$), 12 HB ($\sim 1.5\%$) and 31 RGB($\sim 1\%$), essentially all in the most external annulus, could be field stars (see Table 5.2). Though the effect of the field contamination is small, in the following we use the statistically decontaminated samples in order to determine the population ratios and the radial distribution.

By using the King model, the distance modulus and the reddening estimated in Sect. 5.3.1, the luminosity sampled in each annulus ($L^{\rm samp}$) has also been estimated. Then for each annulus we have computed the double normalized ratio defined in Ferraro et al. (1993):

$$R_{\rm pop} = \frac{N_{\rm pop}/N_{\rm pop}^{\rm tot}}{L^{\rm samp}/L_{\rm tot}^{\rm samp}}, \tag{5.3}$$

with pop= BSS, HB and RGB. We find that $R_{\rm HB}$ and $R_{\rm RGB}$ are essentially constant and close to unity (see $R_{\rm HB}$ in Figure 5.12). This is what expected for any post-MS population according

to the stellar evolution theory (Renzini & Fusi Pecci 1988). Surprisingly we also find that the double normalized ratio of BSS is constant, and it is fully consistent with the reference populations (Fig. 5.12).

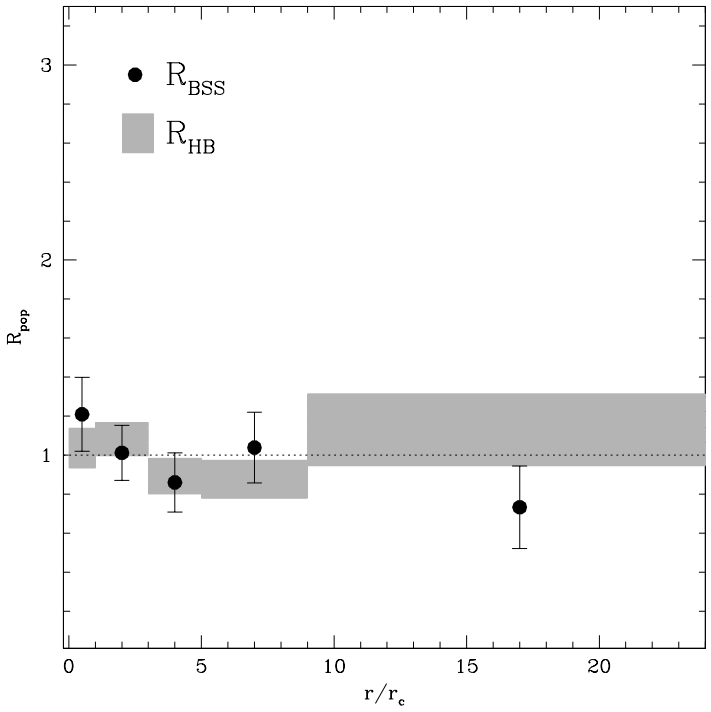

Figure 5.12: Double normalized ratios, as defined in eq. (5.3), of BSS (dots) and HB stars (grey rectangular regions), plotted as a function of the radial coordinate expressed in units of the core radius. The size of the grey rectangles corresponds to the error bars. The two distributions are almost constant around unity over the entire cluster extension, as expected for any normal, non-segregated cluster population.

Using the number counts listed in Table 5.2, we have also computed the specific frequencies N_{BSS}/N_{HB}, n_{BSS}/n_{RGB} and N_{HB}/N_{RGB}. We find that all these ratios are almost constant all over the entire extension of the cluster (see Figure 5.13), confirming again that no signatures of mass segregation are visible for the BSS population of NGC 2419.[4]

[4]Note that this result is independent of which portion of the RGB is selected. Similar results are obtained also by considering the RGB in the same magnitude range of the BSS.

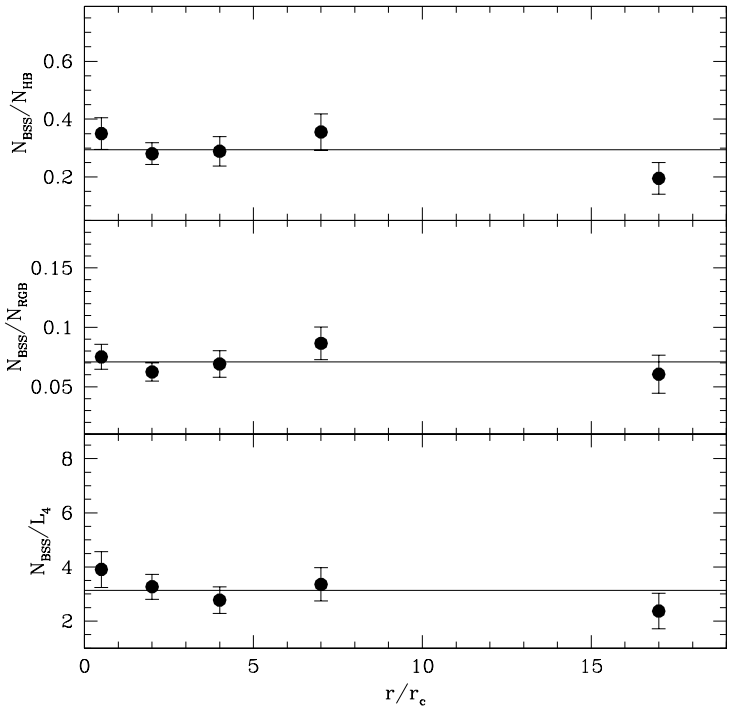

Figure 5.13: Specific frequency of BSS with respect to HB stars (upper panel), RGB stars (middle panel), and the sampled luminosity in units of $10^4 L_\odot$ (bottom panel) as a function of the projected distance from the cluster center in units of r_c.

5.6 Discussion

In most previously surveyed Galactic GCs (M3; 47 Tuc, NGC 6752,M5, M55, NGC 6388, M53) the BSS radial distribution has been found to be bimodal (highly peaked in the core, decreasing to a minimun at intermediate radii, and rising again in the external regions). The mechanisms leading to bimodal radial distributions have been studied for some clusters using dynamical simulations (see Mapelli et al. 2004, 2006; Lanzoni et al. 2007a,b). The observed central peak is mainly made up of collisionally formed BSS and/or MT-BSS sunk into the core because of dynamical friction. The external rising branch is composed of MT-BSS evolving in isolation in the cluster outskirts. In contrast, the BSS radial distribution of NGC 2419 is essentially the same as that of the other "normal" stars in the cluster. Previously, ω Cen was the only GC known to have a flat BSS radial distribution. F06 (see also Meylan & Heggie 1997) argued that two-body relaxation had not led to the complete relaxation of ω Cen even in the central core. Our result here suggests that the same situation holds for NGC 2419.

We can compare this observational evidence with theoretical time-scales expected on the basis of the cluster structural parameters. Following equation (10) of Djorgovski (1993), we computed the cluster central relaxation time (t_{r_c}) by adopting $m = 0.3\,M_{\odot}$ for the average stellar mass, and $M/L = 3$ for the mass-to-light ratio and $M_{V\odot} = 4.79$ for the V band solar magnitude. The integrated magnitude obtained in Sect. 5.3.1 then leads to a total cluster mass of $1.7 \times 10^6 M_{\odot}$, and a total number of stars of 5.7×10^6. By assuming $\rho_0 \simeq 25\,M_{\odot}\,\mathrm{pc}^{-3}$ (Pryor & Meylan 1993), and given the value of the core radius ($r_c = 8.4$ pc) derived in Sect. 5.3.1, we obtain $t_{r_c} \sim 6$ Gyr, which is about half the cluster age ($t = 12$–13 Gyr; Harris et al. 1997). Thus some evidence of mass segregation should be visible at least in the core, at odds with the observed flat distribution of BSS. We can also compute the characteristic relaxation time-scale for stars as massive as BSS ($M_{\mathrm{BSS}} \sim 1.2 M_{\odot}$; see F06) at the cluster half-mass radius (t_{r_h}) using equation (10) of Davies et al. (2004). Since $r_h \sim 24.5$ pc (see Sect. 5.3.1) we obtain $t_{r_h} \sim 18$ Gyr, thus suggesting that no significant segregation is expected for stars as massive as the BSS in the outer parts of the clusters, in agreement with our observational results. This result is similar to that found for ω Cen by F06 where the relaxation time in the core was found to be $\sim$ half the cluster age. In the case of ω Cen a number of possible explanations were examined, for instance, the possibility that ω Cen is the relic of a partially disrupted galaxy, which was much more massive in the past. A similar argument can be advocated for NGC 2419, which has also been suspected to be the relic of a small dwarf galaxy interacting with the Milky Way (van den Bergh & Mackey 2004; Federici et al. 2007 and references therein). However, it should be noted that the above estimates of the relaxation times are rough, and since the predicted value of t_{r_c} is only a factor of 2 smaller than the cluster age, more detailed computations are needed before further interpret these results.

From the observational side, the BSS radial distribution shown in Figs. 5.12 and 5.13 suggests that in NGC 2419 (as in ω Cen) stellar collisions have played a minor (if any) role in modifying the radial distribution of massive objects and probably also in generating exotic binary systems. If dynamical evolution plays a central role in NGC 2419, the observed flat BSS distribution can be explained only by invoking an *ad hoc* formation/destruction rate balancing the BSS population in the core and in the outer region of the cluster. It is more likely that this flat distribution arises because the BSS we are observing result from the evolution of primordial binaries whose radial distribution has not been altered by the dynamical evolution of the cluster. Thus, as in the case of ω Cen, the BSS population observed in NGC 2419 could be a pure population of primordial binaries BSS (PB-BSS), and it can be used to evaluate the incidence of such a population in stellar

systems.

As in previous papers (see Ferraro et al. 1995, F06) here we compute the PB-BSS frequency as the number of BSS normalized to the sampled luminosity in units of $10^4\,L_{odot}$: $S4_{\rm PB-BSS} = N_{BSS}/L_4$ (see the bottom panel of Fig. 5.13). This quantity is useful for estimating the expected number of BSS generated by PBs for each fraction of the sampled light in any stellar system resolved or not[5]. For NGC 2419, we find $S4_{\rm PB-BSS} = 3.1 \pm 0.6$ (see Fig. 5.13). Before comparing this quantity to that found in ω Cen by F06, we must account for the fact that the adopted BSS selection criteria are different in the two clusters. In NGC 2419 we considered BSS brighter than $B < 23.6$; this threshold corresponds to $B < 18$ at the distance of ω Cen, using the value $\delta B = 5.6$ needed to shift the HB of ω Cen onto that of NGC 2419 (see Fig.5.4). By adopting this threshold, 104 BSS are found in the ACS FoV of ω Cen, and by considering the sampled luminosity, we obtain $S4_{\rm PB-BSS} = 1.6$ for this cluster.[6] This comparison suggests that the number of BSS per unit sampled light in NGC 2419 is twice as large than that in ω Cen.[7] Under the hypothesis that the vast majority of these BSS are generated by the evolution of PBs, the different $S4_{\rm PB-BSS}$ values could result from a different binary frequency in the two clusters, since PB-BSS are expected to strongly depend on the fraction of binaries in the cluster. Indeed the first direct correlation between these two quantities (the binary fraction and the BSS frequency) has been recently detected in a sample of 13 low-density clusters by Sollima et al. (2008). Such a connection strongly supports a scenario in which the evolution of PBs is the main formation channel for BSS in low-density environments.

The case of NGC 2419 further supports the idea that important signatures of the dynamical evolution of the parent cluster are imprinted in the radial distribution of the BSS population: indeed the most recent results collected by our group (see Ferraro et al. 2003, 2006; Lanzoni et al. 2007a,b,c; Dalessandro et al. 2008a) are building the ideal data-base from which such signatures can be read and interpreted, and are already confirming this hypothesis.

[5]This quantity is also important in evaluating the incidence of creation/destruction rate of BSS in the central region of high-density clusters, where collisions can have played a major role in producing collisional BSS.

[6]Of course, such a value is slightly smaller than that ($S4_{\rm PB-BSS} = 2$) obtained in F06 by considering the entire sample of BSS with $B < 18.4$

[7]A similar result is obtained if selecting the BSS population of NGC 2419 down to the same threshold used by F06 for the BSS in ω Cen, i.e. $B < 18.4$ (which corresponds to $B = 24$ at the distance of NGC 2419).

Table 5.1: The BSS population of NGC 2419.

Name	RA[degree]	Dec[degree]	B	V	I
BSS 1	114.5346238	38.8659223	21.67	21.48	21.19
BSS 2	114.5317934	38.8778178	21.97	21.84	21.60
BSS 3	114.5545324	38.8522824	22.01	21.86	21.55
BSS 4	114.5290061	38.8781085	21.96	21.87	21.78
BSS 5	114.5563785	38.8777071	22.03	21.88	21.67
BSS 6	114.5375980	38.8849180	21.99	21.88	21.70
BSS 7	114.5426076	38.8723283	22.20	21.98	21.72
BSS 8	114.5322465	38.8824554	22.08	21.98	21.86
BSS 9	114.5321660	38.8802393	22.10	21.99	21.81
BSS 10	114.5314467	38.8844550	22.11	21.99	21.72
BSS 11	114.5389799	38.8741541	22.20	22.04	21.83
BSS 12	114.5180869	38.8707066	22.20	22.04	21.88
BSS 13	114.5333262	38.8735631	22.24	22.09	21.62
BSS 14	114.5186506	38.8555156	22.15	22.09	22.05
BSS 15	114.5631273	38.8567423	22.34	22.10	21.72
BSS 16	114.5350018	38.8575038	22.36	22.14	21.79
BSS 17	114.5220854	38.8869184	22.32	22.14	21.83
BSS 18	114.5559528	38.8756214	22.36	22.14	21.82
BSS 19	114.5308496	38.8836661	22.36	22.15	21.86
BSS 20	114.5052076	38.8695694	22.27	22.18	22.06
BSS 21	114.5479750	38.8829417	22.39	22.23	21.98
BSS 22	114.5542824	38.8787225	22.35	22.23	22.04
BSS 23	114.5279917	38.8771869	22.33	22.23	22.05
BSS 24	114.5289397	38.8789566	22.35	22.25	22.22
BSS 25	114.5402618	38.8322954	22.45	22.30	21.80
BSS 26	114.5544769	38.8807888	22.51	22.30	21.96
BSS 27	114.5179647	38.8667478	22.53	22.35	22.06
BSS 28	114.5208423	38.8864626	22.44	22.37	22.17
BSS 29	114.5099740	38.8743802	22.49	22.38	22.18
BSS 30	114.5707475	38.8723047	22.56	22.39	22.14
BSS 31	114.5349532	38.8807603	22.62	22.43	22.14
BSS 32	114.5373408	38.8847449	22.68	22.43	22.06
BSS 33	114.5255999	38.8898043	22.69	22.46	22.23
BSS 34	114.5213599	38.8819734	22.63	22.49	22.32
BSS 35	114.5624518	38.8577883	22.68	22.51	22.22
BSS 36	114.5502354	38.8587983	22.65	22.52	22.29
BSS 37	114.5724785	38.8543265	22.70	22.52	22.22
BSS 38	114.5377048	38.8776849	22.74	22.56	22.38
BSS 39	114.5367933	38.8863131	22.75	22.56	22.25
BSS 40	114.5370632	38.8841385	22.65	22.57	22.41
BSS 41	114.5416913	38.8744374	22.80	22.57	22.20
BSS 42	114.5328193	38.8783052	22.61	22.57	22.29

(continued on next page)

Table 5.1 – continued from previous page

Name	RA[degree]	Dec[degree]	B	V	I
BSS 43	114.5410755	38.8636039	22.70	22.58	22.35
BSS 44	114.5443444	38.8841840	22.78	22.58	22.18
BSS 45	114.5355871	38.8586443	22.72	22.59	22.29
BSS 46	114.5330413	38.8827233	22.75	22.59	22.34
BSS 47	114.5100504	38.8739744	22.78	22.59	22.38
BSS 48	114.5394051	38.8758936	22.74	22.60	22.44
BSS 49	114.5271347	38.8795152	22.76	22.61	22.42
BSS 50	114.5277051	38.8748074	22.77	22.64	22.42
BSS 51	114.5364186	38.8728954	22.88	22.65	22.22
BSS 52	114.5358544	38.8787353	22.86	22.66	22.44
BSS 53	114.4982285	38.8531324	22.78	22.67	22.14
BSS 54	114.5145126	38.8789390	22.88	22.69	22.41
BSS 55	114.5136075	38.8758341	22.84	22.70	22.50
BSS 56	114.5436548	38.8769220	22.94	22.70	22.35
BSS 57	114.5435517	38.8814084	22.92	22.70	22.40
BSS 58	114.5381816	38.8832314	22.99	22.71	22.25
BSS 59	114.5366860	38.8800032	22.88	22.72	22.39
BSS 60	114.5285765	38.8761503	22.82	22.72	22.40
BSS 61	114.5653514	38.8672278	22.90	22.74	22.41
BSS 62	114.5319576	38.8456597	22.89	22.74	22.52
BSS 63	114.5332823	38.8808548	22.90	22.75	22.50
BSS 64	114.5201658	38.8716290	23.05	22.75	22.49
BSS 65	114.5182917	38.8645682	22.93	22.76	22.43
BSS 66	114.5422667	38.8810701	23.00	22.77	22.48
BSS 67	114.5383605	38.8855947	23.02	22.77	22.42
BSS 68	114.5228769	38.8715036	22.95	22.78	22.58
BSS 69	114.5655782	38.8738971	22.95	22.79	22.54
BSS 70	114.5508635	38.8556174	22.91	22.80	22.44
BSS 71	114.5248251	38.8798819	23.03	22.80	22.50
BSS 72	114.5330946	38.8782802	22.94	22.81	22.42
BSS 73	114.5300473	38.8726778	22.99	22.82	22.42
BSS 74	114.5258531	38.8844487	22.98	22.82	22.57
BSS 75	114.5348296	38.8738382	23.04	22.84	22.40
BSS 76	114.5148586	38.8769283	23.00	22.85	22.74
BSS 77	114.5516168	38.8734430	23.02	22.85	22.62
BSS 78	114.5466460	38.8781617	23.02	22.86	22.60
BSS 79	114.5394030	38.8844577	23.08	22.86	22.43
BSS 80	114.5282537	38.8767212	23.03	22.88	22.50
BSS 81	114.5306900	38.8770293	23.08	22.89	22.55
BSS 82	114.5385251	38.8771382	23.00	22.90	22.66
BSS 83	114.5235814	38.8729527	23.16	22.92	22.48
BSS 84	114.5355456	38.8739955	23.18	22.92	22.46
BSS 85	114.5333547	38.8705373	23.05	22.93	22.76
BSS 86	114.5268290	38.8888513	23.08	22.93	22.65

(continued on next page)

Table 5.1 – continued from previous page

Name	RA[degree]	Dec[degree]	B	V	I
BSS 87	114.5286345	38.8824567	23.17	22.95	22.57
BSS 88	114.5272080	38.8829733	23.15	22.97	22.68
BSS 89	114.5297549	38.8842508	23.17	22.97	22.74
BSS 90	114.5374061	38.8851489	23.23	22.98	22.72
BSS 91	114.5305231	38.8777378	23.19	22.99	22.63
BSS 92	114.5306248	38.8655249	23.12	23.00	22.44
BSS 93	114.5298495	38.8808827	23.18	23.00	22.55
BSS 94	114.5250029	38.8861768	23.26	23.00	22.62
BSS 95	114.5319072	38.8857620	23.20	23.01	22.75
BSS 96	114.5766634	38.8573333	23.27	23.02	22.64
BSS 97	114.5540530	38.8462298	23.17	23.03	22.62
BSS 98	114.5446661	38.8786382	23.24	23.04	22.85
BSS 99	114.5416242	38.8825834	23.19	23.04	22.57
BSS 100	114.5559916	38.8782646	23.32	23.06	22.67
BSS 101	114.5467694	38.8799242	23.34	23.07	22.71
BSS 102	114.5245139	38.8773725	23.24	23.07	22.71
BSS 103	114.5335661	38.8876156	23.24	23.07	22.85
BSS 104	114.5338201	38.8808881	23.32	23.07	22.79
BSS 105	114.5251903	38.8708786	23.30	23.07	22.63
BSS 106	114.5155847	38.8515763	23.25	23.08	22.62
BSS 107	114.5482144	38.8762432	23.24	23.09	22.69
BSS 108	114.5283801	38.8804424	23.32	23.09	22.73
BSS 109	114.5272202	38.8806563	23.33	23.09	22.75
BSS 110	114.5329037	38.8787814	23.21	23.10	22.82
BSS 111	114.5648250	38.8809186	23.39	23.10	22.67
BSS 112	114.5655476	38.8353859	23.08	23.11	22.62
BSS 113	114.5340609	38.8672425	23.38	23.11	22.72
BSS 114	114.5241875	38.8826388	23.39	23.11	22.76
BSS 115	114.5440484	38.8728605	23.33	23.12	22.70
BSS 116	114.5318474	38.8804939	23.31	23.12	22.82
BSS 117	114.4975565	38.8498301	23.36	23.14	22.69
BSS 118	114.5308869	38.8858920	23.31	23.14	22.65
BSS 119	114.5319236	38.8814812	23.39	23.14	22.77
BSS 120	114.5365736	38.8749561	23.34	23.14	22.74
BSS 121	114.5548031	38.8770840	23.36	23.15	22.84
BSS 122	114.5698279	38.8632929	23.43	23.15	22.88
BSS 123	114.5429103	38.8833364	23.26	23.15	22.81
BSS 124	114.5180654	38.8526066	23.35	23.15	22.81
BSS 125	114.5713938	38.8644595	23.41	23.15	22.81
BSS 126	114.5151887	38.8881692	23.29	23.16	22.85
BSS 127	114.4971710	38.8503894	23.39	23.18	22.80
BSS 128	114.5389324	38.8662627	23.35	23.18	22.72
BSS 129	114.5653667	38.8735289	23.35	23.19	22.80
BSS 130	114.5290415	38.8850904	23.46	23.19	22.82

(continued on next page)

Table 5.1 – continued from previous page

Name	RA[degree]	Dec[degree]	B	V	I
BSS 131	114.5263335	38.8860022	23.29	23.20	22.80
BSS 132	114.5704264	38.8781784	23.35	23.20	22.91
BSS 133	114.5450942	38.8616024	23.42	23.21	22.90
BSS 134	114.5261968	38.8738325	23.43	23.21	22.75
BSS 135	114.5411974	38.8462718	23.46	23.21	22.85
BSS 136	114.5459761	38.8828031	23.37	23.21	22.86
BSS 137	114.5219796	38.8885754	23.44	23.25	22.97
BSS 138	114.5550069	38.8277938	23.47	23.26	22.97
BSS 139	114.5343111	38.8853578	23.49	23.27	22.86
BSS 140	114.5707653	38.8713824	23.52	23.27	22.85
BSS 141	114.5633208	38.8755186	23.52	23.28	22.91
BSS 142	114.5372475	38.8697969	23.58	23.29	22.83
BSS 143	114.5128112	38.8761214	23.54	23.30	22.95
BSS 144	114.5303288	38.8832148	23.55	23.31	22.99
BSS 145	114.5293403	38.8792390	23.56	23.31	22.81
BSS 146	114.5403815	38.8621857	23.46	23.32	22.93
BSS 147	114.5328409	38.8759082	23.58	23.34	23.02
BSS 148	114.5058275	38.8390039	23.55	23.35	22.96
BSS 149	114.5354601	38.8773111	23.55	23.38	22.94
BSS 150	114.5289120	38.8672031	23.58	23.38	22.88
BSS 151	114.5165945	38.8734688	23.51	23.39	23.01
BSS 152	114.5364602	38.8814663	22.50	22.51	22.27
BSS 153	114.5340522	38.8779415	22.62	22.62	22.42
BSS 154	114.5347666	38.8829015	22.75	22.79	22.62
BSS 155	114.5593850	38.8513222	22.80	22.76	22.40
BSS 156	114.5358572	38.8710266	22.88	22.91	22.47
BSS 157	114.5439332	38.8315146	22.97	22.98	22.51
BSS 158	114.5550096	38.8666358	22.95	22.60	22.59
BSS 159	114.5358955	38.8824612	23.24	22.88	22.63
BSS 160	114.5736822	38.8698082	23.27	22.95	22.64
BSS 161	114.5383375	38.8831536	23.28	22.89	22.53
BSS 162	114.5363135	38.8768683	23.34	22.97	22.70
BSS 163	114.5411630	38.8818491	23.37	22.99	22.73
BSS 164	114.5385990	38.8814390	23.46	23.16	22.74
BSS 165	114.5303744	38.8839579	23.53	23.22	22.90
BSS 166	114.5342489	38.8869653	23.55	23.52	23.12
BSS 167	114.5326253	38.8762184	23.56	23.18	22.82
BSS 168	114.5274273	38.8465093	22.44	22.52	22.09
BSS 169	114.5294680	38.8762898	21.67	-	21.58
BSS 170	114.5590138	38.8529876	22.61	-	22.13
BSS 171	114.5352678	38.8831155	23.27	-	22.54
BSS 172	114.5293589	38.8824958	23.28	-	22.54
BSS 173	114.5331303	38.8781672	22.37	-	21.82
BSS 174	114.5372462	38.8804816	22.38	-	21.92

(continued on next page)

Table 5.1 – continued from previous page

Name	RA[degree]	Dec[degree]	B	V	I
BSS 175	114.5371350	38.8825563	23.11	-	22.68
BSS 176	114.5299404	38.8833588	23.03	-	22.66
BSS 177	114.5377141	38.8839299	22.28	-	21.96
BSS 178	114.5318896	38.8816916	23.40	-	22.72
BSS 179	114.5338975	38.8878113	22.30	-	21.76
BSS 180	114.5354840	38.8848507	21.99	-	21.99
BSS 181	114.5416767	38.8787643	22.16	-	21.86
BSS 182	114.5274273	38.8465093	22.44	-	22.09
BSS 183	114.5430587	38.8788861	22.52	-	22.27
BSS 184	114.6046393	38.8739340	-	21.61	21.50
BSS 185	114.4732159	38.8794161	-	22.22	22.11
BSS 186	114.5948464	38.8317186	-	22.29	22.18
BSS 187	114.4921101	38.8826003	-	22.36	22.13
BSS 188	114.4795474	38.8950070	-	22.42	22.00
BSS 189	114.5742838	38.8787606	-	22.51	22.11
BSS 190	114.5769900	38.8517555	-	22.53	22.25
BSS 191	114.5235357	38.9041986	-	22.57	22.32
BSS 192	114.6028209	38.8986391	-	22.59	22.26
BSS 193	114.5780235	38.8817962	-	22.63	22.39
BSS 194	114.5205417	38.9003089	-	22.65	22.44
BSS 195	114.5574956	38.8950661	-	22.68	22.37
BSS 196	114.6020290	38.8716163	-	22.69	22.43
BSS 197	114.4870399	38.8486762	-	22.73	22.39
BSS 198	114.5278361	38.9056871	-	22.74	22.37
BSS 199	114.4868008	38.8777003	-	22.75	22.48
BSS 200	114.5698058	38.8856298	-	22.80	22.43
BSS 201	114.5631611	38.9001108	-	22.80	22.45
BSS 202	114.5728569	38.9152703	-	22.80	22.53
BSS 203	114.5344124	38.9094217	-	22.82	22.45
BSS 204	114.4987279	38.9233287	-	22.84	22.50
BSS 205	114.4950878	38.9045856	-	22.90	22.61
BSS 206	114.5542729	38.8926652	-	22.93	22.61
BSS 207	114.4846796	38.8934777	-	22.96	22.63
BSS 208	114.4793021	38.8865969	-	22.96	22.81
BSS 209	114.4748604	38.9055783	-	22.98	22.61
BSS 210	114.5080023	38.9026343	-	22.97	22.72
BSS 211	114.5573887	38.8903576	-	22.98	22.63
BSS 212	114.5204611	38.9028901	-	23.08	22.85
BSS 213	114.5705620	38.8861123	-	23.09	22.81
BSS 214	114.5548202	38.9085582	-	23.11	22.72
BSS 215	114.5422886	38.8977372	-	23.12	22.84
BSS 216	114.4864816	38.8823681	-	23.16	22.77
BSS 217	114.5658903	38.8861262	-	23.17	22.84
BSS 218	114.5066897	38.8939685	-	23.20	22.79

(continued on next page)

Table 5.1 – continued from previous page

Name	RA[degree]	Dec[degree]	B	V	I
BSS 219	114.4888325	38.8881818	-	23.27	22.80
BSS 220	114.5077125	38.9123421	-	23.27	22.81
BSS 221	114.4809893	38.8830761	-	23.27	23.04
BSS 222	114.5560389	38.8862473	-	23.29	23.07
BSS 223	114.4463878	38.8771839	-	22.20	22.10
BSS 224	114.3957223	38.8532619	-	22.65	22.27
BSS 225	114.4183885	38.8968389	-	22.86	22.52
BSS 226	114.4386092	38.8140150	-	22.90	22.59
BSS 227	114.3704635	38.8294846	-	23.09	22.73
BSS 228	114.5111720	38.9412987	-	22.61	22.43
BSS 229	114.5357260	39.0140900	-	22.74	22.47
BSS 230	114.4848049	38.9588305	-	22.99	22.67
BSS 231	114.7046122	38.8578500	-	22.18	21.92
BSS 232	114.6843307	38.9221184	-	23.28	22.83

r_i''	r_e''	$N_{\rm BSS}$	$N_{\rm HB}$	$N_{\rm RGB}$	$L^{\rm samp}/L^{\rm samp}_{\rm tot}$
0	20	56	160	745	0.21
20	60	71	253	1137	0.31
60	100	41	142	592 (1)	0.21
100	180	43 (1)	121 (1)	497 (3)	0.18
180	500	15 (5)	77 (11)	248 (27)	0.09

Table 5.2: Number Counts of BSS, HB, and RGB Stars, and Fraction of Sampled Luminosity. The values listed out of the parenthesis correspond to the number of stars assumed to belong to the cluster (and thus used in the analysis), while those in the parenthesis are estimated to be contaminating field stars (see Sect. 5.4).

Chapter 6

Blue Straggler Stars in the Unusual Globular Cluster NGC 6388

Based on the results published in:

Dalessandro, E.; Lanzoni, B.; Ferraro, F. R.; Rood, R. T.; Milone, A.; Piotto, G.; Valenti, E.; 2008ApJ, 677.1069D

Abstract

We have used multi-band high resolution HST WFPC2 and ACS observations combined with wide field ground-based observations to study the blue straggler star (BSS) population in the galactic globular cluster NGC 6388. As in several other clusters we have studied, the BSS distribution is found to be bimodal: highly peaked in the cluster center, rapidly decreasing at intermediate radii, and rising again at larger radii. In other clusters the sparsely populated intermediate-radius region (or "zone of avoidance") corresponds well to that part of the cluster where dynamical friction would have caused the more massive BSS or their binary progenitors to settle to the cluster center. Instead, in NGC 6388, BSS still populate a region that should have been cleaned out by dynamical friction effects, thus suggesting that dynamical friction is somehow less efficient than expected. As by-product of these observations, the peculiar morphology of the horizontal branch (HB) is also confirmed. In particular, within the (very extended) blue portion of the HB we are able to clearly characterize three sub-populations: ordinary blue HB stars, extreme HB stars, and blue hook stars. Each of these populations has a radial distribution which is indistinguishable from normal cluster stars.

6.1 Observations and data analysis

6.1.1 The data sets

We have used a combination of high-resolution and wide-field photometric data sets:

1. The High resolution set consists of a series of public multiband (from the UV, to the optical) WFPC2 and ACS *HST* images, which have been retrieved from the ESO/ST-ECF Science Archive. The WFPC2 images were obtained through filters $F255W$ (mid-UV) and $F336W$ (U), with total exposure times ($t_{\rm exp}$) of 9200 and 1060 s, respectively (Prop. 8718, P.I. Piotto), and trough filters $F439W$ (B) and $F555W$ (V), with $t_{\rm exp} = 370$ and 62 s, respectively (Prop. 6095, P.I. Djorgovski). This combined dataset allows us to examine both the hot (HB and BSS) and the cool (RGB and SGB) stellar populations in the cluster. In this dataset the planetary camera (PC, with the highest resolution of $\sim 0\farcs046\,{\rm pixel}^{-1}$) was roughly centered on the cluster center, while the wide field cameras (WFCs, at a lower resolution of $\sim 0\farcs1\,{\rm pixel}^{-1}$) sampled the surrounding outer regions. The photometric reduction of these images was performed using ROMAFOT (Buonanno at al. 1983), a package developed to perform accurate photometry in crowded regions and specifically optimized to handle under-sampled Point Spread Functions (PSFs; Buonanno & Iannicola 1989), as in the case of the WF chips. The ACS dataset is composed of a series of images (Prop. 9821, P.I. Pritzl) obtained through filters $F435W$ (B) and $F606W$ (V), with $t_{\rm exp} = 11$ and 7 s, respectively. It gives complete coverage of the central cluster region out to $110''$ from the center (see the following section). All the ACS images were corrected for geometric distortions and effective flux (Sirianni et al. 2005). The photometric analysis was performed independently in the two images by using the the aperture photometry code SExtractor (Bertin & Arnouts 1996) and adopting an aperture radius of 3 pixels (corresponding to $0\farcs15$).

2. The Wide field set is a complementary set of public B and V images obtained with the Wide Field Imager (WFI) mounted at the 2.2m ESO-MPI telescope at La Silla ESO-Observatory and retrieved from the ESO Science Archive. The WFI is a mosaic of 8-CCD chips, each of 2000×4000 pixels, with a pixel size of $\sim 0\farcs24$. It has exceptional image capability, with a global field of view (FoV) of $33' \times 34'$. Thanks to such a FoV, this dataset covers the entire cluster extension with the cluster roughly centered on the CCD #7. The WFI images have been corrected for flatness, bias and overscan using IRAF tools. The PSF fitting was performed independently on each image using DAOPHOT (Stetson 1987).

Parameter	Value	
Center of Gravity	$\alpha_{\rm J2000} = 17^{\rm h}\,36^{\rm m}\,17^{\rm s}.23$	$\delta_{J2000} = -44^\circ\,44'\,07''.1$
Concentration (c)	1.8	
Core Radius (r_c)	$7''.2$ (0.46 pc)	
Tidal radius (r_t)	$454''$(29 pc)	
Distance	$(m-M)_0 = 15.60$ (13.2 kpc)	
Reddening	$E(B-V) = 0.32$	

Table 6.1: Adopted cluster parameters

6.1.2 Astrometry, Photometric Calibration, and Sample Definition

Using the procedure described in Ferraro et al. (2001, 2003) the WFI catalogue has been placed on the absolute astrometric system. The 8 WFI CCDs have been astrometrized by cross-correlating each of them with the new astrometric 2-MASS catalogue using a specific tool developed at Bologna Observatory. Several hundred astrometric reference stars were found in each WFI chip, thus allowing an accurate absolute positioning of the sources. As a second step, a few hundred stars in the overlapping area between the WFI, and the WFPC2 and ACS FoVs were used as secondary astrometric standards, in order to place the *HST* catalogs on the absolute astrometric system. At the end of the procedure the rms residuals (that we take as representative of the astrometric accuracy) were of the order of $\sim 0''.3$ both in RA and Dec.

By using the procedure described in Ferraro et al. (1997, 2001), the photometric calibration of the UV magnitudes ($F255W$ and $F336W$) has been performed in the STMAG system, adopting the (Holtzman et al. 1995) zero-points. The optical (B and V) magnitudes have been transformed to the Johnson system by using the stars in common with the catalog of Piotto et al. (2002). Linear transformations were adopted, and only small color equation terms were required to correct the response of the different filter profiles.

Final lists with the absolute coordinates and homogeneous magnitudes for all the stars in the three considered catalogs were obtained. To minimize incompleteness effects in the ground based observations of the crowded central regions of the cluster, while still taking advantage of the superior capability of UV observations in detecting the BSS (Ferraro et al 1999a, 2001), we divided the dataset in two main samples: The *HST sample*, includes only stars in the WFPC2 and complementary ACS catalogs. It covers approximately the inner $r < 110''$ of the system (with the WFPC2 FoV almost entirely included in the ACS FoV; see Figure 6.1). The *WFI sample* includes only stars observed with WFI and lying beyond the WFPC2 and ACS FoVs. The *WFI*

sample covers the outer regions, well beyond the cluster extension (see Figure 6.2).

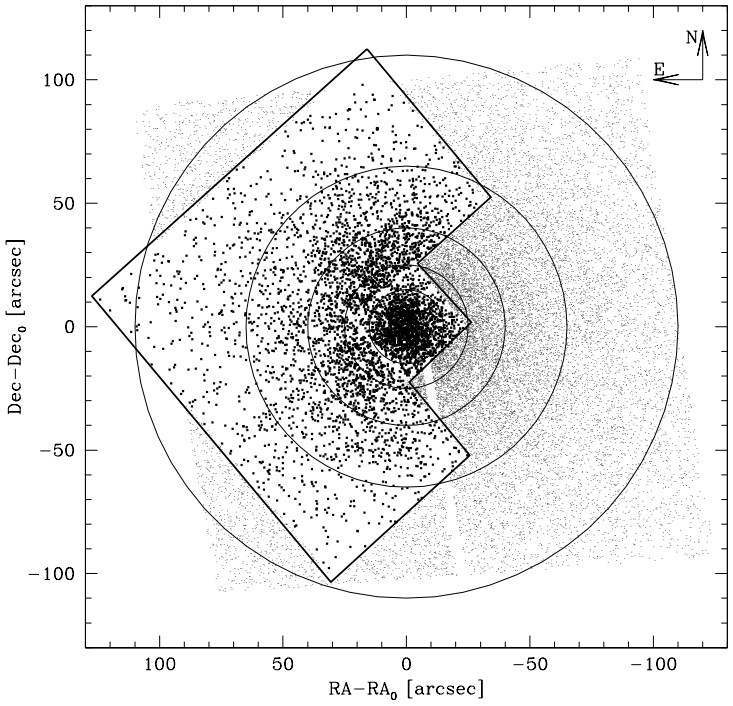

Figure 6.1: Map of the *HST sample*. The thick solid line delimits the WFPC2 *HST* FoV. The concentric annuli are used to study the radial distribution of BSSs. The inner and the outer annuli correspond to $r = 5''$ and $r = 110''$, respectively.

By combining the data sets described above, with additional images of the cluster center obtained with the *HST* ACS High Resolution Camera, very accurate determinations of the center of gravity, surface density profile, and surface brightness profile have been recently obtained by (Lanzoni et al. 2007d). In particular, it has been found that the observed profiles show a deviation from a flat core behavior in the inner $\sim 1''$, suggesting that NGC 6388 might host an IMBH of $\sim 5.7 \times 10^3\, M_\odot$ in its center. However, by excluding the points at $r < 1''$, the density profile is well fit by an isotropic single-mass King model. The resulting cluster structural parameters (concentration, core radius and tidal radius) are listed in Table 6.1, together with the new estimate of the center of gravity.

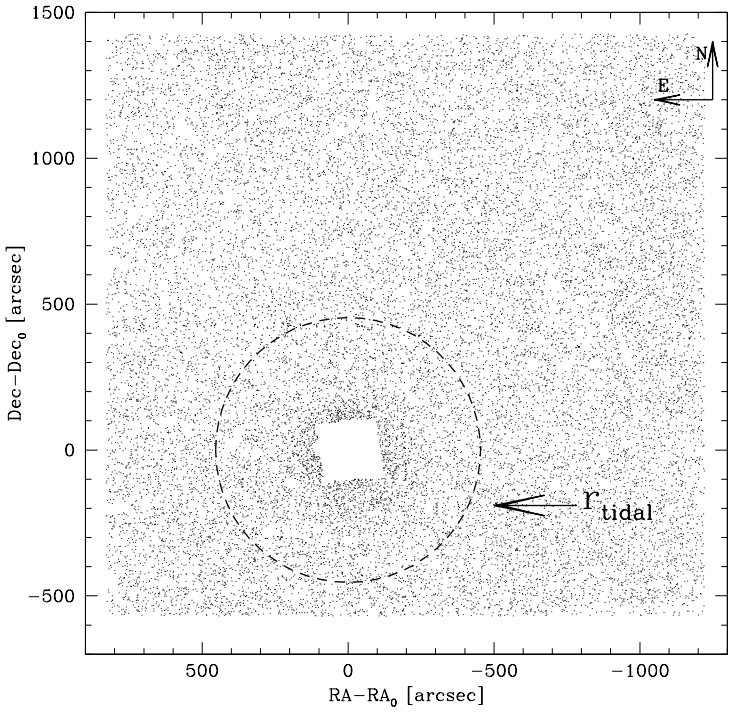

Figure 6.2: Map of the *WFI sample*. This sample has been used to estimate the structural parameters of NGC 6388 and the Galaxy contamination, but not for constructing the radial distribution of BSS. The dashed line marks the cluster tidal radius ($r_t = 454''$).

6.2 CMD overview

6.2.1 The HST sample

The CMDs of the *HST sample* in the UV and the optical bands are shown in Figures 6.3 and 6.4, respectively. As apparent, all of the cluster evolutionary sequences are clearly defined and well populated.

Particularly notable is the Horizontal Branch (HB) morphology. Beside the red clump, which is a typical feature of metal rich stellar populations, the HB clearly shows an extended blue tail (BT), first noticed by Rich et al. (1997) and by Piotto at al. (1997). Among a total of 1763 HB stars counted in the *HST sample*, five sub-populations can be distinguished (see Sect. 6.2.2 and 6.2.3 for details): *(i)* the red-HB (RHB) population, consisting of 1418 stars grouped in the red clump; *(ii)* 15 RR Lyrae variables, which we identified by cross correlating the positions in our catalog with those published by Pritzl et al. (2002) [1]; *(iii)* 267 blue-HB (BHB) stars ; *(iv)* 26

[1]Since our photometry is just a snapshot, the position of each variable star in the CMD is not an indication of the

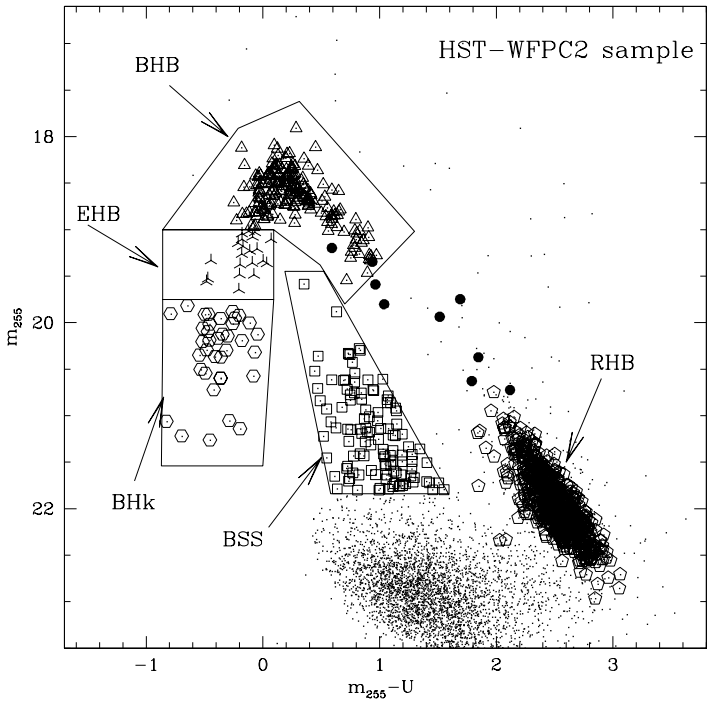

Figure 6.3: Ultraviolet CMD of the *HST* WFPC2 sample. The different stellar populations discussed in the paper are marked with different symbols, as indicated by the labels. Solid dots mark the selected RR Lyrae stars.

Extreme-HB (EHB) stars ; and *(v)* 37 Blue Hook (BHk, to avoid confusion with BH for black hole) stars.

Several previous works have shown that the HB morphology in NGC 6388 is complex. A new extensive study, based on much of the same observational data used here, and also discussing the HB morphology of NGC 6441, has recently been published by Busso et al. 2007. In the present paper we take advantage of the complex HB structure of NGC 6388 to review the HB nomenclature, which has become rather confused in the literature and is often ambiguously used. Then, we briefly discuss the blue HB sub-populations and the HB red clump, the latter being used as cluster reference population for the study of the BSS radial distribution (Sect. 6.3.2).

mean properties. The remaining stars found within the ”RR Lyrae region” of the CMD, but not included in the Pritzl et al. catalog are not considered in the following analysis, since they possibly are field contaminating stars.

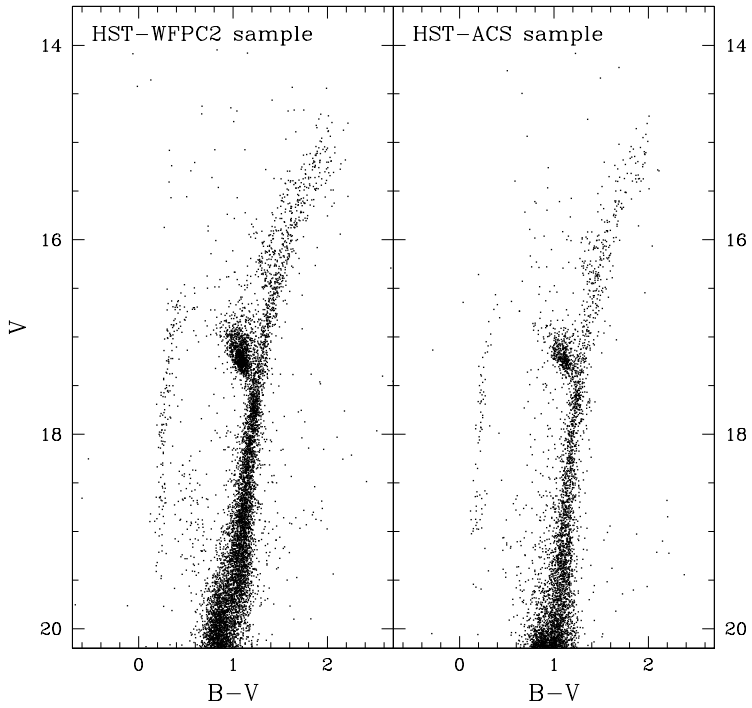

Figure 6.4: Optical CMDs of the *HST* WFPC2 and the complementary ACS samples.

6.2.2 The HB population: nomenclature and radial distribution

The HB is composed by helium-core/hydrogen-shell burning stars. It is traditionally split into red, variable, and blue (RHB, VHB, and BHB, respectively), depending on whether the stars are redder than, within, or bluer than, the RR Lyrae instability strip.

The concept of *HB blue tails* probably originated with the CMD of NGC 6752, which was presented by Russell Cannon at the 1973 Frascati globular cluster workshop, but not published for many years. In visual CMDs of NGC 6752 (and many others to follow), the HB drops downward at high temperature often becoming an almost vertical sequence. This feature looked like a tail hanging from the horizontal part of the BHB, hence the name. Rood & Crocker(1989), Fusi Pecci et al (1993), and Recio-Blanco et al. (2006) have each suggested ways to measure BTs, and the fact that measures of BTness keep being invented demonstrates a lack of consensus on a definition of BTs. In addition, sub-populations like EHB or BHk stars are sometimes recognized within the observed BTs, even if without a precise observational definition.

The *extreme HB* population is theoretically well defined: EHB stars lie at the hottest extreme

of the zero-age HB (ZAHB), and they do not return to the asymptotic giant branch (AGB), but rather spend their He-shell burning phase as hot AGB-manqué or Post-early AGB stars (Dorman et al 1993). There is no comparably precise way to observationally select EHB stars. If far-UV (FUV) (e.g., *HST* F160BW) photometry is available, detailed comparisons with stellar models can be made. These suggest that in a few clusters, the transition between BHB and EHB stars may be associated with a gap in the HB morphology (Ferraro et al. 1998). In the present paper we have assumed this to be the case (see below), but at this point that is only an assumption. The importance of EHB stars is also connected with the fact that they and their progeny are thought to be the source of the UV radiation excess observed in the integrated spectra of some elliptical galaxies (Dorman et al 1995; Yi et al. 1998), and one might be able, for example, to determine the age of the galaxy on the basis of its UV excess. In this context NGC 6388 plays a particularly important role, since it is one of the most metal-rich systems containing EHB stars that can be individually observed.

In a few clusters, including NGC 6388, there is an additional population hotter and less luminous than the EHB stars. Following nomenclature used in recent studies, we call this population *Blue Hook* stars. In visual and even some UV (e.g., $m_{255},\ m_{255}-m_{336}$) CMDs, BHk stars appear as fainter extension of the BT and are separated from the EHB population by a gap. While the effective temperature T_{eff} of HB stars can be reasonably well determined from their position along the BT, it is not appropriate to extrapolate this to the BHk. Accurate stellar parameters for BHk stars require FUV photometry (see for example the BHk studies in NGC 2808 and ω Cen by Moehler et al. 2004) . Indeed, it is only in FUV CMDs that the origin of the name "blue hook" becomes apparent.

Not all BT clusters have EHB stars (see the case of NGC 1904; Lanzoni et al. 2007b), and not all clusters with EHB stars have BHk stars (see the cases of M13 and M80; Ferarro et al. 1998). In order to clearly show the difference between cluster with BTs populated up to the EHB region, and clusters with BHk stars, UV photometry is essential. In Figure 6.5 we compare the ($m_{255},\ m_{255}-U$) CMDs of NGC 6388 to that of M80 (Ferraro et al. 1997, 1999a).

We chose M80 because, among the clusters for which we have a full range of data, it is the one with the HB extending to highest T_{eff}. From comparison with evolutionary tracks in the ($m_{160},\ m_{160}-V$) plane (Dorman and Rood, unpublished) we know that the M80 HB is populated all the way to the extreme blue-end of the ZAHB. In this plane the HB of M80 shows a clear gap at the transition from BHB to EHB (Ferraro et al. 1998). In Fig. 6.5 this gap is also visible at

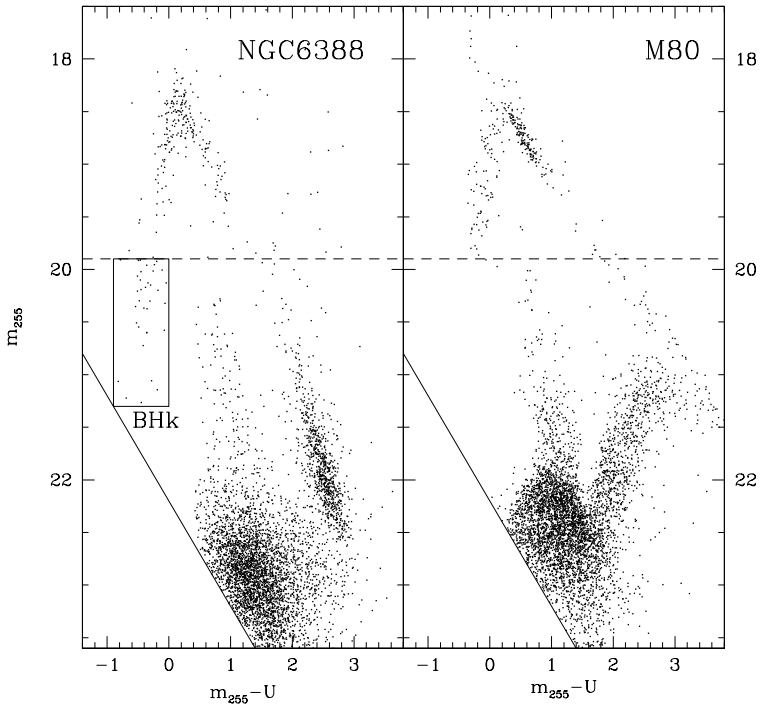

Figure 6.5: Comparison between the UV CMDs of NGC 6388 and M80. The latter has been suitably shifted in color and magnitude in order to superimpose the knees of the two HBs (at $m_{255} - U \simeq 0.2$ and $m_{255} \simeq 18.5$). The dotted line marks the limit ($m_{255} \simeq 20$) below which there are no more BHB stars in M80, and that we have adopted as the brightest boundary of the BHk population.

$m_{255} = 19$. Since there is a corresponding gap in NGC 6388, we tentatively identify the stars with $19.0 < m_{255} < 19.8$ as EHB. The HB sequence of NGC 6388 is significantly more extended than that observed in M80, where there is no analogous population at $m_{255} \simeq 20$. For that reason we identify the latter as BHk stars in NGC 6388, as do Busso et al. 2007. The BHk extends well below the cluster TO in the optical CMD: $V > 21$ in the $(V,\ B-V)$ plane (see Fig. 6.6). Because of the uncertainties in detection of these faint stars using optical wavelengths in such crowded regions, our BHk sample is selected from the UV CMD (WFPC2 sample). By using these criteria we have defined the selection boxes sketched in Figs. 6.3 and 6.6, and obtained the values quoted in the previous section for the number of HB stars belonging to each sub-population.

It has been suggested that EHB might originate in binary systems (Bailyn 1995), or they were formed through a collisional channel. Indeed, similar stars in the field and in old open clusters have been found to often belong to binary systems (Green et al. 2001, Heber et al. 2002). In

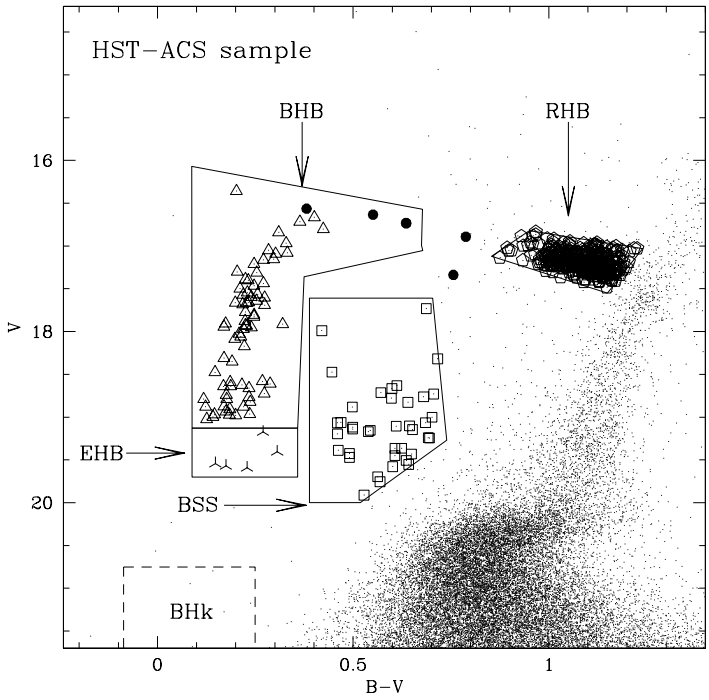

Figure 6.6: Zoom of the optical CMD of the complementary *HST* ACS sample, showing the different stellar populations discussed in the paper, marked as in Fig. 6.3. The selection box of BHk stars is marked as a dashed line, since this population is near the detection limits in the optical wavelengths.

contrast, a recent study by Moni Bidin et al. (2006) has found no evidence of binarity in the EHB population of two globular clusters (M80 and NGC 5986). The nature of BHk stars is still a matter of debate. They may be related to the so-called late hot flashers (Moeheler et al. 2004), or to high helium abundances (Busso et al. 2007). Given that the origin of EHB and BHk stars is still uncertain, it is useful to check whether their radial distributions show any suggestion of binarity or stellar interaction, as it is the case for BSS. We have therefore compared the cumulative radial distributions of the BHB, EHB, and BHk stars to that of RHB stars, which are representative of normal cluster populations (see Sect. 6.3.2). As shown in Figure 6.7, all radial distributions are consistent with being extracted from the same parent population, with Kolmogorov-Smirnov (KS) test probabilities of 59%, 46% and 60%, respectively. Thus, the radial distribution of BHB, EHB and BHk populations is consistent with that of normal cluster stars, in agreement with previous findings by Rich et al. (1997), and possibly suggesting a non-binary nature for these systems. However, a binary EHB star could consist of a 0.5 $M_{\odot}$ He-burning star with a 0.2 $M_{\odot}$ He white

dwarf companion, i.e., a total mass smaller than the TO mass and comparable to RHB masses. As a consequence, even if the initial binary mass were large enough to have sunk to the cluster core, the central relaxation time of NGC 6388 is 8.3×10^7 yr (Djorgovski 1993), less than the HB lifetime, so that an EHB binary could move outward, instead of being segregated into the center.

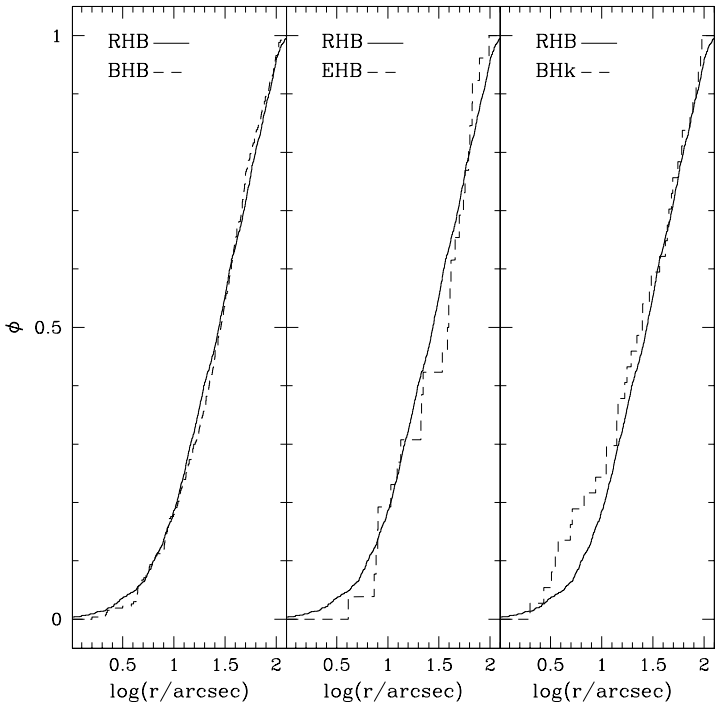

Figure 6.7: Cumulative radial distributions of BHB, EHB and BHk stars (dashed lines), compared to that of the reference RHB population. No evidences of peculiar radial distributions are found for the blue HB sub-populations, with respect to normal cluster stars.

6.2.3 The red HB clump and the distance of NGC 6388

Since the HB red clump in this cluster is very well defined in the optical CMDs, we have selected the RHB population in this plane, and then used the stars in common between the optical and the UV WFPC2 samples to identify it in the $(m_{255},\ m_{255} - U)$ CMD. The selected stars are marked as pentagons in Figs. 6.3 and 6.6.

With our high-quality data set and such a well defined HB red clump, we have estimated the distance modulus and the reddening of NGC 6388 by comparing its CMD and luminosity function to those of the proto-type of metal-rich GCs: 47 Tuc. As shown in Figure 6.8, other than the blue HB, the overall CMD properties of NGC 6388 closely resemble those of a normal metal-rich

cluster. In order to overlap the CMDs, and align the HB red clump and the RGB bump of the two clusters, the color and the magnitude of NGC 6388 have to be shifted by $\delta(B-V) = -0.28$ and $\delta V = -3.15$, respectively. Thus, by adopting $(m-M)_0 = 13.32$ and $E(B-V) = 0.04$ for 47 Tuc (Ferraro et al. 1999b), we obtain $(m-M)_V = 16.59$ and $E(B-V) = 0.32$ for NGC 6388. This yields a true (unreddened) distance modulus of $(m-M)_0 = 15.60 \pm 0.2$, which corresponds to a distance of 13.2 ± 1.2 Kpc (to be compared with 10 Kpc quoted by Harris 1996).

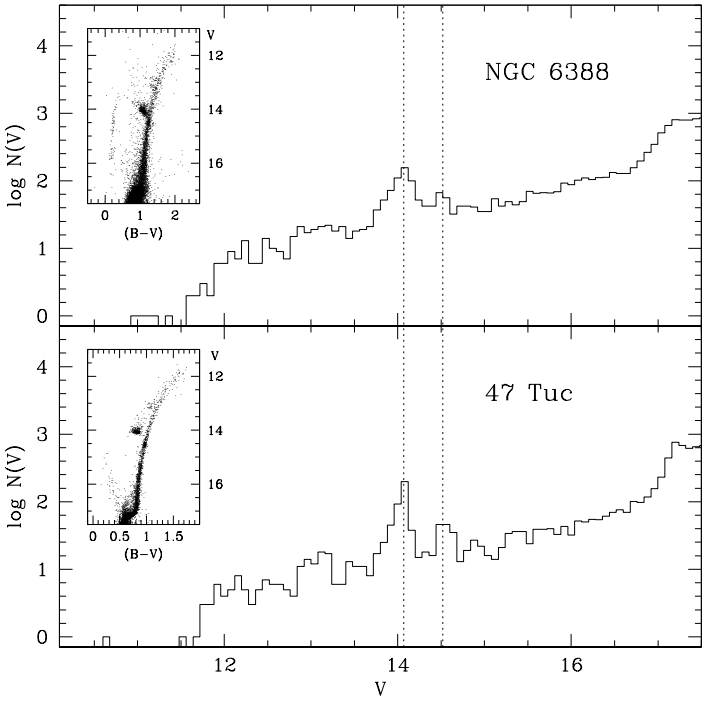

Figure 6.8: Differential Luminosity Function of NGC 6388 shifted to that of 47 Tuc. The dotted lines indicate the HB red clump and the RGB-bump level. From the inserts it is apparent that, other than the blue HB, the CMDs of the two clusters are quite similar.

The proper comparison of the CMDs of the two clusters deserves additional comments. First, NGC 6388 is known to be slightly more metal-rich ($[\mathrm{Fe/H}] = -0.44$; Carretta et al. 2007) than 47 Tuc ($[\mathrm{Fe/H}] \simeq -0.6$; Carretta et al. 2004). However, current theoretical models suggest that such a small overabundance ($\delta[\mathrm{Fe/H}] \sim 0.15$ dex) would generate just a small difference in the HB absolute magnitude ($\delta M_V^{\mathrm{HB}} \sim 0.03$ mag). Second, the presence of differential reddening of the order of 0.07 (see Busso et al. 2007) can spread the HB red clump, increasing the uncertainties of the entire procedure. However, this contribution is significantly smaller than the conservative

estimate of the error in the derived cluster distance, $\delta(m - M) = \pm 0.2$ mag. Finally, the morphology of the HB red clump is not exactly the same in the two clusters. However, as discussed by Catelan et al. 2006, who compared the two CMDs by using a reddening-independent quantity, the main difference between the two red HB clumps consists in the fact that the bluer RHB stars in NGC 6388 ($\sim 20\%$ of the total RHB population) are slightly brighter than the average in 47 Tuc. This feature might be interpreted in the framework of a sub-population with a higher helium content. However comparison of the luminosity functions in Figure 6.8 clearly shows that the relative position of the HB red clump and RGB bump is quite similar in the two clusters. Since the location in magnitude of the RGB bump is quite sensitive to the helium content (see Fusi Pecci et al. 1990), such a nice correspondence clearly demonstrates that at least the main component of the stellar population of NGC 6388 has an helium abundance fully compatible with that of 47 Tuc, while only a minor fraction of the cluster stars could be helium enhanced (this is also in agreement with the findings of Catelan et al. 2006, and Busso et al. 2007). The possible impact on the relative distance of the two clusters derived above is therefore negligible.

6.2.4 The WFI sample and background contamination

Figure 6.9 shows $(V,\ B - V)$ CMDs of four radial zones of the WFI sample. The sequences seen in Fig. 6.4 are still obvious in the interval $120'' < r < 250''$, but there is also significant contamination from field stars. The CMDs are progressively more contaminated as r increases: cluster sequences are barely visible in the region $250'' < r < 490''$, less so for $490'' < r < 800''$, and have vanished for $r > 800''$. The contamination has two main components (the bulge and the disk populations of the Galaxy): the first is an almost vertical blue sequence with $0.5 < (B - V) < 1.0$, the second is another vertical sequence with $(B - V) \sim 1.3$, which clearly indicates the presence of metal rich stars.

Indeed, Figure 6.9 shows that field contamination is particularly severe in this cluster. For this reason we decided to limit the following analysis to the *HST sample*, and to use the most external region of the WFI sample ($r > 800''$) to statistically estimate the field contamination level. We have counted the number of background stars and derived an appropriate background density for each selection box discussed in the paper (see Sect. 6.3 for the definition of the BSS population). Then, we have used this background density to statistically decontaminate each population in the *HST sample*, by following a procedure similar to that described by Bellazzini et al. 1999. Table 6.3 shows the observed sample size and the resulting statistical estimate of field contamination for each of the sub-populations in each radial region of the cluster. Statistical decontamination has

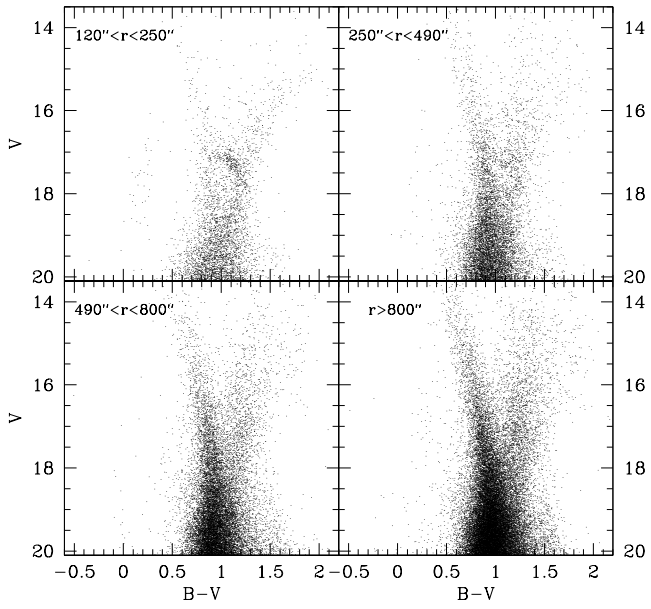

Figure 6.9: Optical CMDs of the *WFI sample* for four different radial ranges, as marked by the labels in each panel.

the disadvantage that we don't know whether a given star is a member of a given sub-population or not. However, all of the conclusions of the current paper depend on number counts, so that background correction only increases the noise without affecting the conclusions. Future proper motion studies currently ongoing for this cluster will finally assess the real membership of each star. Preliminary results indicate contamination counts which are in agreement with those listed in Table 6.3.

6.3 The Blue Straggler Star population

6.3.1 The BSS Selection

Hot populations like BSS and BHB stars are the brightest objects in UV CMDs, while the RGB stars, that dominate the emission of GCs in the optical bands, are faint at these wavelengths. In addition, the high spatial resolution of *HST* minimizes problems associated with photometric blends and crowding in the high density central regions. Thus *HST* UV CMDs are the optimal tool for selecting BSS in GCs. Given this, our main criterion for the selection of the BSS population

is the position of stars in the ($m_{255},\ m_{255} - U$) CMD. To avoid incompleteness biases and contamination from TO and sub-giant stars, we adopt a magnitude threshold that is about one magnitude brighter than the TO point: $m_{255} = 21.85$. Figure 6.3 shows the adopted selection box and the candidate BSS in the UV CMD. Using the BSS in common between the WFPC2 and the ACS FoVs, we have transformed the BSS selection box from the UV plane into the optical plane. To avoid regions with very high risk of Galactic contamination, we have considered only stars with $(B - V) < 0.7$. The resulting candidate BSS in the complementary ACS field are shown in Fig. 6.6.

The final sample is of 153 BSS in the *HST sample*: 114 are found in the WFPC2 dataset, and 39 in the complementary ACS sample. The magnitude and the positions of the selected BSS are listed in Table 6.2.

6.3.2 The BSS projected radial distribution

In order to study the radial distribution of BSS (or any other population) for detecting possible peculiarities, a reference population representative of normal cluster stars must be defined.

In our previous papers we have used both the RGB or the HB as reference populations. In NGC 6388 the RGB population is affected by a significantly larger field contamination, with respect to the HB. On the other hand, the HB morphology is quite complex, the presence of a BT in such a metal-rich cluster is unusual, and the nature of EHB and BHk stars is still unclear (see Sect. 6.2.2). Instead, the HB red clump is a common feature of similar metallicity GCs, it is bright and well defined both in the UV and in the optical CMDs, and it comprises the majority (80%) of the HB population (see Section 6.2.1). We have verified that RHB and RGB stars share the same radial distribution over the region ($r < 110''$), suggesting that RHB stars are indeed representative of normal cluster populations. For all these reasons, we have chosen the RHB as the reference population for NGC 6388.

We first compare the BSS and the RHB cumulative radial distributions. Since we expect a negligible number of field stars contaminating the BSS and RHB sample (see Table 6.3) no correction has been applied to the observed sample used to construct these cumulative radial distributions. As shown in Figure 6.10, the trend is bimodal, with the BSS more segregated than RHB stars in the central cluster regions, and less concentrated outward. The KS probability that the two populations are extracted from the same parent distribution is $\sim 10^{-4}$.

For a more quantitative analysis we have divided the surveyed area in 6 concentric annuli (sketched in Fig. 6.1), and the number of BSS ($N_{\rm BSS}$) and RHB ($N_{\rm RHB}$) stars was counted in each

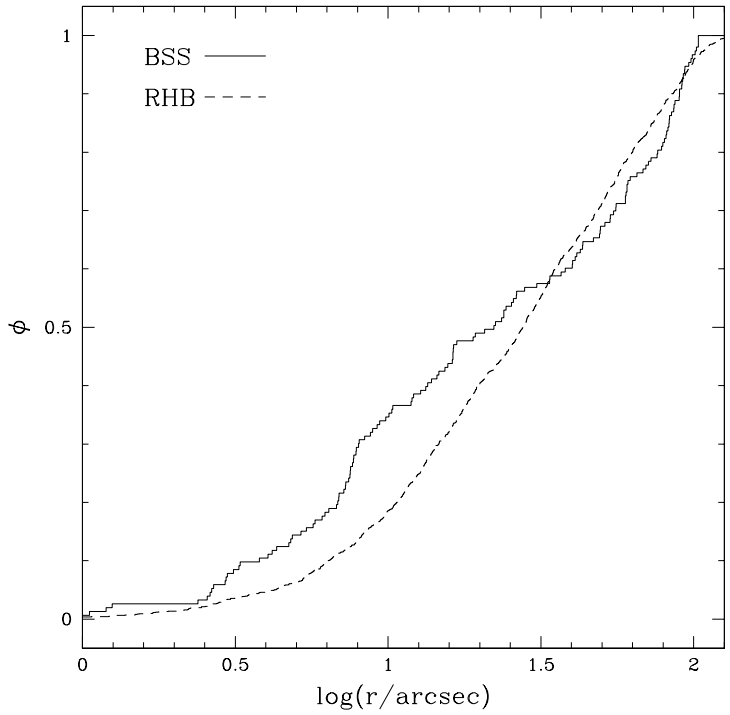

Figure 6.10: Cumulative radial distribution of BSS (solid line) and RHB stars (dashed line) as a function of the projected distance from the cluster center, for the combined HST sample. The probability that they are extracted from the same population is $\simeq 10^{-4}$.

annulus (see the values listed in Table 6.3). We have then computed the double normalized ratio (Ferraro et al. 1993):

$$R_{\rm pop} = \frac{N_{\rm pop}/N_{\rm pop}^{\rm tot}}{L^{\rm samp}/L_{\rm tot}^{\rm samp}}, \tag{6.1}$$

where pop=BSS, RHB, $N_{\rm pop}$ refers to statistically decontaminated number counts (see Sect. 6.2.4), and the luminosity in each annulus has been calculated by integrating the single-mass King model that best fits the observed surface density profile (see Lanzoni et al. 2007d) , with the distance modulus and the reddening previously quoted, and by properly taking into account the incomplete spatial coverage of the outermost annulus.

As expected from stellar evolution theory (Renzini & Fusi Pecci 1988), the radial trend of $R_{\rm RHB}$ is essentially constant with a value close to unity. On the contrary, the BSS radial distribution is very different and is clearly bimodal. As shown in Figure 6.11, $R_{\rm BSS}$ reaches a value of almost two at the center, while $R_{\rm RHB}$ has no central peak. $R_{\rm BSS}$ decreases to a minimun

near $r = 5\,r_c$, and rises again near $r = 11\,r_c$.

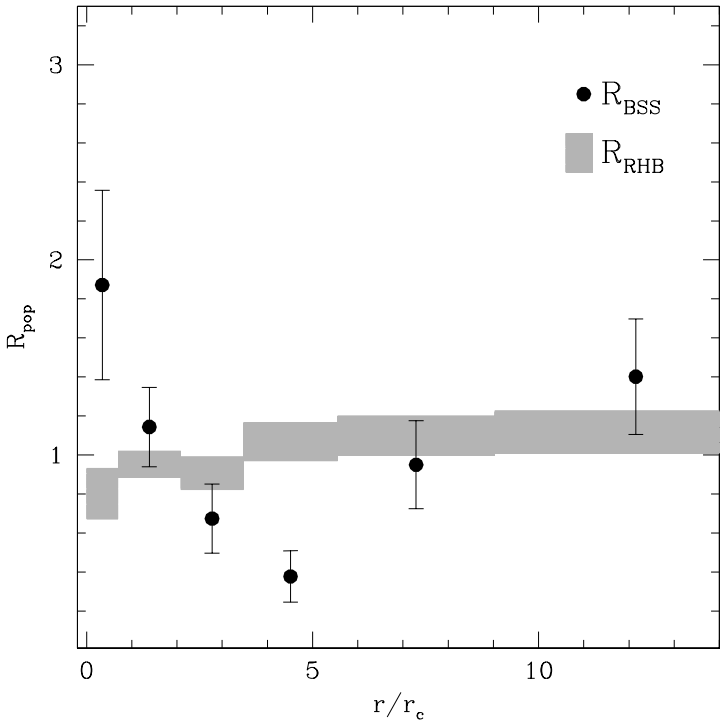

Figure 6.11: Radial distribution of the BSS and HB double normalized ratios, as defined in equation (6.1), plotted as a function of the radial coordinate expressed in units of the core radius. $R_{\rm RHB}$ (with the size of the rectangles corresponding to the error bars computed as described in Sabbi et al. 2004) is almost constant around unity over the entire cluster extension, as expected for any normal, non-segregated cluster population. Instead, the radial trend of $R_{\rm BSS}$ (dots with error bars) is bimodal: highly peaked in the center (more than a factor of ~ 2 higher than R_{RHB}), decreasing at intermediate radii, and rising again outward.

6.4 Discussion

In Figure 6.12 we have compared the radial distribution of the ratio between the BSS and HB number counts computed for NGC 6388, with that obtained for other GCs showing a bimodal distribution (see for example Lanzoni et al. 2007a). The position of the observed minimum in NGC 6388 resembles that of M3, but NGC 6388 has a core radius ~ 3 times smaller. In physical units its minimum is closer to the cluster center than in any previously observed cluster. By equating the dynamical friction timescale $t_{df} \propto \sigma^3/\rho$ (Binney & Tremaine 1987;see also Mapelli et al. 2006) to the cluster age (assumed to be $t = 12\,$Gyr), one can estimate the value of the

radius of avoidance ($r_{\rm avoid}$). This is defined as the radius within which all the stars of $\sim 1.2\,M_{\odot}$ (the expected average mass for BSS) have already sunk to the core because of dynamical friction effects.

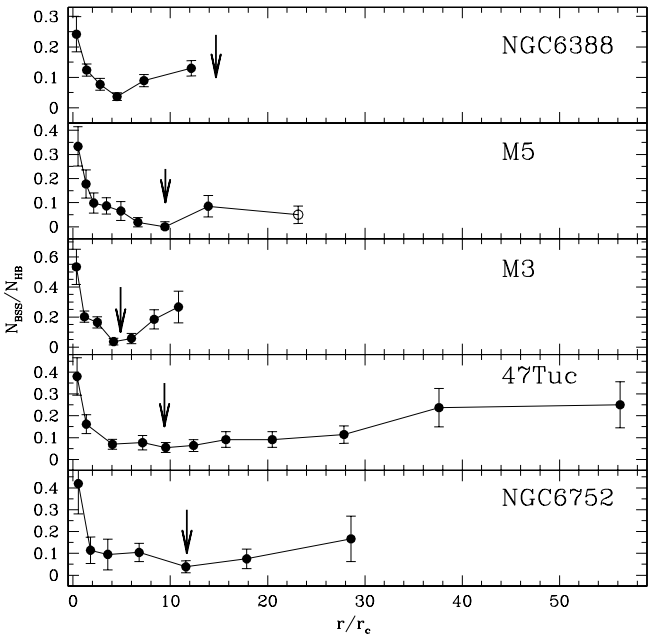

Figure 6.12: Radial distributions of the specific frequency $N_{\rm BSS}/N_{\rm HB}$, as observed for NGC 6388 and for other four clusters (see references in Lanzoni et al. 2007a). The arrows mark the position of the estimated radius of avoidance (see Sect. 6.4). This well corresponds to the position of the observed minimum of distributions, but in the case of NGC 6388.

As shown in Fig. 6.12, the position of $r_{\rm avoid}$ well corresponds to that of the observed minimum for all the clusters studied to date in a similar way. For NGC 6388, by adopting $\sigma_0 = 18.9\,{\rm km\,s^{-1}}$ and $n_0 = 10^6\ {\rm stars\,pc^{-3}}$ as central velocity dispersion and stellar density (Pryor & Meylan 1993), and by assuming the cluster structural parameters derived from the best-fit King model by Lanzoni et al. 2007d (see Table 6.1), we have obtained $r_{\rm avoid} \simeq 15\,r_c$. This is about 3 times larger than the location of observed minimum, thus representing the first case where the two distances do not coincide. This result is quite puzzling and somehow suggests that NGC 6388 appears "dynamically younger" than expected on the basis of its structural properties. In fact, our observations suggest that the dynamical friction in this cluster has been effective in segregating BSS (and similar massive objects) out to only 4–5 r_c, whereas the theoretical expectation indicates

that, within $15\,r_c$, all stars with the mass of BSS or their binary progenitors should have already sunk to the center. Note that significantly larger (by a factor of 2) velocity dispersion, or lower (by a factor of 7) central density would be necessary to reconcile the expected and the observed minima. Why is dynamical friction less efficient in this cluster? Could the presence of an IMBH in the cluster center be important? As discussed in Lanzoni et al (2007d), the radius of influence of a $5 \times 10^3\,M_\odot$ BH at the center of NGC 6388 is only 0.07 pc or $0.15\,r_c$, so it is not obvious how it might affect cluster evolution at 5–$15\,r_c$. Perhaps the BSS that we observe at $r \gg r_c$ are stars which have "visited" the central region and have been put on highly eccentric orbits by the interaction with the BH. However this effect would probably fill-in the BSS avoidance region in the projected radial distribution.

Table 6.2: The BSS population of NGC 6388.

Name	RA[degree]	Dec[degree]	m_{255}	U	B	V
BSS-1	264.0713276	-44.7367013	19.59	19.23	20.00	-
BSS-2	264.0744196	-44.7337510	19.88	19.25	18.32	17.88
BSS-3	264.0662077	-44.7330923	20.28	19.45	18.51	17.84
BSS-4	264.0684376	-44.7363620	20.30	19.46	18.46	17.71
BSS-5	264.0729064	-44.7351137	20.61	19.58	18.78	18.23
BSS-6	264.0759361	-44.7387021	20.34	19.60	18.81	18.27
BSS-7	264.0734613	-44.7342291	20.33	19.60	18.79	18.32
BSS-8	264.0719025	-44.7360255	20.34	19.61	18.81	18.38
BSS-9	264.0744172	-44.7344345	20.43	19.66	18.88	18.42
BSS-10	264.0728800	-44.7350638	20.79	19.71	18.84	18.07
BSS-11	264.0692420	-44.7364498	20.61	19.72	18.83	18.18
BSS-12	264.0900025	-44.7337870	20.55	19.76	18.79	18.32
BSS-13	264.0791273	-44.7265070	20.83	19.76	19.00	18.45
BSS-14	264.0703257	-44.7346882	20.86	19.77	18.95	18.41
BSS-15	264.0727463	-44.7348325	20.72	19.78	18.89	18.41
BSS-16	264.0908653	-44.7330954	20.92	19.78	19.13	18.50
BSS-17	264.0950506	-44.7305534	20.73	19.78	18.92	18.43
BSS-18	264.0755655	-44.7319929	20.86	19.79	18.94	18.37
BSS-19	264.0709775	-44.7343269	20.95	19.80	19.17	18.52
BSS-20	264.0729054	-44.7373249	20.64	19.85	19.17	18.57
BSS-21	264.0774606	-44.7203559	20.36	19.89	19.10	18.73
BSS-22	264.0712908	-44.7340081	20.61	19.91	18.94	18.51
BSS-23	264.0722999	-44.7418140	20.76	19.91	19.03	18.58
BSS-24	264.0692830	-44.7353270	20.62	19.93	19.15	18.68
BSS-25	264.0730816	-44.7373322	21.09	19.94	18.98	18.37
BSS-26	264.0711454	-44.7357811	20.76	19.97	19.18	18.64
BSS-27	264.0740359	-44.7366416	20.82	19.98	19.07	18.56
BSS-28	264.0690052	-44.7342695	20.97	19.98	19.05	18.51
BSS-29	264.0716947	-44.7360388	20.72	19.99	19.11	18.69
BSS-30	264.0734948	-44.7340751	21.20	20.00	19.13	18.41
BSS-31	264.0924983	-44.7371176	21.36	20.01	19.33	18.65
BSS-32	264.0712030	-44.7307819	20.61	20.02	19.15	18.66
BSS-33	264.0850725	-44.7117026	20.78	20.03	19.15	18.66
BSS-34	264.0721562	-44.7355198	20.94	20.06	19.13	18.67
BSS-35	264.0695609	-44.7353630	21.14	20.06	19.22	18.66
BSS-36	264.0811280	-44.7352173	21.05	20.07	19.70	18.90
BSS-37	264.0845995	-44.7288863	20.52	20.08	19.32	18.88
BSS-38	264.0713843	-44.7351224	21.21	20.08	19.41	18.90
BSS-39	264.0719022	-44.7328261	20.83	20.08	19.15	18.58
BSS-40	264.0731414	-44.7310496	21.33	20.09	19.32	18.70
BSS-41	264.0769106	-44.7325813	21.21	20.09	19.26	18.68
BSS-42	264.0675349	-44.7325655	21.01	20.10	19.37	18.81

(continued on next page)

Table 6.2 – continued from previous page

Name	RA[degree]	Dec[degree]	m_{255}	U	B	V
BSS-43	264.0980263	-44.7236097	21.51	20.10	19.38	18.67
BSS-44	264.0733222	-44.7321552	21.14	20.13	19.29	18.73
BSS-45	264.0705941	-44.7356392	21.42	20.14	19.56	18.93
BSS-46	264.0826815	-44.7205322	21.03	20.16	19.48	18.92
BSS-47	264.0741392	-44.7369091	21.72	20.22	20.00	-
BSS-48	264.0796168	-44.7316743	21.49	20.22	19.66	18.82
BSS-49	264.0725420	-44.7373506	21.42	20.23	19.41	18.67
BSS-50	264.0727137	-44.7347390	20.91	20.23	19.21	18.83
BSS-51	264.0728013	-44.7352342	20.71	20.24	19.49	18.94
BSS-52	264.0708155	-44.7354777	21.80	20.24	19.60	18.96
BSS-53	264.0666210	-44.7356899	21.13	20.25	19.46	18.91
BSS-54	264.0704891	-44.7268370	21.38	20.26	19.60	18.92
BSS-55	264.0980270	-44.7386344	21.18	20.26	19.35	18.72
BSS-56	264.0741211	-44.7239227	21.26	20.26	19.49	19.03
BSS-57	264.0731733	-44.7359040	21.17	20.28	19.48	18.75
BSS-58	264.0954016	-44.7362336	21.72	20.30	19.84	19.08
BSS-59	264.0743720	-44.7343175	21.57	20.30	19.44	18.62
BSS-60	264.0793244	-44.7373760	21.50	20.30	19.72	19.04
BSS-61	264.0690277	-44.7373768	21.71	20.30	19.72	19.09
BSS-62	264.0912426	-44.7405868	21.15	20.31	-	-
BSS-63	264.0722140	-44.7372844	21.36	20.33	19.49	18.98
BSS-64	264.0728109	-44.7215652	21.43	20.33	19.32	18.89
BSS-65	264.0719910	-44.7354745	21.80	20.34	19.90	19.44
BSS-66	264.0860927	-44.7398976	21.19	20.34	19.51	18.87
BSS-67	264.0730524	-44.7343388	20.84	20.35	19.46	19.08
BSS-68	264.0986242	-44.7176347	21.67	20.37	19.64	18.96
BSS-69	264.0800129	-44.7312105	21.41	20.38	19.83	19.14
BSS-70	264.1113200	-44.7289661	21.65	20.38	19.56	18.88
BSS-71	264.0702622	-44.7378023	21.50	20.38	19.63	19.08
BSS-72	264.0717220	-44.7350064	20.93	20.38	19.51	18.91
BSS-73	264.0728847	-44.7360009	21.31	20.39	19.70	19.12
BSS-74	264.0692923	-44.7360376	21.44	20.40	19.77	19.28
BSS-75	264.0955880	-44.7417241	21.15	20.40	19.52	19.10
BSS-76	264.0693855	-44.7394905	21.28	20.40	19.79	19.28
BSS-77	264.1038007	-44.7310446	21.15	20.42	19.61	18.99
BSS-78	264.0798640	-44.7278464	21.72	20.43	19.87	19.20
BSS-79	264.0659657	-44.7483103	21.53	20.43	19.80	19.08
BSS-80	264.0703238	-44.7369962	21.64	20.45	19.68	19.08
BSS-81	264.0699210	-44.7360097	21.52	20.47	19.81	19.25
BSS-82	264.0816205	-44.7257532	21.61	20.47	19.89	19.19
BSS-83	264.0738714	-44.7341383	21.60	20.48	19.88	19.20
BSS-84	264.0703247	-44.7372218	21.54	20.48	19.69	19.00
BSS-85	264.0846404	-44.7532567	21.07	20.48	19.71	19.26
BSS-86	264.0752340	-44.7368040	21.13	20.50	19.75	18.98

(continued on next page)

Table 6.2 – continued from previous page

Name	RA[degree]	Dec[degree]	m_{255}	U	B	V
BSS-87	264.0732053	-44.7336856	21.73	20.51	19.67	18.78
BSS-88	264.0716876	-44.7420581	21.28	20.54	-	-
BSS-89	264.0769857	-44.7358893	21.75	20.56	19.85	19.27
BSS-90	264.0745164	-44.7347478	21.43	20.57	19.30	18.68
BSS-91	264.0771518	-44.7162974	21.64	20.58	19.73	19.16
BSS-92	264.0731693	-44.7307359	21.41	20.58	19.70	19.24
BSS-93	264.0665272	-44.7338214	21.76	20.58	20.74	-
BSS-94	264.0728917	-44.7367876	21.75	20.58	19.86	19.20
BSS-95	264.0728622	-44.7332917	21.73	20.60	19.92	19.20
BSS-96	264.0699788	-44.7348746	21.68	20.62	20.06	19.42
BSS-97	264.0767788	-44.7367850	21.76	20.65	19.99	19.30
BSS-98	264.0752313	-44.7360231	21.43	20.66	19.91	19.40
BSS-99	264.0690455	-44.7360655	21.59	20.66	19.92	19.33
BSS-100	264.0645021	-44.7366823	21.63	20.67	20.33	-
BSS-101	264.0868248	-44.7226142	21.22	20.70	19.94	19.35
BSS-102	264.0763519	-44.7343980	21.79	20.71	19.98	19.41
BSS-103	264.0738812	-44.7323527	21.78	20.78	20.49	-
BSS-104	264.0817348	-44.7255523	21.80	20.81	20.76	-
BSS-105	264.0879744	-44.7530901	21.64	20.82	20.06	19.45
BSS-106	264.0958204	-44.7476216	21.54	20.82	19.97	19.33
BSS-107	264.0744738	-44.7352289	21.62	20.84	20.19	19.63
BSS-108	264.0683065	-44.7366074	21.57	20.85	20.27	19.71
BSS-109	264.0729048	-44.7357186	21.45	20.91	20.10	19.56
BSS-110	264.1051211	-44.7400310	21.68	20.93	20.00	19.41
BSS-111	264.0750004	-44.7380082	21.70	20.97	20.25	19.64
BSS-112	264.1034917	-44.7330571	21.80	20.99	20.90	-
BSS-113	264.0664414	-44.7191412	21.65	21.04	20.73	-
BSS-114	264.1041424	-44.7372147	21.79	21.15	20.89	-
BSS-115	264.0587770	-44.7232668	-	-	18.42	17.73
BSS-116	264.0587877	-44.7419468	-	-	18.41	17.99
BSS-117	264.0415475	-44.7494423	-	-	19.03	18.32
BSS-118	264.0591752	-44.7325291	-	-	19.44	18.73
BSS-119	264.0399619	-44.7416955	-	-	19.44	18.76
BSS-120	264.0626549	-44.7319403	-	-	19.26	18.67
BSS-121	264.0656735	-44.7382969	-	-	19.70	19.00
BSS-122	264.0543045	-44.7165044	-	-	18.92	18.47
BSS-123	264.1024248	-44.7197756	-	-	19.24	18.63
BSS-124	264.0985183	-44.7176377	-	-	19.47	18.83
BSS-125	264.0372996	-44.7495574	-	-	19.38	18.78
BSS-126	264.0726785	-44.7602530	-	-	19.28	18.71
BSS-127	264.0450589	-44.7245777	-	-	19.38	18.88
BSS-128	264.0664781	-44.7116443	-	-	19.75	19.06
BSS-129	264.0868936	-44.7619855	-	-	19.80	19.15
BSS-130	264.0515702	-44.7488506	-	-	19.93	19.24

(continued on next page)

Table 6.2 – continued from previous page

Name	RA[degree]	Dec[degree]	m_{255}	U	B	V
BSS-131	264.0414501	-44.7250296	-	-	19.75	19.10
BSS-132	264.0608376	-44.7354588	-	-	19.71	19.17
BSS-133	264.0432072	-44.7496767	-	-	19.72	19.10
BSS-134	264.0408113	-44.7188845	-	-	19.70	19.15
BSS-135	264.0537356	-44.7414724	-	-	19.94	19.25
BSS-136	264.0419570	-44.7266006	-	-	19.66	19.19
BSS-137	264.0460967	-44.7523250	-	-	19.53	19.07
BSS-138	264.0464003	-44.7497293	-	-	20.08	19.43
BSS-139	264.0670837	-44.7300225	-	-	19.62	19.12
BSS-140	264.0929004	-44.7590185	-	-	19.85	19.39
BSS-141	264.0520071	-44.7447235	-	-	19.53	19.06
BSS-142	264.0642760	-44.7398872	-	-	20.19	19.55
BSS-143	264.1023870	-44.7487205	-	-	19.92	19.42
BSS-144	264.0614927	-44.7448240	-	-	19.99	19.36
BSS-145	264.0614923	-44.7351662	-	-	19.97	19.36
BSS-146	264.0895926	-44.7593768	-	-	20.14	19.51
BSS-147	264.0503348	-44.7281774	-	-	19.96	19.47
BSS-148	264.1046050	-44.7521475	-	-	20.06	19.45
BSS-149	264.0652589	-44.7258199	-	-	20.18	19.58
BSS-150	264.0442421	-44.7459965	-	-	20.32	19.75
BSS-151	264.0407394	-44.7479096	-	-	20.26	19.70
BSS-152	264.0517913	-44.7413855	-	-	20.44	19.91
BSS-153	264.0691168	-44.7411559	-	-	19.64	19.14

r_i	r_e	$N_{\rm BSS}$		$N_{\rm RHB}$		$N_{\rm BHB}$		$N_{\rm EHB}$		$N_{\rm BHk}$		$L^{\rm samp}/L^{\rm samp}_{\rm tot}$
[arcsec]	[arcsec]	obs	bck	obs	bck	obs	bck	obs	bck	obs	bck	
0	5	22	0	91	0	18	0	1	0	6	0	0.08
5	15	43	0	346	0	57	0	7	0	8	0	0.26
15	25	17	0	221	0	43	0	3	0	5	0	0.18
25	40	10	1	247	1	54	0	3	0	4	0	0.17
40	65	24	2	248	2	52	1	8	0	8	0	0.16
65	110	37	7	237	6	40	1	4	0	6	0	0.15

Table 6.3: The values listed out of the parenthesis correspond to the number of stars assumed to belong to the cluster (and thus used in the analysis), while those in the parenthesis are estimated to be contaminating field stars (see Sect. 6.2.4).

Chapter 7

The surface density profile of NGC 6388: a good candidate for harboring an intermediate-mass black hole

Based on the results published in:

Lanzoni, B.; Dalessandro, E.; Ferraro, F. R.; Miocchi, P.; Valenti, E.; Rood, R. T.;

ApJL, 668, L139

Abstract

We have used a combination of high resolution (HST ACS-HRC, ACS-WFC, and WFPC2) and wide-field (ESO-WFI) observations of the galactic globular cluster NGC 6388 to derive its center of gravity, projected density profile, and central surface brightness profile. While the overall projected profiles are well fit by a King model with intermediate concentration ($c = 1.8$) and sizable core radius ($r_c = 7\farcs2$), a significant power law (with slope $\alpha = -0.2$) deviation from a flat core behaviour has been detected within the inner $1''$. These properties suggest the presence of a central intermediate mass black hole. The observed profiles are well reproduced by a multi-mass isotropic, spherical model including a black hole with a mass of $\sim 5.7 \times 10^3\ M_\odot$.

7.1 Introduction

The surface brightness (SB) and the projected density profiles of the vast majority of globular clusters (GCs) are well reproduced by a family of simple models characterized by an extended isothermal core and a tidally truncated envelope—the so-called King models (King 1966).

However a fraction ($\sim$ 15–20%, see Djorgovski & King 1986) of galactic GCs deviate significantly from this behaviour. The projected density profiles of these clusters do not exhibit an extended core, showing instead a power law behaviour $\Sigma(r) \propto r^{\alpha}$ with α ranging from -0.8 to -1.0 . This feature has been thought to arise from the dynamical evolution of stellar systems that have experienced the collapse of the core. These are called post-core collapse clusters, hereafter PCC).

However, other processes can affect the shape of a star cluster density profile; among these the existence of an Intermediate Mass Black Hole (IMBH) in the central region has recently received attention. Interestingly enough, detailed collisional N-body simulations (Baumgardt et al., 2005, hereafter BMH05; Trenti et al. 2007) and theoretical arguments (Heggie et al. 2007) have shown that the presence of a IMBH yields quite a different SB profile than core collapse does. These studies indicate that in an initially dense cluster a IMBH gives rise to a strong expansion of the central region that, in turn, leads to a quasi-steady configuration resembling that of a medium concentration cluster with a core-like profile. Thus, the clusters most likely to harbor IMBHs are those having the appearance of normal King model clusters except in the very central regions where a power law deviation from a flat behaviour is expected. The exponent of this power law is predicted to be significantly lower ($\alpha \sim -0.2$) than in the PCC case (BMH05, Miocchi 2007). Small departures from a King model have been observed in the projected density profile of a few GCs (included NGC 6388) by Noyola & Gebhardt (2006, hereafter NG06).

The confirmation of the existence of IMBHs and an estimate of their frequency would be important for a number of astrophysical problems like the formation processes of super massive BH in galaxies, super-Eddington X-ray sources in extragalactic globular clusters (Sivakoff et al. 2007), the origin of ultraluminous X-ray sources (Miller 2003; Fabbiano 2006). Despite of their potential importance, the existence of IMBH in GCs is still an open question. For instance, the evidence for an IMBH in M15 reported by van der Marel et al. (2002) and Gebhardt, Rich & Ho (2002) has been questioned by Baumgardt et al (2003a). Baumgardt et al (2003b) also question evidence for an IMBH in G1 in M31 (Gebhardt, Rich & Ho 2002, but see Gebhardt, Rich & Ho 2005 and the recent findings by Ulvestad et al 2007 and Green & Ho 2007).

Here we present accurate surface density and SB profiles obtained with a combination of high-resolution and wide-field observations of the galactic globular cluster NGC 6388, which a number of authors (BMH05; NG06; Drukier & Bailyn 2003, hereafter DB03; Miocchi 2007) have indicated as a prime candidate to harbor an IMBH. These profiles nicely match the theoretical

models of a cluster with a $5.7 \times 10^3 M_\odot$ BH: having an extended core, intermediate concentration, but also significant deviations from a flat core distribution in the innermost cluster regions ($r \lesssim 1''$).

7.2 The data

In this paper we make use of a combination of high-resolution and wide-field photometric data sets, obtained with WFPC2 and ACS on board *HST*, and with WFI at ESO-2.2 m, respectively. A detailed description of the observations, photometric reduction and astrometry procedures of the data obtained with WFPC2, ACS-WFC, and WFI is given in a companion paper discussing the Blue Straggler Star and Horizontal Branch populations (Dalessandro et al 2008a; see also the previous Chpater). Here we use only the optical (B, V, I) samples from the entire multi-wavelength data set. These have been all homogenized and transformed to the Johnson magnitude system. All the star positions have been placed on the absolute astrometric system using several hundred astrometric reference stars from the new astrometric 2-MASS catalogue[1], following the procedure described, e.g., in (Lanzoni et al. 2007a), with a final astrometric accuracy of the order of $\sim 0\farcs3$ both in RA and Dec.

Additional images obtained with the ACS-HRC have been retrieved from the ESO/ST-ECF Science Archive. These data sample the cluster central region with a field of view (FoV) of $26'' \times 29''$ and a spatial resolution of $0\farcs027\,\mathrm{pix}^{-1}$. The HRC data were obtained through filters $F555W$ (V) and $F814W$ (I), with total exposure times of 620 and 3070 s, respectively. After corrections for geometric distortions and effective flux (Sirianni et al. 2005), the photometric analysis was performed by using SExtractor (Bertin & Arnouts 1996), adopting a fixed aperture radius of 4 pixels ($0\farcs108$). The sample has then been astrometrized and photometrically calibrated by using the stars in common with the ACS-WFC catalog. The color-magnitude diagrams based on the data from all four data sets are shown in Fig. 7.1.

7.3 Center of gravity

Given the absolute positions of individual stars in each catalog, the center of gravity, $C_{\rm grav}$, of NGC 6388 has been determined by averaging the coordinates α and δ of all stars detected in the highest resolution data set (the HRC sample). In order to correct for spurious effects due to incompleteness in the very inner regions of the cluster, we considered only stars brighter than

[1] Available at `http://irsa.ipac.caltech.edu`.

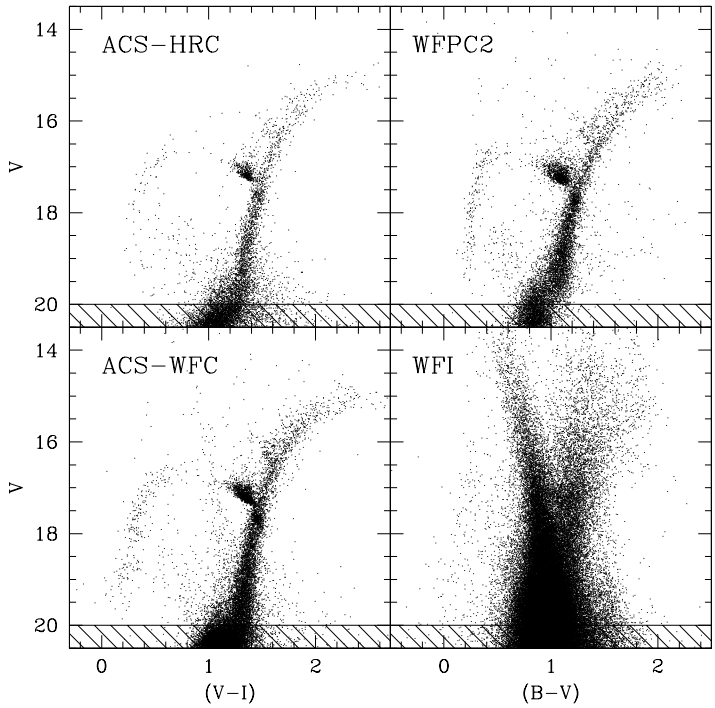

Figure 7.1: Color Magnitude diagrams for the four data sets used. The WFI data are dominated by field contamination.

$V = 20$ (roughly corresponding to the sub-giant branch of the cluster). By following the iterative procedure described in Montegriffo et al. 1995 (see also Ferraro et al. 2004), the center of gravity is located at $\alpha_{\rm J2000} = 17^{\rm h}\,36^{\rm m}\,17\overset{\rm s}{.}23$, $\delta_{J2000} = -44^\circ\,44'\,7\overset{''}{.}1$, with an uncertainty of $0\overset{''}{.}3$ in both α and δ. A careful examination of field inside the core radius shows that our determination of the center is biased neither by the presence of very bright stars, nor of a star clump. The derived $C_{\rm grav}$ is located $\sim 2\overset{''}{.}6$ southeast ($\Delta\alpha = 3\overset{''}{.}4$, $\Delta\delta = -1\overset{''}{.}1$) of that derived by Djorgovski & Meylan (1993) using the surface brightness distribution. An accurate comparison with the center adopted by NG06 is not possible since the value listed in their Table 1 is just referred to the world coordinate system of a specific WFPC2 image, however a visual inspection suggests that their center is located $\sim 0\overset{''}{.}5$ SE of ours.

7.4 Projected density and surface brightness profiles

We have determined the projected density profile of NGC 6388 using direct star counts over the entire cluster radial extent, from $C_{\rm grav}$ out to $\sim 1400'' \sim 23'$. This distance is significantly

larger than the expected cluster extension ($r_t = 372''$, Harris 1996). In order to avoid spurious effects due to possible incompleteness, only stars brighter than $V = 20$ have been considered (see Dalessandro et al 2008a). There are more than 58,000 stars in the entire (i.e., the combination of ACS, WFPC2 and WFI) photometric data set. Following the procedure described in Ferraro et al. 1999a, we have divided the sample in 40 concentric annuli, each centered on $C_{\rm grav}$. Each annulus has been split into an adequate number of sub-sectors. The number of stars lying within each sub-sector was counted, and the star density was obtained by dividing these values by the corresponding sub-sector areas. The stellar density in each annulus was then obtained as the average of the sub-sector densities, and the uncertainty in the average values for each annulus was estimated from the variance among the sub-sectors. The radius associated with each annulus is the mid-point of the radial bin. The outermost ($r \gtrsim 7'$) measures have an almost constant value and their average has been used to estimate the Galaxy contamination to be ~ 56 stars arcmin^{-2}. Subtracting this background yields the the profiles shown in Figs. 7.2.

If the innermost ($r < 1''$) points are excluded, the density profile is well fit all over the entire extension by an isotropic, single-mass King model with a core of $r_c = 7''.2$ and an intermediate concentration ($c = 1.8$). These values are similar to those quoted by Trager et al. (1995; $r_c = 7''.4$ and $c = 1.7$), Harris (1996; $r_c = 7''.2$ and $c = 1.7$), and McLaughling & van der Marel (2005; $r_c = 7''.8$ and $c = 1.71$).[2] In the inner $\sim 1''$ the observed profile shows an indication of a deviation from a flat core behaviour. With only 7 stars in the innermost bin, the statistical error of the inner bin ($0'' \leq r < 0''.3$) is relatively large. With star counts alone the exact amount of the deviation from the flat core cannot be reliably estimated.

Exploiting the exceptional high resolution of ACS-HRC images we have computed the SB profile by direct aperture photometry to more accurately determine the inner shape of the cluster profile. In the innermost region ($r < 1''$) we have used two sets of annuli stepped by $0''.3$ and $0''.5$, respectively. The SB values have been computed as the sum of the counts in each pixel, divided by the number of pixels in any given annulus. The counts have then been converted to a magnitude scale and calibrated by using a relation that links the "instrumental" magnitude to the calibrated one (obtained by performing aperture photometry for a number of high S/N isolated stars). The resulting SB profile for the innermost $10''$ from the center is shown in Figure 7.3. A steepening of the profile at $r \lesssim 1''$ is clearly apparent, in agreement with what we found above for the surface density distribution. A linear fit to the inner points suggest that the slope of the profile is 0.6 ± 0.06

[2]Note that the higher concentration quoted in the present paper implies a ($\sim 20\%$) larger tidal radius ($r_t = 454''$) than previously determined.

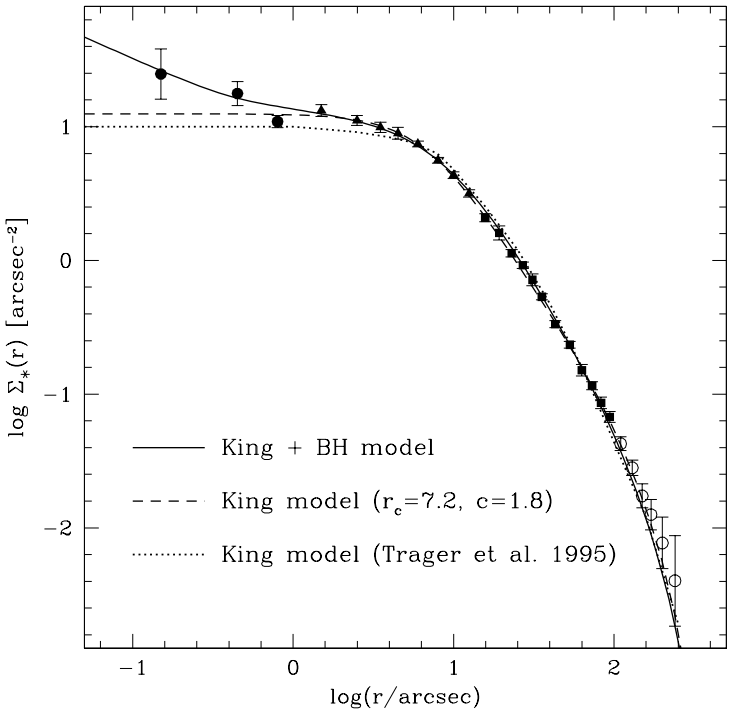

Figure 7.2: Observed surface density profile obtained by star counts from the combined photometric data-set: ACS-HRC (*filled circles*), WFPC2 (*triangles*), ACS-WFC (*squares*), and WFI (*empty circles*). The background level (see Sect. 7.4) has been subtracted. The single-mass King model that best fits the profile excluding the innermost ($r \lesssim 1''$) points is shown as a dashed line. It is characterized by a sizable core radius ($r_c = 7''.2$), and an intermediate concentration ($c = 1.8$). The solid line shows the profile of the model (see Sect. 7.5) including a $5.7 \times 10^3 M_\odot$ BH in the cluster center. The profile from Trager et al (1995) is shown (*dotted line* for comparison.

in the $\log \Sigma - \log r$ plane.

In terms of the surface luminosity density $I(r)$, if $I \propto r^\alpha$ we find $\alpha \simeq -0.23$. This is steeper (but still marginally consistent within the errors) than the slope $\alpha = -0.13 \pm 0.07$ derived from the analysis of WFPC2 images by NG06. The N06 profile is shown for comparison in Figure 7.3, as can be seen their profile is fully compatible with our data in the common region. The use of high resolution images allow us to probe the innermost region of the cluster where most of the deviation from a flat behaviour occurs[3].

[3]Even the small difference in the center determination can play a role. Simulations have shown that even an offset of only a few $0''.1$ is sufficient to flatten the profile. An additional difference in the slope determination might arise from the different approach used by NG06, who removed the bright stars and did not fit a power law to the data but instead calculated the derivative of the smooth central profile.

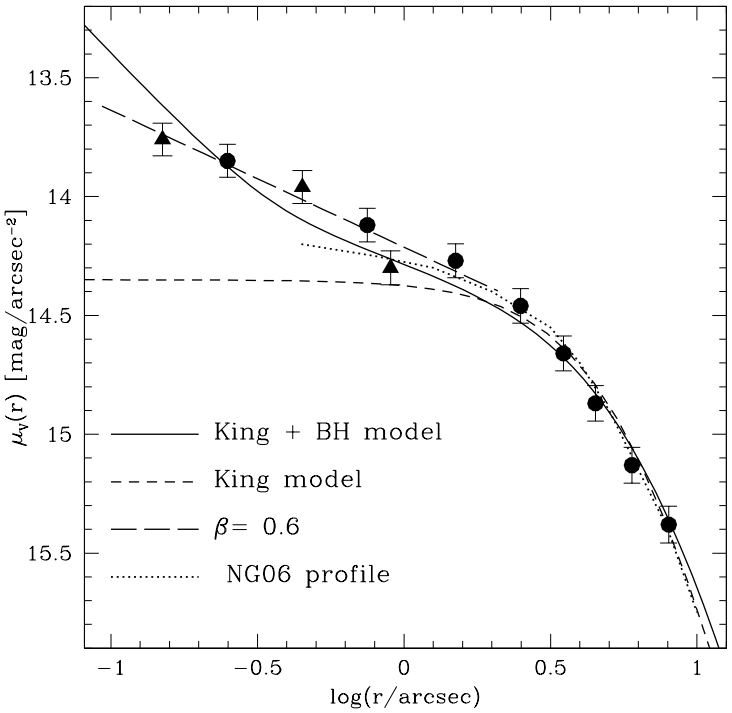

Figure 7.3: Surface brightness profile derived from the ACS-HRC images within $10''$ from the cluster center. *Dots* refer to a radial binning of $0''.5$, triangles sample the inner $1''$ by steps of $0''.3$. The *solid line* shows the profile of the model obtained by including a $5.7 \times 10^3 M_\odot$ BH (the same as in Fig. 7.2). The *short-dashed line* corresponds to the King model shown in Fig. 7.2. $\beta = 0.6$ is the slope of the linear best fit (see the *long-dashed line*) to the innermost points. The profile obtained by NG06 is also shown (see the *dotted line* for comparison.

7.5 Discussion

The properties of the projected density and SB profiles derived in the previous section for NGC 6388 are not those of a cluster which has experienced the core collapse. Instead they are just what BMH05 suggest as the signatures of a cluster harboring an IMBH in its center: *(i)* a typical King profile with intermediate concentration ($c = 1.8$) in the external regions, *(ii)* a sizable core, and *(iii)* a inner logarithmic slope $\alpha \sim -0.2$. These features have been recently confirmed by the predictions of a self-consistent parametric model that includes the presence of a central IMBH (Miocchi 2007). This model consists of a multi-mass isotropic, spherical King model, which has been extended inside the region of gravitational influence of the BH via the inclusion of the Bahcall & Wolf 1976 phase-space distribution function.

In order to further support the case for an IMBH in the center of NGC 6388, we have

used this model to reproduce the observed density and SB profiles. A Salpeter mass function ($\mathrm{d}N \propto m^{-1.35}\mathrm{d}\log m$) is assumed in the model and seven discrete mass bins are used to approximate the continuum mass spectrum of the real cluster. The stellar mass range in the interval from 0.3 to 0.9 $M_\odot$ (here and thereafter, where not specified, masses are measured in $M_\odot$) equally subdivided in 6 bins 0.1 wide. These were populated with main sequence stars. In addition the bins $[0.5, 0.6]$ and $[0.7, 0.8]$ include WD populations with mass 0.55 and 0.75, coming from progenitors with mass, respectively, in $[0.9, 1.5]$ and $[1.5, 4]$ ranges. The seventh mass bin contains a massive WD population with $m = 1.2$, hypothesized as remnants of stars with mass 4–8. The $[0.8, 0.9]$ bin has $< m >= 0.84$ and contains the TO stars, plus giants and HB stars. The light-to-mass ratios were taken to be $\{4.9 \times 10^{-3}, 10^{-2}, 2.3 \times 10^{-2}, 6.5 \times 10^{-2}, 0.19, 10, 0\}$ corresponding to the bins ordered in increasing average mass. The velocity dispersion of the seven components is constrained by the requirement of complete energy equipartition at the border of the BH influence region (see Miocchi et al. 2006; Miocchi 2007), where the adimensionalised potential $W_{\rm BH}$, along with the the ratio between the BH mass ($M_{\rm BH}$) and the cluster mass (M), determine the form of the generated profiles. Besides of the various scale parameters, $W_{\rm BH}$ and $M_{\rm BH}$ are adjusted to obtain the best fit to the observed profiles. To do this, we conservatively include only data from the central $100''$ in order to avoid possible spurious effects which might affect the most external points of the SB profiles because of the field contamination subtraction. The best fit to the observed SB profile is then found for $r_c = 7\farcs2$, $c = 1.8$, $W_{\rm BH} = 11.5$ and $M_{\rm BH} = 2.2 \times 10^{-3} M$ (yielding $P(\chi^2 > \chi^2_{\rm fit}) > 99\%$). The level of confidence remains above 97% for an IMBH mass in the range 2.1–$2.4 \times 10^{-3} M$. The r_c and c values are consistent with the value deduced by the parametric fit of the single-mass King model mentioned above. The results of this parametric fit to the projected density and the SB profiles are shown in Figs. 7.2 and 7.3 respectively.

By assuming the total cluster luminosity $V_t = 6.72$ (Harris 1996), and the distance modulus $(m - M)_V = 16.59$ (Dalessandro et al. 2008a)[4], we estimate a total mass of $2.6 \times 10^6 M_\odot$ for NGC 6388, yielding $M_{\rm BH} \simeq 5.7 \times 10^3 M_\odot$.[5]

While the central IMBH is a possible explanation of the shape of the observed profiles, one might question whether this result is unique. In fact, a central concentration of massive remnants

[4]The distance has been obtained differentially with respect to 47 Tucanae, by assuming the distance scale by Ferraro et al. (1999b).

[5]Note that this mass is well within the range of values (2.5–10×10^3) derived from the $M_{\rm BH} - \sigma$ relation (Ferrarese & Merritt 2000; Gebhardt et al. 2000; see for example equation (10) of DB03), by assuming the low ($\beta = 4.02$) and the high ($\beta = 4.65$) exponents, respectively.

(like white dwarfs and neutron stars) has been proposed as an alternative explanation in the case of M15 (van den Bosch et al. 2006). However, we have found that a multi-mass King model including a population of such remnants but without central BH is unable to reproduce the observed slope of the profiles in the core region. Since our evidence is based exclusively from the shape of the density profile, the presence of a IMBH at the center of NGC 6388 is still debatable. Accurate kinematical studies of the motion of stars in the central region of the cluster are needed to solidify the case.

The region in which to seek for the possible kinematical signatures of a BH is very small. The self-consistent model here employed generates a projected velocity dispersion profile that shows a sharp rise from the "isothermal plateau" to a purely Keplerian behaviour at $r \sim 0\farcs16$ (i.e., $\sim 0.02\, r_c$). A more promising path to detect the kinematic signature of a BH is by proper motion measurements (DB03). Some stars should move with anomalously high velocities under the influence of the BH. In order to estimate the number of these stars, we first need to evaluate the BH radius of influence r_h. A crude estimate of r_h is given by: $r_h = G\, M_{\rm BH}/\sigma_0^2$, where σ_0 is the velocity dispersion outside r_h. By assuming $\sigma_0 = 18.9\,{\rm km\,s^{-1}}$ (Pryor & Meylan 1993), we find $r_h \simeq 0.07\,$pc, corresponding to $1\farcs1$ with the cluster distance ($d = 13.18\,$kpc; Dalessandro et al. 2008a). By using equation (7) of DB03, it is possible to estimate the number of stars (N), measurable through proper motions studies, having velocities 3 times the cluster velocity dispersion outside r_h: $N = 0.27\,\Sigma_0\, r_h^2$, where $\Sigma_0\, r_h^2$ is the number of stars within r_h. This relation suggests that $\sim 27\%$ of stars within r_h are expected to show anomalously high velocity. We can directly derive this number from the HRC images. Adopting the value of the cluster center presented above we count 28 relatively bright ($V < 19$) stars within $r_h = 1\farcs1$ (out of a total of ~ 85 stars detected down to $V \sim 22$), corresponding to a total of ~ 7 high-velocity stars. This estimate shows that the presence of $\sim 5 \times 10^3 M_\odot$ BH in the center of NGC 6388 can in principle be kinematically confirmed in the near future through accurate proper motion studies or radial velocity measurements with *Adaptive Optic* supported instruments. However, these measurements can be quite challenging. According to Figure 1 of DB03, the high velocity stars are expected to be mainly confined within $0.4\, r_h$ (only $\sim 0\farcs4$ from the center). They would have speeds of order $60\,{\rm km\,s^{-1}}$ which, given projection effects, would give tangential velocities of order $20\,{\rm km\,s^{-1}}$. The distance derived by (Dalessandro et al. 2008a) and adopted here is 25% larger than that from Harris (1996), so the resulting proper motions would be $\sim 0.3\,{\rm mas\,yr^{-1}}$. Given the current estimate for the proper motion measurement error of roughly 0.3 mas, a baseline

of at least 3–5 yr would be required.

Chapter 8

Conclusions and future perspectives

This Thesis is part of a project devoted at exploring the interplay between dynamics and stellar evolution in GGCs, through the detailed study of peculiar stellar populations. In this work we primarily focused on BSS. The number of interesting results that we have obtained clearly demonstrates that the best approach to study the BSS population consists in using:

1. High-resolution UV observations in the dense central regions of the clusters. This allows to minimize the effects of blends by SGB and RGB stars, that dominate the emission at optical wavelengths and to observe BSS in the band where they are the most powerful emitters.

2. Wide field observations, needed to characterize the BSS properties all over the cluster extension.

By using such an approach we have obtained a number of results which are significantly contributing to construct a complete observational database of BSS in GGCs. Table 8.1 summarize the most important results obtained by our group, with the ones obtained within this Thesis highlighted in bold-face.

Figures 8.1, 8.2, 8.3 present the BSS radial distributions obtained up to now in 12 GGCs (6 of them have been studied in this Thesis). As can be seen in most cases the distribution is bimodal, with a high peak in the cluster center, a dip at intermediate radii and a rising branch in the external regions. In another case (NGC 1904) the radial distribution shows a clear central peak followed by a flat distribution extending to the most external cluster regions. In two cases (namely ω Cen and NGC 2419) the radial distribution is completely flat and not even the central peak is detected.

The interpretation of these distributions is intriguing. For example the agreement between r_{avoid} and the position of the minimum of the radial distributions (discussed for each cluster in the previous Sections) is impressive (see Fig. 8.4), with the only discrepant case being that of

Name	Argument	References
M3	First detection of a BSS bimodal radial distribution	Ferraro et al. 1993,1997
M80	BSS population in the core	Ferraro et al. 1999
47 Tuc	BSS radial distribution	Ferraro et al. 2003
NGC 288	BSS population in the core	Bellazzini et al. 2002
47 Tuc	BSS dynamical modeling and introduction of zone of avoidance concept	Mapelli et al. 2004
NGC 6752	BSS radial distribution	Sabbi et al. 2004
ω Cen	The first flat BSS radial distribution	Ferraro et al. 2006a
47 Tuc	BSS chemical signatures	Ferraro et al. 2006b
NGC 6266	BSS population in the core	Beccari et al. 2006a
–	BSS dynamical modeling of four GCs	Mapelli et al. 2006
M5	**BSS obs and theoretical studies**	**Lanzoni et al. 2007a**
NGC 1904	**BSS obs and theoretical studies**	**Lanzoni et al. 2007b**
M55	**BSS radial distribution**	**Lanzoni et al. 2007c**
NGC 6388	**BSS radial distribution**	**Dalessandro et al. 2008a**
NGC 2419	**The second flat BSS radial distribution**	**Dalessandro et al. 2008b**
M2	**BSS radial distribution - insight on their progeny**	**Dalessandro et al. 2009**

Table 8.1: Paper of this series. All the works part of this Thesis are in bold-face.

NGC 6388 discussed in Chapter 6. This evidence suggests that indeed the radial position of the dip is essentially driven by the dynamical friction efficiency within the cluster.

Hence even at this early stage, our investigation suggests that precious information about the parent cluster dynamical evolution are imprinted in the observed BSS radial distribution. Though the data collected so far is still limited to a dozen of clusters, a first scenario can be drawn from the available database.

The two clusters (NGC 2419 and ω Cen) where the BSS radial distribution is fully consistent with that of the reference populations, are considered to be *dynamically unevolved*. Hence, the observed BSS radial distribution represents a very good approximation of the *initial* BSS radial distribution, i.e. the distribution of the BSS (originated by primordial binaries) at early epochs, when mass segregation and dynamical friction processes had not played a major role yet. In the course of the time, mass segregation and dynamical friction start to segregate binaries (and their by-products) into the cluster center, thus generating the central peak of the distribution. Since the action of dynamical friction and mass segregation progressively extends to larger and larger distances from the center, the dip left by the massive objects sunk to the bottom of the potential well becomes more and more visible at increasing radii. In the meanwhile the most remote

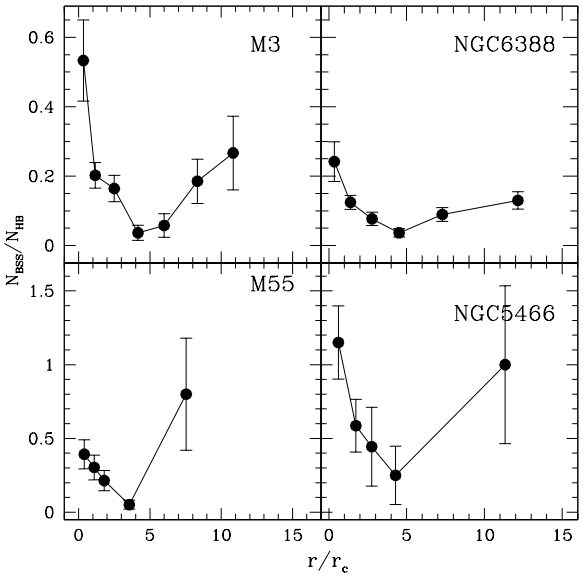

Figure 8.1: Radial distributions of the specific frequency N_{BSS} /N_{HB}, observed in four GGCs (see references in Tab. 8.2.)

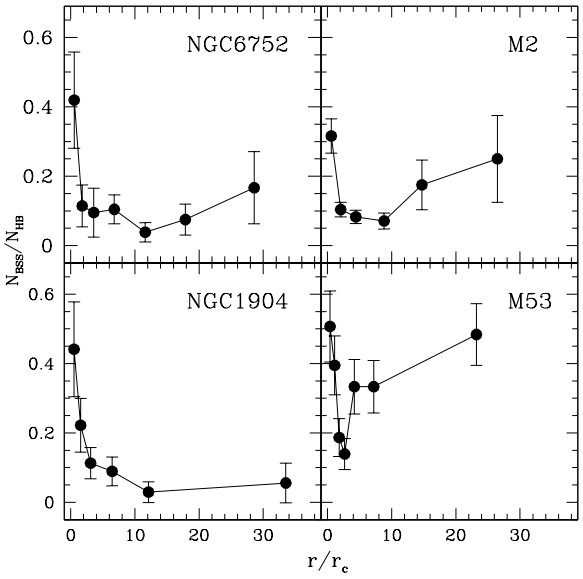

Figure 8.2: As in Fig. 8.1.

BSS are still evolving in isolation in the outer regions of the cluster with nearly the same initial frequency (this generates the rising branch of the observed BSS distribution). Hence because of the dynamical friction effect, the observable r_{min} increases with the dynamical age of the cluster.

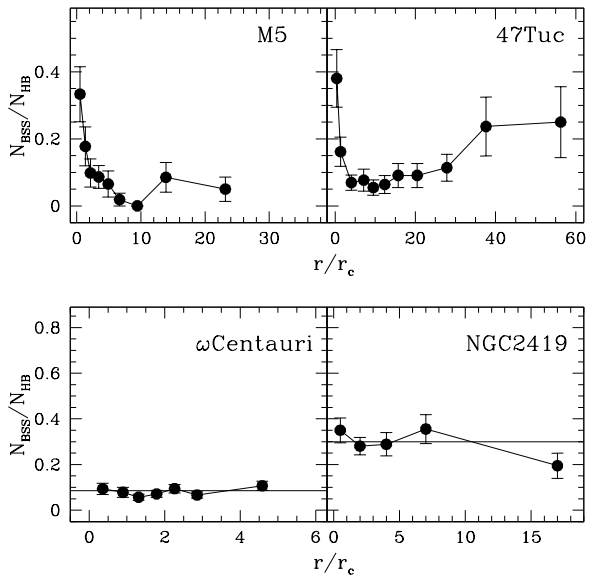

Figure 8.3: As in previous figures. ω Cen and NGC 2419 represents the only clusters that show a flat BSS radial distribution.

In a highly evolved cluster we can expect that virtually all the binaries (at any distance from the cluster center) have sunk into the cluster core, thus generating a single peak in the BSS radial distribution, as observed in NGC 1904.

Thought this scenario needs to be proved by appropriate dynamical simulations, it is in qualitative agreement with the observed general trend, suggesting that a potential "dynamical clock" can be defined from the study of the BSS radial distribution.

8.1 The future: The UV approach to the study of hot stellar populations

As shown in the previous Chapters, the UV approach proposed by our group to the study of BSS in GGSs has produced a number of interesting results, confirming that it is the only viable approach to collect complete samples of hot stars in old stellar populations (whose light is dominated by cool giants). The future development of this project will require two main ingredients:

- enlarging the data-set of GGCs observed following the prescriptions discussed above, in order to properly derive the BSS radial distribution in a adequate number of systems sampling the entire cluster structural parameter space;

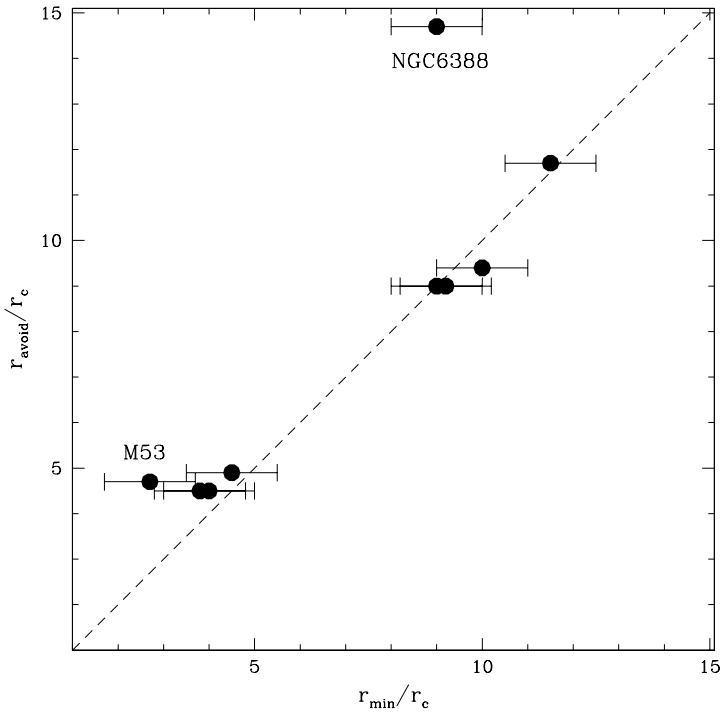

Figure 8.4: Comparison between the observed minimum r_{min} and r_{avoid}. A good agreement is evident for all the clusters with the only outlier represented by NGC 6388.

- performing appropriate N-body simulations in order to accurately study how the radial distribution of a binary population evolves in time in high density environments. This will allow us to quantitatively test and state the ”dynamical cloc” idea discussed above

To this purposes we are leading an HST Large Program (approved in Cycle 16 Supplemental - Prop. 11975; PI Ferraro, granted with 177 orbits) aimed at securing high resolution UV observations of the central regions of 45 GGCs (see Table 8.2). Moreover we are involved in a program which has already secured UV GALEX observations for more than 20 GGCs. By combining these two datasets and complementary ground-based photometry, in a couple of years we will be able to study the BSS radial distribution for almost half of the entire GC population in the Galaxy. In the meanwhile, direct N-body simulations will be performed by using the N-BODY6 code (Aarseth 2006) and by taking advantage of the ongoing collaboration with MODEST[1].

[1]The MOdelling DEnse STellar system project is an international collaboration among various European and US research groups working in stellar dynamics, stellar evolution and stellar hydrodynamics (http://www.manybody.org/modest)

Other hot stellar populations in the UV – Beside BSS, the HST UV Large Program will provide crucial information on other classes of stars populating GGCs. These include the bluest and hottest stars along the HB, their bright progeny (the so-called AGB manqué stars) and post-AGB stars. In particular in the classical (V, B-V) CMD, stars at the blue-end of the HB lie along an almost vertical sequence (the so-called *"blue tail, BT"*), extending down to visual magnitudes similar to or fainter than the main sequence TO. The hottest stars along the BTs are the so-called *extreme HB (EHB) stars*, also observed as hot subdwarf (sdO/sdB) in the Galactic field. These stars are thought to be hot because they have lost almost all their hydrogen-rich envelope during the preceding RGB phase, but many open questions remain (e.g., Catelan et al. 2006): Why do some GGCs have EHB stars and others do not? Are EHB stars related to He-rich sub-populations? (as suggested by Caloi & Dantona 2007), or is it simply a matter that some stars loose much more mass than others during the RGB stage? After the core helium exhaustion, these stars do not return to the asymptotic giant branch (AGB), but rather spend their He-shell burning phase as hot AGB-manqué or Post-early AGB stars, with lifetimes that are strongly influenced by the still poorly understood behaviour of the convective core boundary near He exhaustion (Dorman & Rood 1993). In a few clusters there is an additional population that appears as a fainter extension of the BT and is separated from the EHB stars by a gap: these are the so-called *Blue Hook (BHk)* stars. Not all BT clusters have EHB stars (e.g., NGC1904 - Lanzoni et al. 2007b) and not all clusters with EHB stars have BHk stars (cf. M80 and NGC6388 shown in Fig. 8.5). BHk stars are still poorly understood (e.g., Moehler et al. 2004). Occasionally HBs also exhibit fine structures like the gaps shown in Fig. 8.5, that become particularly evident and are best studied when far-UV filters are used. Multi-populations separated by gaps along the HB might be due to the existence of two mass loss drivers (Ferraro et al. 1998), or to phenomena like the helium dredge-up (Sweigart et al. 2002), or helium abundance variations (D'Antona et al. 2002). Questions like *"Are the gaps always located at the same effective temperature (T_{eff}) in all clusters?"*, or *"Do the gaps correspond to HB regions completely devoid of or only poorly populated by stars?"*, or *"Are the HB multi-populations originated by different mass-loss processes?"* still persist. Many of the features mentioned above are most visible in UV CMDs. More fundamentally the true nature of these hot stars can be revealed only if their physical parameters (at least T_{eff} and the luminosity L) are accurately known. While the value of T_{eff} for HB stars can be reasonably well determined from their position along the HB, this is not the case for the BHk, that requires far UV observations for a proper detection and an accurate study (e.g., in NGC2808 by Moehler et al. 2004 and ω Cen

by Whitney et al. 1998; D'Cruz et al. 2000). As early as 1989, Rood & Crocker argued that the only way to distinguish between various processes affecting the HB morphology (including multiple abundance populations) is to perform high-accuracy studies of the HB star distribution along the "vertical" (log L) direction. This indeed requires UV photometry.

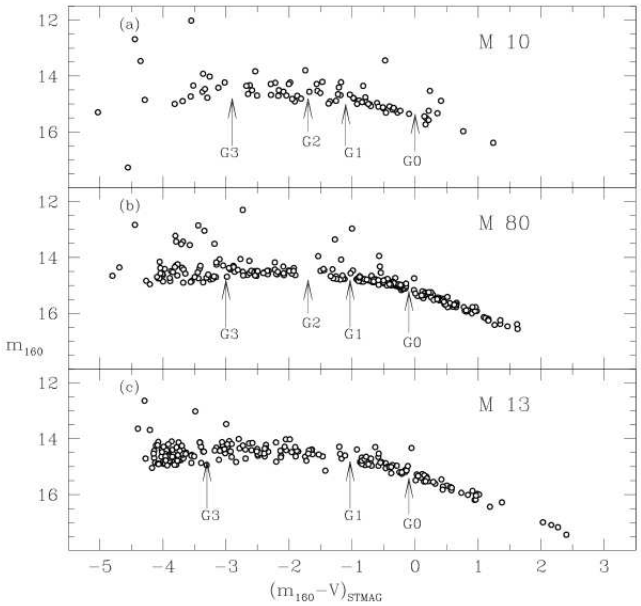

Figure 8.5: HBs in the (m_{160}, m_{160} - V)plane for M10, M80 and M13. The M10 and M80 HBs have been shifted to match M13. M10 shows gaps similar to those found earlier in M13 and M80. The gaps are certainly telling us something important - we are just not quite sure what. Our working hypothesis is that they are related to the mass loss process(es). Important issues yet to be determined: How universal are blue-HB gaps? How do gap locations relate to cluster parameters?

Since an extended blue HB can occur also in metal rich ([Fe/H]=-0.4) stellar populations (e.g., Busso et al. 2007), EHB stars and their progeny are the most likely source of the UV-excess observed in elliptical galaxies and spiral bulges (Buzzoni 1989; Greggio & Renzini 1990). We cannot hope to understand the UV-excess unless we understand these stars locally. Since the most luminous of these stars are rare (a few per cluster at best) we need to observe many clusters and the largest possible are in each of them.

The most age-sensitive part of the integrated light of a distant system is the emission from TO stars, which is optimally observable in the near-UV, where the light from the luminous red stars is suppressed. While in principle such a powerful age estimator can be absolutely calibrated, in practice one must first understand the other contributors to the UV emission. Peterson et al. (2003) have shown that blue-HB stars and BSS are required to explain the near-UV spectrum of

the globular cluster G1 in M31. EHB stars may also be important.

Thanks to the ongoing HST UV Large Program, we will be able to study these hot stellar populations in the largest GGC sample ever surveyed and with unprecedent accuracy, thus finally finding the answers to most of the still open questions discussed above.

Name	RA	Dec	GALEX
NGC1261	03:12:15.3	-55:13:01	◊
NGC2298	06:48:59.2	-36:00:19	◊
NGC3201	10:17:36.7	-46:24:40	–
NGC4147	12:10:06.2	+18:32:32	◊
NGC4372	12:25:45.4	-72:39:33	–
NGC4590-M68	12:39:28.0	-26:44:34	◊
NGC4833	12:59:34.9	-70:52:28	–
NGC5024-M53	13:12:55.2	+18:10:09	◊
NGC5053	13:16:27.0	+17:41:52	–
NGC5466	14 05:27.3	+28:32:18	–
NGC5946	15:35:28.6	-50:39:35	–
NGC5694	14:39:36.5	-26:32:18	–
NGC5824	15:03:58.6	-33:04:07	–
NGC5897	15:17:24.4	-21:00:36	–
NGC6121-M4	16:23:35.4	-26:31:32	–
NGC6144	16:27:14.1	-26:01:29	–
NGC6171-M107	16:32:31.9	-13:03:13	–
NGC6229	16:46:58.8	+47:31:40	◊
NGC6284	17:04:28.7	-24:45:52	◊
NGC6293	17:10:10.4	-26:34:54	–
NGC6342	17:21:10.1	-19:35:15	–
NGC6356	17:23:35.0	-17:48:47	◊
NGC6362	17:31:54.8	-67:02:52	–
NGC6397	17:40:41.3	-53:40:25	–
NGC6402-M14	17:37:36.1	-03:14:45	–
NGC6541	18:08:02.3	-43:42:57	–
NGC6584	18:18:37.6	-52:12:55	–
NGC6626-M28	18:24:32.9	-24:52:11	–
NGC6656-M22	18:36:24.2	-23:54:12	–
NGC6681-M70	18:43:12.6	-32:17:31	–
NGC6717	18:55:06.0	-22:42:06	–
NGC6723	18:59:33.1	-36:37:53	–
NGC6779-M56	19:16:35.5	+30:11:04	–
NGC6838-M71	19:53:46.1	+18:46:42	–
NGC6864-M75	20:06:04.8	-21:55:20	–
NGC6934	20:34:11.5	+07:24:15	–
NGC6981-M72	20:53:27.9	-12:32:13	–
NGC7078-M15	21:29:58.4	+12:10:01	–
IC4499	15:00:19.2	-82:12:49	–
NGC5139-ω Cen	13 26 45.9	-47:28:37	–
NGC6624	18 23 40.5	-30:21:40	–
NGC5286	13 46 26.5	-51:22:24	–
NGC5927	15 28 0.5	-50:40:22	–
NGC1851	05 14 6.3	-40:02:50	–
NGC104	00 24 5.2	-72:04:51	◊

Table 8.2: Target of the HST Prop. GO 16-Supl. The availability of GALEX data is indicated as a ◊

Bibliography

Aarseth, S. J. 2006, Modelling Dense Stellar Systems, 26th meeting of the IAU, Joint Discussion 14, 22-23 August 2006, Prague, Czech Republic, JD14, #1, 14,

Albrow, M. D., et al. 2001, ApJ, 559, 1060

Bahcall J.N., Wolf R.A, 1976, ApJ, 209, 214

Bailyn, C. D. 1994, AJ, 107, 1073

Bailyn, C. D. 1995, ARA&A, 33, 133

Bailyn, C. D., & Pinsonneault, M. H. 1995, ApJ, 439, 705

Baumgardt H., Makino J., Hut P., 2005, ApJ, 620, 238 (BMH05)

Baumgardt, H., Hut, P., Makino, J., McMillan, S., Portegies Zwart, S., 2003a, ApJ, 582, L21

Baumgardt, H., Makino, J., Hut, P., McMillan, S., Portegies Zwart, S., 2003b, ApJ, 589, L25

Beccari, G., Ferraro, F. R., Lanzoni, B., & Bellazzini, M., 2006a, ApJ, 652, L121

Beccari, G., Ferraro, F. R., Possenti, A., Valenti, E., Origlia, L., & Rood, R. T. 2006b, AJ, 131, 2551

Beccari, G., et al. 2008, ApJ, 679, 712

Bedin, L. R., Piotto, G., Anderson, J., Cassisi, S., King, I. R., Momany, Y., & Carraro, G. 2004, ApJl, 605, L125

Bellazzini, M., Ferraro, F. R., & Buonanno, R. 1999, MNRAS 307, 619

Bellazzini, M., Fusi Pecci, F., Messineo, M., Monaco, L., & Rood, R. T. 2002, AJ, 123, 1509

Bellazzini, M. 2007, A&A, 473, 171

Bertin, E., & Arnouts, S. 1996, A&As, 117, 393

Bekki, K., & Freeman, K. C. 2003, MNRAS, 346, L11

Binney, J., & Tremaine, S. 1987, Galactic Dynamics, (Princeton University Press)

Buonanno, R., Buscema, G., Corsi, C. E., Ferraro, I., & Iannicola, G. 1983, A&A, 126, 278

Buonanno, R., Iannicola, G. 1989, PASP, 101, 294

Busso, G., et al. 2007, A&A, 474, 105

Buzzoni, A. 1989, ApJs, 71, 817

Caloi, V., & D'Antona, F. 2007, A&A, 463, 949

Cariulo, P., Degl'Innocenti, S., & Castellani, V. 2004, A&A, 421, 1121

Carretta, E., Gratton, R. G., Bragaglia, A., Bonifacio, P., & Pasquini, L. 2004, A&A, 416, 925

Carretta, E., et al. 2007, A&A, 464, 967

Catelan, M., Stetson, P. B., Pritzl, B. J., Smith, H. A., Kinemuchi, K., Layden, A. C., Sweigart, A. V., & Rich, R. M. 2006, ApJl, 651, L133

Catelan, M. 2007, American Institute of Physics Conference Series, 930, 39

Chernoff, D. F., & Weinberg, M. D. 1990, ApJ, 351, 121

D'Antona, F., Caloi, V., Montalbán, J., Ventura, P., & Gratton, R. 2002, A&A, 395, 69

D'Antona, F., Bellazzini, M., Caloi, V., Pecci, F. F., Galleti, S., & Rood, R. T. 2005, ApJ, 631, 868

D'Cruz, N. L., et al. 2000, ApJ, 530, 352

Dalessandro, E., Lanzoni, B., Ferraro, F. R., Rood, R. T., Milone, A., Piotto, G., & Valenti, E. 2008a, ApJ, 677, 1069

Dalessandro, E., Lanzoni, B., Ferraro, F. R., Vespe, F., Bellazzini, M., & Rood, R. T. 2008b, ApJ, 681, 311

Dalessandro, E., Beccari, E., Lanzoni, B., Ferraro, F. R., Rood, R. T. & Schiavon, P.R. 2009, submitted to ApJ

Davies, M. B., Piotto, G., & de Angeli, F. 2004, MNRAS, 349, 129

Desidera, S. 1998, Master's thesis, Padua Univ.

Djorgovski, S., & Meylan, G. 1993, Structure and Dynamics of Globular Clusters. Proceedings of a Workshop held in Berkeley, California, July 15-17, 1992, to Honor the 65th Birthday of Ivan King. Editors, S.G. Djorgovski and G. Meylan; Publisher, Astronomical Society of the Pacific, Vol. 50, 325

Djorgovski, S. 1993, in ASPC Conf. Ser. 50, Structure and Dynamics of Globular Clusters, ed. S. G. Djorgovski & G. Meylan (San Francisco: ASP), 373D

Dolphin, A. E. 2000, PASP, 112, 1383

Dorman, B., Rood, R. T., & O'Connell, R. W. 1993, ApJ, 419, 596

Dorman, B., & Rood, R. T. 1993, ApJ, 409, 387

Dorman, B., O'Connell, R. W., & Rood, R. T. 1995, ApJ, 442, 105

Drissen, L., & Shara, M. M. 1998, AJ, 115, 725

Drukier, G.,A., Bailyn, C.D., 2003, ApJ, 597, L125 (DB03)

Dubath P., Meylan G., Mayor M., 1997, A&A, 324, 505

Fabbiano, G., 2006, ARA&A, 44, 323

Ferrarese, L., Merritt, D., 2000, ApJ, 539, L9

Federici, L., Bellazzini, M., Galleti, S., Fusi Pecci, F., Buzzoni, A., & Parmeggiani, G. 2007, A&A, 473, 429

Ferraro, F. R., Fusi Pecci, F., Cacciari, C., Corsi, C., Buonanno, R., Fahlman, G. G., & Richer, H. B. 1993, AJ, 106, 2324

Ferraro, F. R., Paltrinieri, B., Fusi Pecci, F., Cacciari, C., Dorman, B., Rood, R. T., Buonanno, R., Corsi, C. E., Burgarella, D., & Laget, M., 1997, A&A, 324, 915

Ferraro, F. R., Paltrinieri, B., Pecci, F. F., Rood, R. T., & Dorman, B. 1998, ApJ, 500, 311

Ferraro, F. R., Paltrinieri, B., Rood, R. T., Dorman, B. 1999a, ApJ 522, 983

Ferraro F. R., Messineo M., Fusi Pecci F., De Palo M. A., Straniero O., Chieffi A., Limongi M. 1999b, AJ, 118, 1738

Ferraro, F. R., D'Amico, N., Possenti, A., Mignani, R. P., & Paltrinieri, B. 2001, ApJ, 561, 337

Ferraro, F. R., Sills, A., Rood, R. T., Paltrinieri, B., & Buonanno, R. 2003, ApJ, 588, 464

Ferraro, F. R., Beccari, G., Rood, R. T., Bellazzini, M., Sills, A., & Sabbi, E. 2004, ApJ, 603, 127

Ferraro, F. R., 2006, in Resolved Stellar Populations, ASP Conference Series, 2005, D. Valls-Gabaud & M. Chaves Eds., astro-ph/0601217

Ferraro, F. R., et al. 2006a, ApJ, 647, L53

Ferraro, F. R., Sollima, A., Rood, R. T., Origlia, L., Pancino, E., & Bellazzini, M. 2006b, ApJ, 638, 433

Fusi Pecci, F., Ferraro, F. R., Corsi, C. E., Cacciari, C., Buonanno, R. 1992, AJ, 104, 1831

Fusi Pecci, F., Ferraro, F. R., Bellazzini, M., Djorgovski, S., Piotto, G., & Buonanno, R. 1993, AJ, 105, 1145

Gebhardt, K., et al., 2000, ApJ, 539, L13

Gebhardt, K., Rich, R.M., Ho, L.C. , 2002, ApJ, 578, L41

Gebhardt, K., Rich, R.M., Ho, L.C. , 2005, ApJ, 634, 1093

Gerssen, J., van der Marel, R.P., Gebhardt, K., Guhathakurta, P., Peterson, R. C.; Pryor, C., 2002, ApJ, 124, 3270

Green, E. M., Liebert, J., & Saffer, R. A. 2001, 12th European Workshop on White Dwarfs, 226, 192

Greene, J.E., Ho, L.C., 2007, ApJ, 656, 84

Greggio, L., & Renzini, A. 1990, ApJ, 364, 35

Harris, W.E. 1996, AJ, 112, 1487

Harris, W. E., et al. 1997, AJ, 114, 1030

Heber, U., Moehler, S., Napiwotzki, R., Thejll, P., & Green, E. M. 2002, A&A, 383, 938

Heggie D. C., Hut P., Mineshige S., Makino J., Baumgardt H., PASJ, 59, L11

Hills, J. G., & Day, C. A. 1976, Astrophys. Lett., 17, 87

Holtzman, J. A., Burrows, C. J., Casertano, S., Hester, J. J., Trauger, J. T., Watson, A. M., & Worthey, G. 1995, PASP, 107, 1065

Hurley, J. R., Aarseth, S. J., & Shara, M. M. 2007, ApJ, 665, 707

King I.R., 1966, AJ, 71, 64

Irwin, M. J., & Trimble, V. 1984, AJ, 89, 83

Ivanova, N., Belczynski, K., Fregeau, J. M., & Rasio, F. A. 2005, MNRAS, 358, 572

Kaluzny J., Olech A., Thompson I. B., Pych W., Krzemiński W., & Schwarzenberg-Czerny A. 2004, A&A, 424, 1101

Lanzoni, B., Dalessandro, E., Ferraro, F. R., Mancini, C., Beccari, G., Rood, R. T., Mapelli, M., & Sigurdsson, S. 2007a, ApJ, 663, 267

Lanzoni, B., et al. 2007b, ApJ, 663, 1040

Lanzoni, B., Dalessandro, E., Perina, S., Ferraro, F. R., Rood, R. T., & Sollima, A. 2007c, ApJ, 670, 1065

Lanzoni, B., Dalessandro, E., Ferraro, F. R., Miocchi, P., Valenti, E., & Rood, R.T. 2007d, ApJ, 668, L139

Layden, A. C., & Sarajedini, A. 2000, AJ, 119, 1760

Lázaro, C., Ferro, A. A., Arévalo, M. J., Bramich, D. M., Giridhar, S., & Poretti, E. 2006, MNRAS, 372, 69

Lee, J.-W., & Carney, B. W. 1999, AJ, 117, 2868

Lee, Y.-W., Joo, J.-M., Sohn, Y.-J., Rey, S.-C., Lee, H.-C., & Walker, A. R. 1999, Nature, 402, 55

Leigh, N., Sills, A., & Knigge, C. 2007, ApJ, 661, 210

Leon, S., Meylan, G., & Combes, F. 2000, A&A, 359, 907

Leonard, P. J. T. 1989, AJ, 98, 217

Lombardi, J. C. Jr., Rasio, F. A., Shapiro, S. L. 1995, ApJ, 445, L117

Mackey, A. D., & van den Bergh, S. 2005, MNRAS, 360, 631

Mandushev, G. I., Fahlman, G. G., Richer, H. B., & Thompson, I. B. 1997, AJ, 114, 1060

Mapelli, M., Sigurdsson, S., Colpi, M., Ferraro, F. R., Possenti, A., Rood, R. T., Sills, A., & Beccari, G. 2004, ApJ, 605, L29

Mapelli, M., Sigurdsson, S., Ferraro, F. R., Colpi, M., Possenti, A., & Lanzoni, B. 2006, MNRAS, 373, 361

Mateo, M., Harris, H. C., Nemec, J., & Olszewski, E. W. 1990, AJ, 100, 469

Mateo M., in "The origins, evolution, and destinies of binary stars in clusters", E. F. Milone & J. C. Mermilliod Eds. 1996, ASPC, 90, 346

McLaughlin, D. E., & van der Marel, R. P. 2005, ApJs, 161, 304

Miller, C. 2003, Dynamics and Evolution of Dense Stellar Systems, 25th meeting of the IAU, Joint Discussion 11, 18 July 2003, Sydney, Australia, 11,

Meylan, G., & Heggie, D. C. 1997, A&Ar, 8, 1

Miocchi P., 2006, MNRAS, 366, 227

Miocchi, P. 2007, MNRAS, 381, 103

Moehler, S., Sweigart, A. V., Landsman, W. B., Hammer, N. J., & Dreizler, S. 2004, A&A, 415, 313

Monaco, L., Bellazzini, M., Ferraro, F. R., & Pancino, E. 2005, MNRAS, 356, 1396

Moni Bidin, C., Moehler, S., Piotto, G., Momany, Y., Recio-Blanco, A., & Mendez, R. A. 2006, in "Globular Clusters: Guides to Galaxies", March 2006, Concepcion (Chile); astro-ph/0606035

Montegriffo, P., Ferraro, F. R., Fusi Pecci, F., & Origlia, L. 1995, MNRAS, 276, 739

Olech, A., Kaluzny, J., Thompson, I. B., Pych, W., Krzeminski, W., & Shwarzenberg-Czerny, A. 1999, AJ, 118, 442

Newberg, H. J., et al. 2003, ApJl, 596, L191

Noyola, E., Gebhardt, K., 2006, AJ, 132, 447 (NG06)

Pancino, E., Ferraro, F. R., Bellazzini, M., Piotto, G., & Zoccali, M. 2000, ApJl, 534, L83

Peterson, R. C., et al. 2003, Bulletin of the American Astronomical Society, 35, 1398

Pietrinferni, A., Cassisi, S., Salaris, M., & Castelli, F. 2006, ApJ, 642, 797

Piotto, G., et al. 1997, Advances in Stellar Evolution, 84

Piotto, G., et al. 2002, A&A, 391, 945

Piotto, G., et al. 2007, ApJl, 661, L53

Pritchet, C. J., & Glaspey, J. W. 1991, ApJ, 373, 105

Pritzl, B. J., Smith, H. A., Catelan, M., & Sweigart, A. V. 2002, AJ, 124, 949

Pryor C., & Meylan G., 1993, Structure and Dynamics of Globular Clusters. Proceedings of a Workshop held in Berkeley, California, July 15-17, 1992, to Honor the 65th Birthday of Ivan King. Editors, S.G. Djorgovski and G. Meylan; Publisher, Astronomical Society of the Pacific, Vol. 50, 357

Recio-Blanco, A., Aparicio, A., Piotto, G., de Angeli, F., & Djorgovski, S. G. 2006, A&A, 452, 875

Renzini, A., & Fusi Pecci, F. 1988, ARA&A, 26, 199

Rey, S.-C., Lee, Y.-W., Ree, C. H., Joo, J.-M., Sohn, Y.-J., & Walker, A. R. 2004, AJ, 127, 958

Rich, R. M., et al. 1997, ApJl, 484, L25

Ripepi, V., et al. 2007, ApJl, 667, L61

Robin, A. C., Reylé, C., Derrière, S., & Picaud, S. 2003, A&A, 409, 523

Rood, R. T., & Crocker, D. A. 1989, IAU Colloq. 111: The Use of pulsating stars in fundamental problems of astronomy, 103

Sabbi, E., Ferraro, F. R., Sills, A., Rood, R. T., 2004, ApJ 617, 1296

Sandquist, E. L., Bolte, M., Stetson, P. B.; Hesser, J. E. 1996, ApJ, 470, 910

Sandquist, E. L., & Martel, A. R. 2007, ApJl, 654, L65

Sarna, M. J., & de Greve, J. P. 1996, QJRAS, 37, 11

Shara, M. M., Saffer, R. A., & Livio, M. 1997, ApJ, 489, L59

Schechter, P. L., Mateo, M., & Saha, A. 1993, PASP, 105, 1342

Sigurdsson S., Phinney, E. S., 1995, ApJS, 99, 609

Sills, A., Karakas, A., & Lattanzio, J. 2008, arXiv:0811.2974

Sirianni, M., et al. 2005, PASP, 117, 1049

Sivakoff, G. R., et al. 2007, ApJ, 660, 1246

Sohn, Y.-J., Byun, Y.-I., & Chun, M.-S. 1996, Ap&SS, 243, 379

Sollima, A., Pancino, E., Ferraro, F. R., Bellazzini, M., Straniero, O., & Pasquini, L. 2005, ApJ, 634, 332

Sollima, A., Beccari., G., Ferraro, F. R., Fusi Pecci, F., & Sarajedini, A., 2007, MNRAS, 380, 781

Sollima, A., Lanzoni, B., Beccari, G., Ferraro, F. R., & Fusi Pecci, F. 2008, A&A, 481, 701

Stetson, P. B. 1987, PASP, 99, 191

Sweigart, A. V., & Catelan, M. 1998, ApJl, 501, L63

Sweigart, A. V., Brown, T. M., Lanz, T., Landsman, W. B., & Hubeny, I. 2002, Omega Centauri, A Unique Window into Astrophysics, 265, 261

Tian, B., Deng, L., Han, Z., & Zhang, X. B. 2006, A&A, 455, 247

Trager, S.C., Djorgovski, S., & King I.R., 1993, Structure and Dynamics of Globular Clusters. Proceedings of a Workshop held in Berkeley, California, July 15-17, 1992, to Honor the 65th Birthday of Ivan King. Editors, S.G. Djorgovski and G. Meylan; Publisher, Astronomical Society of the Pacific, Vol. 50, 347

Trager, S.C.,King I.R. & Djorgovski, S., 1995, AJ, 109, 218

Trenti M., Ardi E., Mineshige S., Hut P., 2007, MNRAS, 374, 857

Ulvestad, J.S., Greene, J.E., Ho, L.C., 2007, ApJ, 661, L151

van den Bergh, S., & Mackey, A. D. 2004, MNRAS, 354, 713

van den Bosch, R., de Zeeuw, T., Gebhardt, K., Noyola, E., van de Ven, Glenn, 2006, ApJ, 641, 852

van der Marel, R.P., Gerssen, J., Guhathakurta, P., Peterson, R.C., Gebhardt, K., 2002, AJ, 124, 3255

Verbunt, F. 2003, in ASP Conf. Ser. 296, New Horizons in Globular Cluster Astronomy, ed. G. Piotto et al. (San Francisco: ASP), 245

Warren, S. R., Sandquist, E. L., & Bolte, M., 2006, ApJ 648, 1026 (W06)

Whitney, J. H., et al. 1998, ApJ, 495, 284

Zaggia, S. R., Piotto, G., & Capaccioli, M., 1997, A&A, 327, 1004

Zhao, J.-L., Chen, L., & Wen, W. 2006, Chinese Journal of Astronomy and Astrophysics, 6, 435

Zinn, R., & Searle, L. 1976, ApJ, 209, 734

Yi, S., Demarque, P., & Oemler, A. J. 1998, ApJ, 492, 480